

UNIVERSITÉ PIERRE ET MARIE CURIE
École Doctorale Chimie Physique et Chimie Analytique de Paris Centre (ED 388)
France



CHARLES UNIVERSITY IN PRAGUE

Faculty of Mathematics and Physics

Czech Republic

Study programme: Physics

Specialisation: Biophysics, chemical and macromolecular physics



Molecular mechanisms of DNA regulatory segment recognition by MADS box family transcription factors

DOCTORAL THESIS OF

Barbora Profantová - Řezáčová

Supervised by Josef Štěpánek and Pierre-Yves Turpin

Presented and publicly defended on September 23, 2014

Members of the jury:

Prof. Vladimír Baumruk	Fac.Math.Phys. Charles University in Prague, Czech Rep.	Examiner
Assoc.prof. Otakar Jelínek	1st Fac.Med., Charles University in Prague, Czech Republic	Referee
Prof. Michel Manfait	Université de Reims Champagne-Ardenne, France	Referee
Prof. Josef Štěpánek	Fac.Math.Phys. Charles University in Prague, Czech Rep.	Supervisor
Prof. Germain Trugnan	ERL INSERM, France	Examiner
Prof. Pierre-Yves Turpin	Université Pierre et Marie Curie, France	Supervisor

I declare that I carried out this doctoral thesis independently, and only with the cited sources, literature and other professional sources.

I understand that my work relates to the rights and obligations under the Act No. 121/2000 Coll., the Copyright Act, as amended, in particular the fact that the Charles University in Prague has the right to conclude a license agreement on the use of this work as a school work pursuant to Section 60 paragraph 1 of the Copyright Act.

In..... date.....

signature

Acknowledgements

I hereby wish to express my deepest gratitude to both of my supervisors, Prof. Josef Štěpánek and Prof. Pierre-Yves Turpin, for their guidance, ever-present optimism and encouragement during the research and writing of this thesis. It has been my honor to work with them.

Special thanks to all the staff members and students of the Laboratoire Jean Perrin and ANbioPhy in France for creating a helpful and friendly atmosphere, especially to Jaroslava Joniová, Veronika Huntošová and Imène Chebbi. Furthermore, I would like to express my sincere gratitude to Christian Zentz for his patience during our discussions on various scientific topics and fluorescence measurements. I owe my thanks to Sergei Kruglik for his kind help with Raman measurements.

For their friendship, support and excellent working conditions I also thank to all members of the Division of Biomolecular Physics at Institute of Physics of Charles University in Prague, especially to Pavla Pečínková, Vlastimil Zíma and Kateřina Hofbauerová. Many thanks belong to Vladimír Kopecký Jr. for his cooperation and guidance in FTIR and Raman measurements and their analysis. I would like to thank to Jiří Bok from the Theoretical Division for development of the software for pre-processing of Raman spectra.

My great thanks belong to Lucie Bednárová from Institute of Organic Chemistry and Biochemistry of the Academy of Sciences of the Czech Republic in Prague for performing some CD experiments for us. I would also like to thank to Yves-Marie Coic from Institut Pasteur in France for synthesis of several model oligopeptides.

Last but not least, my personal thanks belong to my family whose support and patience have been invaluable. The greatest thanks belong to my husband Václav not only for helpful discussions of my research, but also for being there for me all the time. Special thanks belong to my little daughter Lada for making my life more beautiful and wonderful.

I gratefully acknowledge support of the French government scholarship "thèse en cotutelle" of the Ministry of Education of France, the Czech Science Foundation (No. 202/09/0193) and the Grant Agency of Charles University (No. 402111).

Title: Molecular mechanisms of DNA regulatory segment recognition by MADS box family transcription factors

Author: Barbora Profantová –Řezáčová

Department / Institute:

Institute of Physics of Charles University, Faculty of Mathematics and Physics,
Charles University in Prague

École Doctorale Chimie Physique et Chimie Analytique de Paris Centre (ED 388)

Supervisors of the doctoral thesis:

Prof. RNDr. Josef Štěpánek, CSc., Faculty of Mathematics and Physics, Charles
University in Prague

Prof. Pierre Yves Turpin., Laboratoire Jean Perrin, Université Pierre et Marie Curie

Assistant supervisor: RNDr. Vladimír Kopecký Jr., PhD., Faculty of Mathematics
and Physics, Charles University in Prague

Abstract: The thesis deals with physico-chemical properties of the MADS box, binding domain of transcription factors, which are important for the formation of complexes with the DNA regulatory segment bearing the CArG box. The study was performed also on model oligopeptides, selected segments of the MADS box and their analogues with a point mutation. A wide range of spectroscopic techniques was employed, namely absorption, circular dichroism, fluorescence and Raman spectroscopies. Advanced approaches including multivariate methods were used for data processing. The three tyrosines of the MADS box located in amino-acid vicinities of different charge and hydrophobicity, were used as intrinsic spectroscopic probes. The obtained characteristics of the MADS box and its segments structural arrangement, flexibility and acid-base equilibria are the main results of the work.

Keywords: MADS box, optical spectroscopy, factor analysis, protein-DNA interaction, tyrosine

Název práce: Molekulární mechanismy rozpoznání regulačního úseku DNA transkripčními faktory z rodiny MADS box

Autor: Barbora Profantová –Řezáčová

Katedra / Ústav:

Fyzikální ústav UK, Matematicko fyzikální fakulta, Univerzita Karlova v Praze
École Doctorale Chimie Physique et Chimie Analytique de Paris Centre (ED 388)

Vedoucí doktorské práce:

Prof. RNDr. Josef Štěpánek, CSc., Matematicko fyzikální fakulta, Univerzita Karlova v Praze

Prof. Pierre Yves Turpin., Laboratoire Jean Perrin, Université Pierre et Marie Curie

Konzultant: RNDr. Vladimír Kopecký Jr., PhD., Matematicko fyzikální fakulta, Univerzita Karlova v Praze

Abstrakt: Disertační práce se zabývá fyzikálně-chemickými vlastnostmi vazebné domény MADS box transkripčních faktorů, významnými pro tvorbu komplexů s regulačním segmentem DNA obsahujícím CARG box. Studium probíhalo i na modelových oligopeptidech, vybraných kratších segmentech MADS boxu a jejich analogiích s bodovou mutací. Byla využita široká škála spektroskopických technik, jmenovitě absorpční, fluorescenční a Ramanova spektroskopie a spektroskopie cirkulárního dichroismu. Ke zpracování dat byly použity pokročilé postupy včetně multivariačních metod. Tři tyrosiny MADS boxu, nacházející se v okolí aminokyselin s různým nábojem a hydrofobicitou, byly využity jako vnitřní spektroskopické sondy. Výsledkem práce jsou charakteristiky strukturního uspořádání, flexibility a acidobasických rovnováh MADS boxu a jeho vybraných segmentů.

Klíčová slova: MADS box, optická spektroskopie, faktorová analýza, interakce protein-DNA, tyrosin

Titre de la thèse: Mécanismes moléculaires de reconnaissance de segments de régulation de l'ADN par des facteurs de transcription de la famille des "boîtes MADS"

Auteur: Barbora Profantová –Řezáčová

Department / Institute:

Institute of Physics of Charles University, Faculty of Mathematics and Physics,
Charles University in Prague

École Doctorale Chimie Physique et Chimie Analytique de Paris Centre (ED 388)

Directeurs de thèse:

Prof. RNDr. Josef Štěpánek, CSc., Faculty of Mathematics and Physics, Charles
University in Prague

Prof. Pierre Yves Turpin., Laboratoire Jean Perrin, Université Pierre et Marie Curie

Professeur consultant: RNDr. Vladimír Kopecký Jr., PhD., Faculty of Mathematics
and Physics, Charles University in Prague

Résumé: Cette thèse concerne les propriétés physico-chimiques des « Boîtes MADS », séquences de liaison de facteurs de transcription déterminantes pour la formation de complexes avec des segments de régulation de l'ADN comportant des séquences spécifiques nommées « Boîtes CARG ». Des études ont aussi été menées sur certains segments bien choisis des Boîtes MADS et quelques-uns de leurs analogues mutés. Un large choix d'approches spectroscopiques a été employé pour ces études : absorption électronique, dichroïsme circulaire, fluorescence et diffusion Raman. Des approches performantes d'analyse multivariée ont été utilisées pour le traitement des résultats expérimentaux. Les trois tyrosines de la Boîte MADS, situées dans des environnements de charge et d'hydrophobicité différents, ont été utilisées comme marqueurs spectroscopiques intrinsèques. Les principaux résultats de ce travail concernent les caractéristiques de structures, flexibilités et équilibres acido-basiques de la Boîte MADS et de ses différents segments.

Mots clés: MADS box, spectroscopie optique, analyse factorielle, interactions protéine-ADN, tyrosine

Contents

1. THEORY	7
1.1. Transcription of a gene.....	7
1.1.1. Regulation of the transcription initiation	8
1.1.2. Regulation segments of DNA	9
1.1.3. Transcription factors	11
1.2. MADS box family of transcription factors	13
1.2.1. The MADS box.....	14
1.2.2. Biological role of MADS box proteins	15
1.2.3. SRF and its DNA regulatory segment recognition	17
1.2.4. Primary structure of the MADS box of SRF.....	19
1.3. Tyrosine as an inner probe of the MADS box	21
1.3.1. Absorption properties of tyrosine	21
1.3.2. Fluorescence properties of tyrosine	22
1.3.3. Raman characteristics of tyrosine	23
2. OBJECTIVES OF THE THESIS	26
3. EXPERIMENTAL	28
3.1. Samples	28
3.1.1. Model oligopeptides.....	28
3.1.2. Model DNA oligonucleotides	29
3.1.3. Other biomolecules and chemicals	30
3.1.4. Buffers	30
3.1.5. Sample preparation	31
3.1.6. Oligopeptide repurification.....	31
3.2. Experimental techniques	33
3.2.1. Fluorescence spectroscopy.....	33
3.2.2. UV-VIS Absorption spectroscopy	34
3.2.3. Raman spectroscopy	34

3.2.4.	Infrared spectroscopy	36
3.2.5.	Circular dichroism	37
3.2.6.	pH measurement	37
3.3.	Data analysis.....	38
3.3.1.	Factor analysis	38
3.3.2.	Fluorescence quenching analysis	39
3.3.3.	pH titration analysis	40
4.	RESULTS AND DISCUSSION	43
4.1.	Free tyrosine.....	43
4.1.1.	Concentration dependence of free tyrosine.....	43
4.2.	Shorter segments of the MADS box	46
4.2.1.	Fluorescence and absorption pH dependence of CH08 oligopeptide	46
4.2.2.	Fluorescence quenching of the CH08	49
4.2.3.	CD spectra of CH08 oligopeptide.....	51
4.2.4.	Raman spectra of CH08 oligopeptide	52
4.2.5.	Infrared spectra of CH08 oligopeptide.....	55
4.2.6.	Fluorescence and absorption pH dependence of JS01 oligopeptide	57
4.2.7.	CD spectra of JS01 oligopeptide.....	57
4.2.8.	Raman spectra of JS01 oligopeptide	58
4.2.9.	Raman spectra of JS03 oligopeptide.....	60
4.2.10.	Raman spectra of JS02 oligopeptide	61
4.3.	Longer segments of MADS box	62
4.3.1.	Raman spectra of longer oligopeptides.....	62
4.3.2.	Absorption and fluorescence spectra of longer oligopeptides	64
4.4.	MADS box	65
4.4.1.	Fluorescence of the MADS box.....	66
4.4.2.	MADS box fluorescence quenching	67
4.4.3.	Fluorescence and absorption pH dependency of the MADS box	71
4.5.	Peptide/DNA interaction	77
4.5.1.	Addition of the oligonucleotide to the oligopeptide sample	77

4.5.2. Addition of the oligopeptide to the oligonucleotide sample	79
4.5.3. Comparison of the interaction experiments	84
5. CONCLUSIONS	88
6. DISSEMINATION OF THE THESIS RESULTS	91
7. BIBLIOGRAPHY	93
8. LIST OF ABBREVIATIONS	105
9. LIST OF FIGURES	106
10. LIST OF TABLES	111
11. ATTACHMENTS	112

1. Theory

1.1. Transcription of a gene

Genetic information is transcribed from DNA to RNA and then translated from RNA to protein (Figure 1). This fundamental principle, called the central dogma of molecular biology, is obeyed by all types of cells, from bacteria to human [1]. Unlike prokaryotic transcription, eukaryotic transcription takes place in membrane-bounded nucleus, whereas the translation proceeds in the cytoplasm. This spatial and temporal separation enables to regulate gene expression in intricate ways [2].

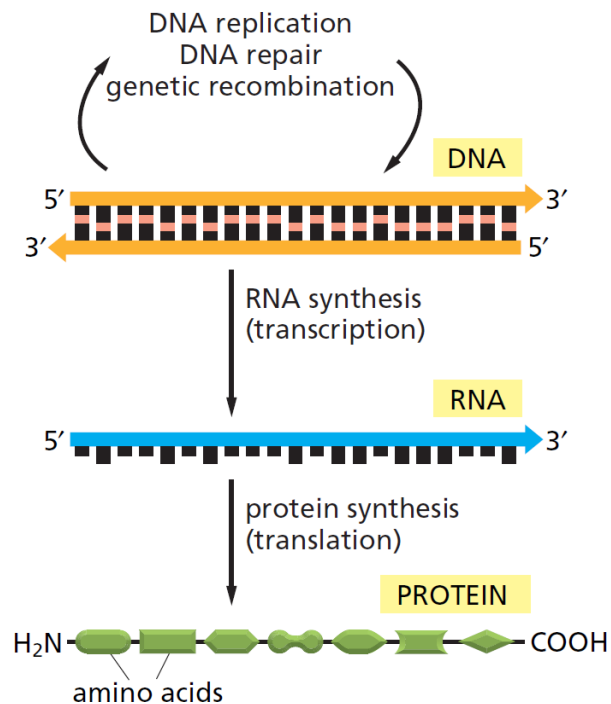


Figure 1. Expression of genetic information [1].

During transcription, the first step of gene expression, an enzyme system converts the information stored in a segment of double-stranded DNA into an RNA strand according to the base complementarity to one of the DNA strands. Transcription is more site selective than the DNA replication and some parts of the DNA are never transcribed. The cell is able to restrict or strengthen the expression of genetic information, thus only the currently needed genes are expressed.

The process of transcription consists of three phases: initiation, elongation and termination. It is initiated by an attachment of RNA polymerase to the DNA template strand at a promoter DNA sequence. Like the DNA polymerase catalysing DNA replication, the RNA polymerase catalyses formation of phosphodiester bonds that link the nucleotides together, forming a linear chain. The RNA polymerase moves along the DNA, unwinding the DNA helix just ahead of the active site exposing a new region of the template strand. It elongates the RNA strand by adding ribonucleotide units (using molecules ATP, CTP, UTP and GTP as substrates) to the 3'-hydroxyl end, synthesizing RNA in the 5'→ 3' direction [3]. Each nucleotide in the newly formed RNA corresponds to Watson-Crick base-pairing scheme. During the elongation, the nucleobases of the growing RNA end pair temporarily with the DNA template, forming a short hybrid RNA-DNA double helix. Just behind the transcribed region, the RNA chain is displaced and the DNA helix is re-formed.

In eukaryotes, the termination of transcription occurs by different processes depending on the type of the RNA polymerase. It can happen by using a termination factor, after a transcription of a termination sequence or it can be even more complex. Next RNA synthesis from the same DNA template can start before the first RNA is complete; therefore many RNA copies usually arise from the same gene in a relatively short time.

1.1.1. Regulation of the transcription initiation

Synthesis of informational macromolecules is highly expensive in terms of energy; therefore the beginning of the pathway is the essential place for its regulation. The initiation of the transcription is thus the main point controlling which protein is to be produced and at what rate. In contrast to bacteria, RNA polymerases of eukaryotes cannot initiate the transcription process without additional proteins and their transcription is mediated and regulated by protein/DNA interactions [1].

The regulation of transcription initiation is often caused by differences in the interaction between RNA polymerase and promoter. Like in the case of bacteria, the sequences of various promoters differ considerably, affecting the binding affinity of RNA polymerases and thus the basal frequency of transcription initiation [3]. In eukaryotes the expression of genes is further modulated by regulatory proteins. Many

of them enhance or repress interaction between RNA polymerase and the promoter. A typical eukaryotic gene has many activator and repressor proteins determining together the rate and pattern of its transcription. To bind a promoter the three eukaryotic RNA polymerases also need a group of general transcription factors (see Figure 2), which must assemble at the specific short DNA sequence (promoter) with the polymerase before the transcription may begin.

Before the initiation of eukaryotic transcription the DNA, densely packed into nucleosomes and higher order forms of chromatin structure, need to be opened and unwound to afford access to RNA polymerases.

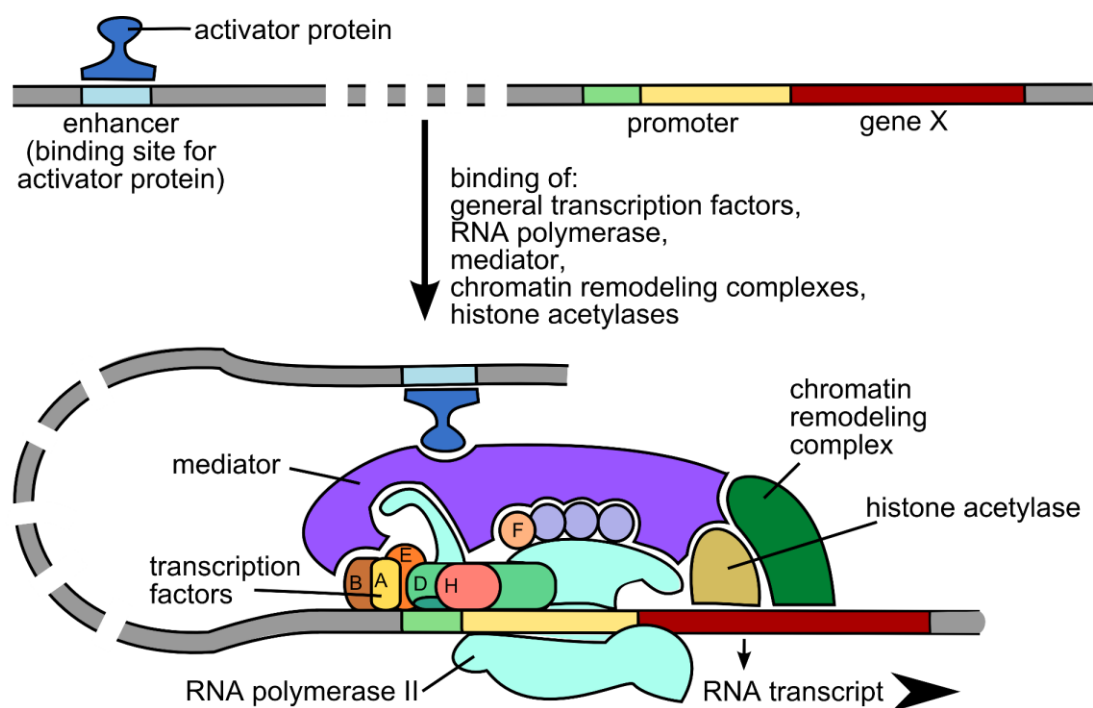


Figure 2. Initiation of transcription in eukaryotic cell (adapted from [1]). Transcription factors are marked as A,B...H.

1.1.2. Regulation segments of DNA

Hundreds of DNA regulation segments have already been identified. Both eukaryotic and prokaryotic genes require promoters for the initiation of the transcription. These DNA sequences are referred as cis-acting elements, meaning they are always on the same molecule of DNA as the regulated gene [2]. A typical gene is usually regulated by a number of cis-regulating segments, some of them are

closer to the coding sequence (proximal promoter region), some of them are placed further (distal) [4].

Each type of eukaryotic RNA polymerases needs its characteristic promoter. RNA polymerase I discerns a single type of promoter, present only in rRNA genes. Polymerase III transcribes from promoters located in the upstream position, embedded in the genes or downstream of the initiation site. Promoters of RNA polymerase II can be either simple or more complex (see Figure 3). They are combinations of short sequence elements usually located in the immediate upstream region of the gene.

Two classes of promoters can be distinguished. The core promoters encompass components directing the basal transcription complex to initiate transcription and allow a constitutive expression of the gene even in the absence of additional regulatory elements, but at very low (basal) levels. They do not need to contain all elements shown in the Figure 3. For example in many of them the initiator element (INR) may substitute a function of the TATA box [5]. Noncore promoters can be found in the core promoter region but are usually located in the sequence upstream of it (proximal or distal promoter regions). They typically contain multiple recognition sites that may operate as enhancer or silencer sequences (see below) modulating the basal transcription level.

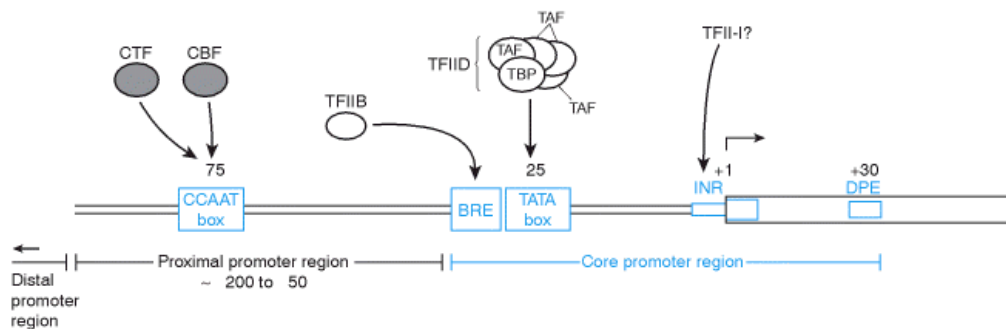


Figure 3. Binding of transcription factors to the regulatory promoter elements in eukaryotes [5]. Abbreviations: TATA box (sequence TATA(A/T)A(A/T)), BRE (TFIIB Recognition Element), DPE (Downstream Promoter Element), CCAAT box (sequence GGCCAATCT).

Enhancers present another type of cis-acting DNA segments. They are able to immensely increase the effectiveness of promoters. Their positions relative to promoters are not fixed and can vary substantially [2]. Silencers on the other hand have an opposite function and serve to reduce the transcription levels.

Response elements modulate transcription in response to external stimuli (specific hormones or intracellular second messengers such as cyclic AMP). They can be usually found at a short distance upstream of promoters [5].

Cis-acting elements are binding sites for transcription factors. Such a protein is sometimes called a trans-acting factor because it may be encoded by a gene on a different DNA molecule than the gene it regulates.

1.1.3. Transcription factors

Transcription factors (TF) are often identified as key metabolic or developmental regulators. They are absolutely necessary for the normal development of a living organism and also for correct functioning of all the processes within its cells. Though they present a variable family of proteins, they are generally defined by their ability to bind specific sequences of DNA and regulate transcription of a gene in time. TFs are active inside the nucleus; their activity is therefore affected by nuclear transport (import/export). Posttranslational modifications like phosphorylation present also an important mechanism controlling their activity (see Figure 4). TFs may also control genes necessary for their own transcription and thus be responsible for their own transcription.

General transcription factors (GTFs), also known as basal, are required for transcription of all genes. They participate in formation of the transcription-initiation complex that binds to promoter region upstream of the regulated gene and interacts directly with the RNA polymerase. They are considered as the most basic set of proteins necessary to activate the gene transcription [5]. The most common GTFs are TFIIA, TFIIB, TFIID, TFIIIE, TFIIF and TFIIH (marked in Figure 2).

Specific TFs stimulate or repress transcription of individual genes by binding to their regulatory sequences [4]. They are especially important during the development of multicellular organisms dictating the fate of individual cells. For example, homeotic genes controlling the pattern of body formation encode a transcription factor instructing cells to form various structures of the body. These genes may activate one gene and repress another, creating effects that are necessary for the proper development of an organism. A mutation of any of these homeotic transcription factors results in incorrect development of the organism.

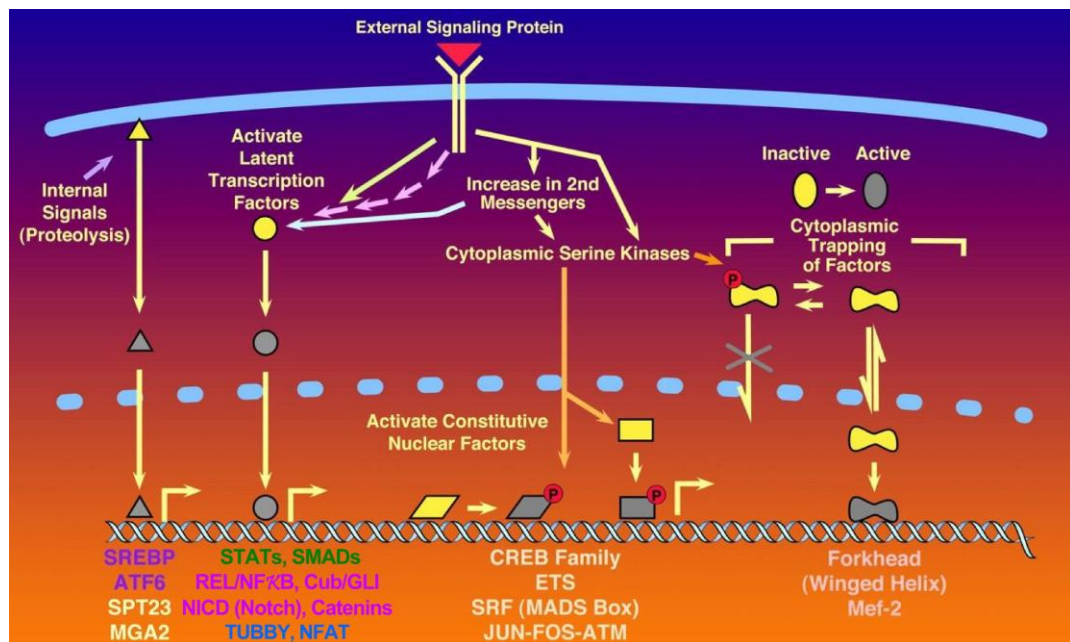


Figure 4. General scheme of response to signals from extracellular signalling proteins through cell surface receptors to the nucleus. Latent cytoplasmatic factors activated by phosphorylation (green), regulated phosphorylation or proteolysis (light purple), and second messenger fluctuations (light blue). Internal signals regulate proteolysis at the plasma membrane liberating some transcription factors (dark purple). Resident nuclear proteins (yellow, □) may be phosphorylated on serine and thus activated either by binding to DNA or free at nucleus) [6].

More than 2000 transcription factors were found encoded in the human genome [6]. They can be classified according to their role within cellular regulatory circuits [6] but they are usually distinguished according to their common structural motives [7-8] (see Figure 5) based on the similarity of sequence and from the tertiary structure of their DNA binding domains.

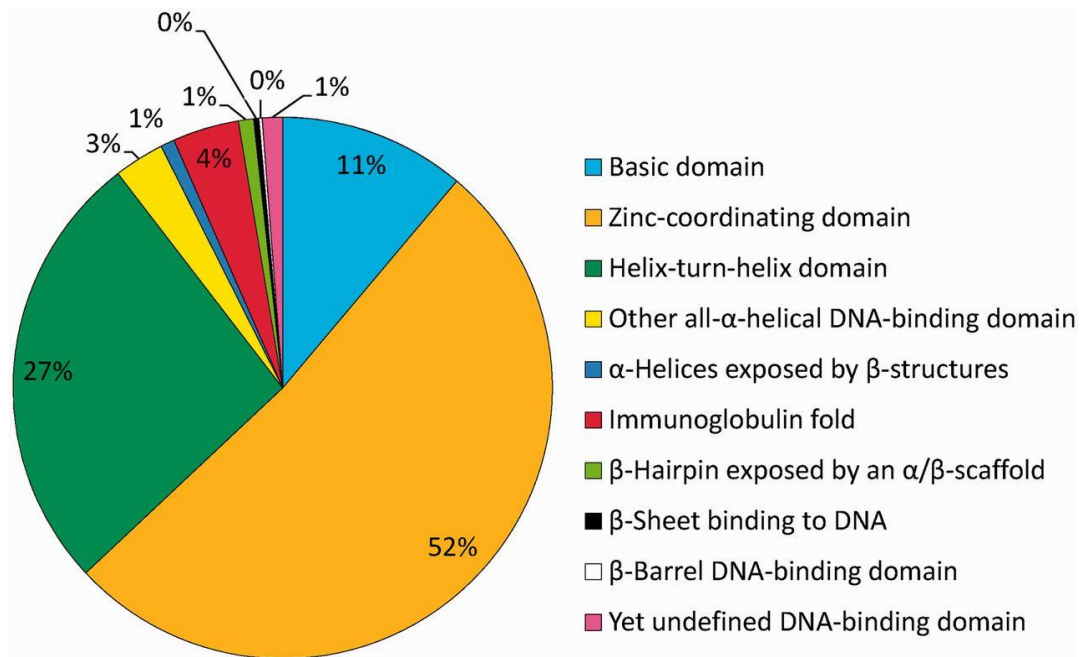


Figure 5. Relative sizes of the 10 human TF superclasses distinguished according to the type of DNA binding domain [7].

1.2. MADS box family of transcription factors

The MADS box family of transcription factors can be distinguished based on the primary sequence similarity amongst a number of proteins from a wide range of eukaryotic organisms [9]. These transcriptional regulators are involved in a diverse range of important biological functions, embryogenesis, flower and root development in plants [10-13], expression of immediate early genes, muscle differentiation and maintenance in animals [14-17], cell type-specific transcription, arginine metabolism and pheromone response in yeast [9, 18-19].

The MADS acronym is derived from abbreviation of its earliest four founded members: MCM1 (Minichromosome Maintenance 1) from the yeast [20], Agamous from the thale cress -*Arabidopsis thaliana* [21], Deficiens from the snapdragon - *Antirrhinum majus* [22] and SRF (Serum Response Factor) from the human [23].

Within the class of MADS box factors we distinguish two families: type I of SRF-like proteins that are mainly responders to external signals (like SRF and yeast RLM1) [7-8]; type II of MEF2-like (Myocyte Enhancer Factor) regulators of differentiation, homeotic genes and yeast regulators.

In addition to the MADS box domain, these factors share a loose sequence similarity in another region called SAM domain for the SRF-like proteins (e.g., SRF, ARGRI, and MCM1) and MEF2 domain for the MEF2-like proteins [9]. In plants, the MEF-like proteins are also called MIKC-type proteins referring to comprised domains: (M) MADS, (I) an intervening domain, (K) a keratin-like domain and (C) a C-terminal region [24-25].

1.2.1. The MADS box

The MADS box is constituted by a conserved sequence of 56 amino acids shared within the members of the family (see Figure 6). Several members of this family have been shown to form dimers. Two functional segments within the sequence have been determined: the N-terminal basic half of the MADS box presents the DNA binding domain whereas the C-terminal hydrophobic segment forms a protein dimerization domain.

The X-ray structures of several members of MADS box family of transcription factors bound to their DNA consensus (human SRF [26-27], yeast MCM1 [28], MEF2a [29-30]) have revealed that their overall structures are very similar, but with differences in DNA binding.

Generally the MADS box proteins bind to similar A/T rich DNA regions, however there are distinctive consensus sequences: SRF binds as a homodimer specifically to a 10-bp cis element known as the CArG-box of sequence CC(A/T)₆GG [31], whereas MEF2-like proteins binds as homo- or heterodimer to another 10-bp segment CTA(A/T)₄TAG called MEF2 site [32].

Some members of MADS box family particularly recruit other transcription factors and form regulatory multi-protein complexes: SRF/TCF [33], MCM1/MAT α 2 [34] and MEF2/MyoD [35]. The interaction with other auxiliary proteins is common for the MADS box family of transcription factors and plays a crucial role in the regulation of the target genes.

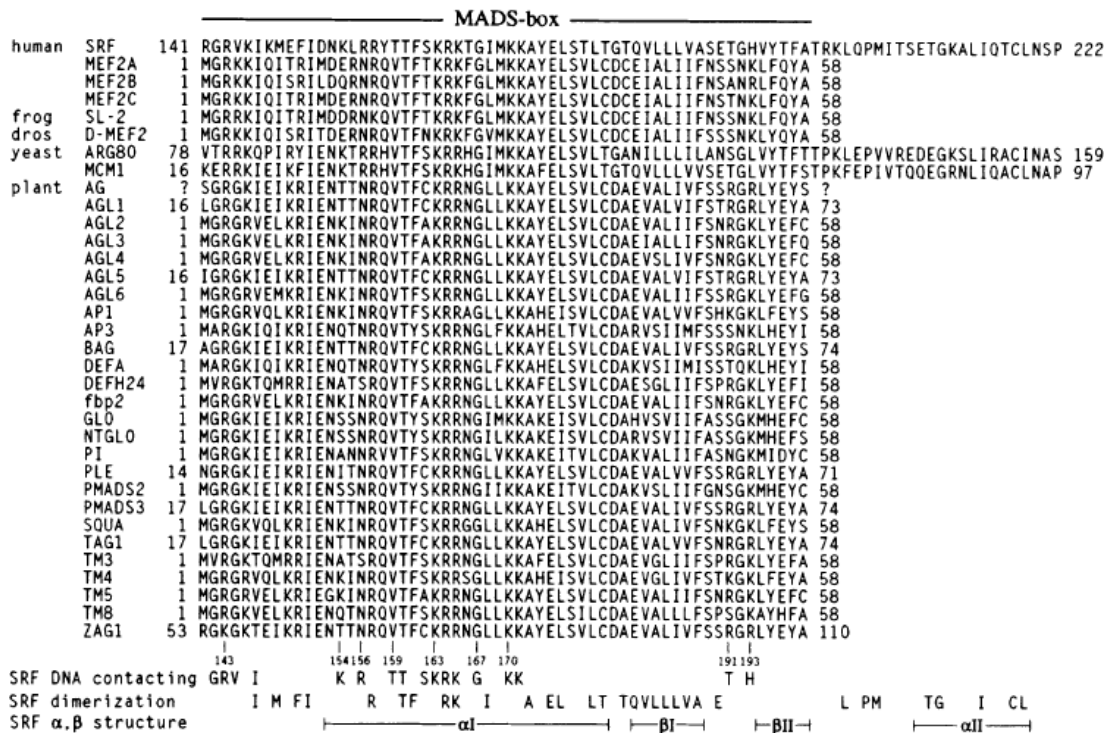


Figure 6. Protein sequences of non-identical MADS domains aligned to show their homology. The amino acid positions involved in DNA contacts, dimerization interactions and α, β structure are indicated below for the core SRF [26].

1.2.2. Biological role of MADS box proteins

In yeast, the MCM1 can act both as an activator or repressor in the regulation of many genes involved in arginine metabolism, mating or cell cycle depending on the proteins it attracts [36]. It plays a crucial role in the control of the cell cycle at both G2/M and M/G1 transitions by interacting with the Yox1, Yhp1 or Fkh2 proteins [37-38], transcription of cell-type specific genes in cooperation with the MAT α 1 activator and the MAT α 2 repressor [39], in the pheromone response mediated by the STE cofactors [19, 40] and together with Arg80 a SRF-like protein serve as an additional regulating factor in the arginine metabolism [41].

In plants, the representation of MADS box containing proteins is rather extensive, forming a group of homeotic transcription factors. Initially they have been found to participate in the floral organ specification from root to flower and fruit, but more recent studies disclosed their functions in the morphogenesis of almost all organs throughout the life cycle of the plant, from vegetative to reproductive growth, determining the identity of the floral meristem, ovules and root development

[24, 42-43]. The MADS-box gene family with more than 100 genes in representative flowering plant genomes is significantly larger than that found in animals or fungi [43]. The best studied plant MADS box genes are those determining floral identity in *Arabidopsis* and *Antirrhinum* [22, 44] (Figure 7).

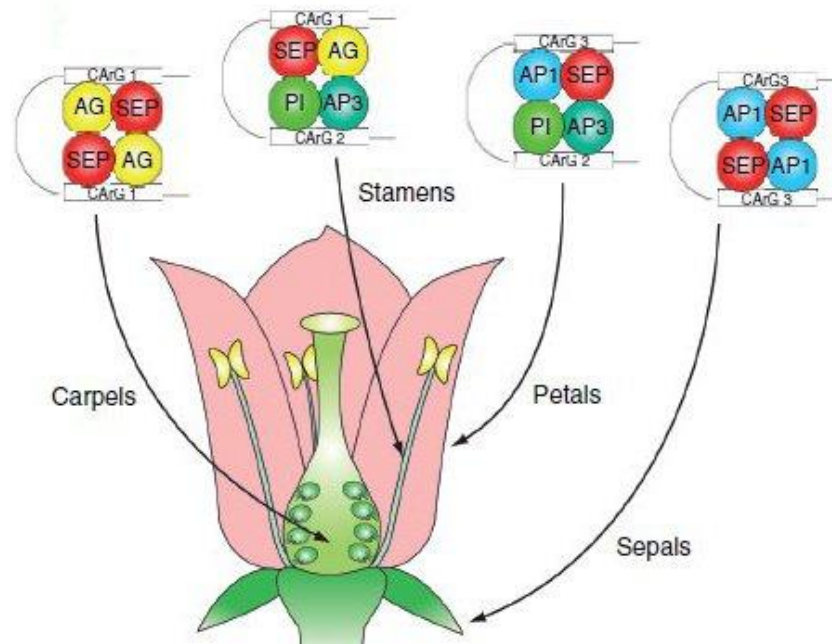


Figure 7. Structure of MADS-domain proteins and their function in determining floral organ identity [45]. Structures of 'floral quartets'. Multimeric complexes of MIKCC-group proteins, bound to two DNA sequence elements (CARG-boxes) present in numerous target genes, determine floral organ identity.

In animals the SRF-like MADS box factors are involved in the regulation of many immediate early genes involved in the mitogenic response of proliferative cells [46]. They are also important in the control of gene tissue specificity and the response to hypertrophic growth stimuli of muscle genes expressed in post-replicative myocytes [47-50]. Additionally to DNA binding and dimerization domains, these factors contain a C-terminal transcription activation domain. The transcription activation also requires additional accessory proteins in response to extracellular signals such as growth and differentiation signals [51].

Similar to SRF the MEF2-like factors also regulate the transcription of genes necessary for muscle differentiation and cell proliferation in animals. In mammals there are four MEF2 genes (A, B... D) expressed in distinct but overlapping patterns during embryogenesis and in adult tissues [52-53]. In mice, inactivation of the MEF2C gene leads to cardiac morphogenetic defects, vascular abnormalities and

lethality by embryogenetic day 10 [54]. In contrast to mammals, *Drosophila* has only one D-MEF2 gene, its mutation results in embryos lacking differentiated skeletal, cardiac and visceral muscle cells [55].

1.2.3.SRF and its DNA regulatory segment recognition

The Serum Response Factor (SRF), one of the founding members of the MADS box family of transcription factors, plays an important role in the control of differentiation and proliferation in mammalian cells. SRF was firstly identified due to its role in the regulation of immediate early genes in response to growth factor induction [46, 56]. Later on it was found to regulate also the expression of muscle-specific genes [47]. Since then there has been a large number of studies on SRF-dependent gene expression and on promoters containing its binding site. These studies assisted in identification of more than 150 genes regulated by SRF in mammals [14]. In addition to the immediate early genes, SRF controls genes coding components of the actin cytoskeleton and the muscular contractile apparatus [57]. The regulation of such a vast number of different genes proceeds through combinatorial interactions with several signal regulated and tissue specific regulatory cofactors (for example see Figure 8) [58].

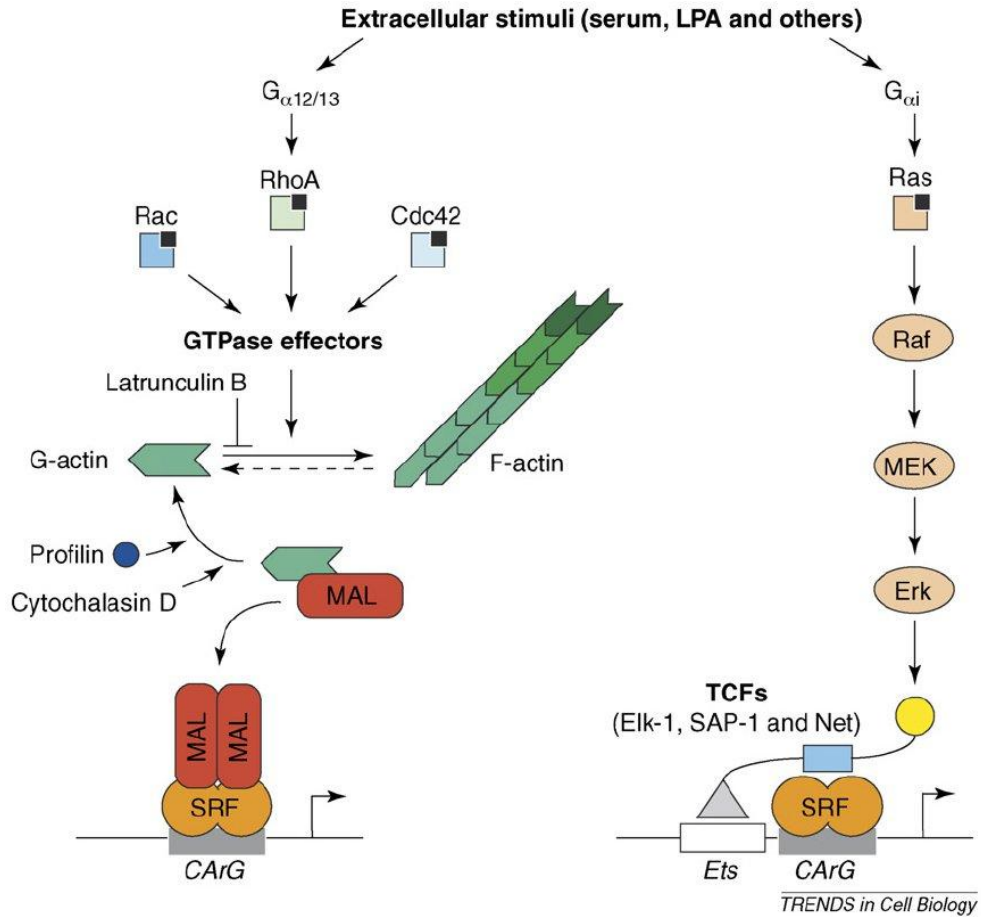


Figure 8. Model of two principal pathways regulating SRF activity in non-muscle cells [58].

The SRF is a 508 amino acids long protein and its core domain (residues 132-223) is sufficient for DNA binding, dimerization and interaction with other accessory factors [23, 59]. The sequence is shown in the Figure 9. The core SRF includes the MADS-box, a C-terminal transcriptional activation domain and a N-terminal domain that can be phosphorylated by kinases.

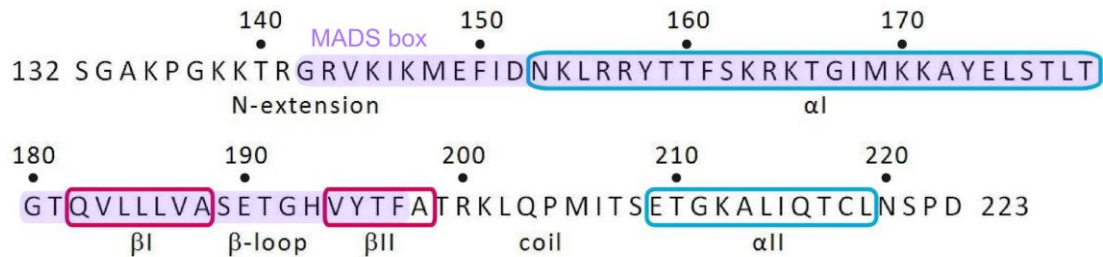


Figure 9. Core SRF sequence (residues 132-223). The α and β secondary structure assignment are boxed, MADS box region is marked by purple (according to Pellegrini, et al. [26]).

SRF binds as a homodimer to the serum response element (SRE), which contains the CArG box segment, having the sequence CC(A/T)₆GG [60]. The X-ray structure of the core SRF domain bound to DNA was solved by Pellegrini et al. in 1995 [26] (see Figure 10).

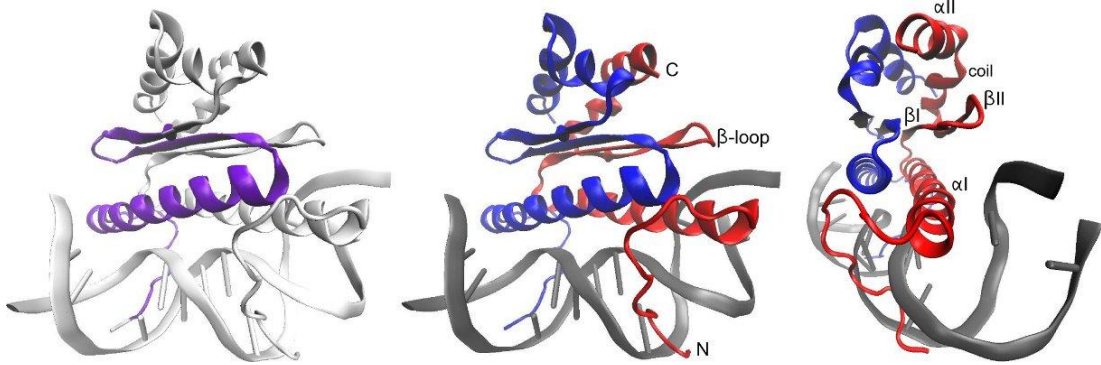


Figure 10. The core SRF/DNA complex (PDB file 1srs [26] visualized by VMD [61]). Left: Position of the MADS box within the core SRF (marked by violet colour). Middle: View perpendicular to the molecular two-fold and overall DNA helix axes. Right: View revealing the stab-like structure of the monomers. The two SRF-core monomers (blue and red) have highly similar conformations. DNA recognition segment is in dark grey colour (middle and right).

In the DNA-bound dimer, the core SRF forms two antiparallel amphipathic alpha-helices αI oriented approximately parallel on the minor groove. These helices make minor and major groove contacts, while the N-terminal extensions form minor groove contacts with the DNA. The bound DNA is bent and wrapped around the protein, but it was shown by following studies on core SRF with 20mer SRE that the oligonucleotide does not stay in a stable bending conformation in solution and keeps switching between bent and linear conformations [62]. It exhibits a compressed minor groove in the center and widened minor groove in the flanks.

1.2.4. Primary structure of the MADS box of SRF

The MADS box is constituted by a conserved sequence of 56 amino acids. The knowledge of their chemical properties may be essential to understand the biochemistry of the oligopeptide. Amino acids are usually divided into five main classes based on the properties of side chains (R groups), in particular, on their polarity or tendency to interact with water at biological pH. The hydrophathies and dissociation constants of the MADS box amino acids are shown in Table 1.

Table 1. Properties of amino acids within the SRF MADS box.

^a pKa of R groups of titratable amino acids; taken from [3].

^b A scale combining the hydrophobicity and hydrophilicity of R group which can be used to measure the tendency of the amino acid to seek aqueous environment (values > 0) or avoid it (values < 0); according to Hopp–Woods hydrophobicity scale [63].

SRF residue	Amino acid	pKa ^a R group	Δ Charge	Hydrophathy ^b	SRF residue	Amino acid	pKa ^a R group	Δ Charge	Hydrophathy ^b
142	G Gly			0.0	170	K Lys	10.53	1 → 0	3.0
143	R Arg	12.48	1 → 0	0.2	171	K Lys	10.53	1 → 0	3.0
144	V Val			-1.5	172	A Ala			-0.5
145	K Lys	10.53	1 → 0	3.0	173	Y Tyr	10.07	0 → -1	-2.3
146	I Ile			-1.8	174	E Glu	4.25	0 → -1	3.0
147	K Lys	10.53	1 → 0	3.0	175	L Leu			-1.8
148	M Met			-1.3	176	S Ser			0.3
149	E Glu	4.25	0 → -1	3.0	177	T Thr			-0.4
150	F Phe			-2.5	178	L Leu			-1.8
151	I Ile			-1.8	179	T Thr			-0.4
152	D Asp	3.65	0 → -1	3.0	180	G Gly			0.0
153	N Asn			0.2	181	T Thr			-0.4
154	K Lys	10.53	1 → 0	3.0	182	Q Gln			0.2
155	L Leu			-1.8	183	V Val			-1.5
156	R Arg	12.48	1 → 0	3.0	184	L Leu			-1.8
157	R Arg	12.48	1 → 0	3.0	185	L Leu			-1.8
158	Y Tyr	10.07	0 → -1	-2.3	186	L Leu			-1.8
159	T Thr			-0.4	187	V Val			-1.5
160	T Thr			-0.4	188	A Ala			-0.5
161	F Phe			-2.5	189	S Ser			0.3
162	S Ser			0.3	190	E Glu	4.25	0 → -1	3.0
163	K Lys	10.53	1 → 0	3.0	191	T Thr			-0.4
164	R Arg	12.48	1 → 0	3.0	192	G Gly			0.0
165	K Lys	10.53	1 → 0	3.0	193	H His	6	1 → 0	-0.5
166	T Thr			-0.4	194	V Val			-1.5
167	G Gly			0.0	195	Y Tyr	10.07	0 → -1	-2.3
168	I Ile			-1.8	196	T Thr			-0.4
169	M Met			-1.3	197	F Phe			-2.5

From the three common aromatic amino acids photosensitive in the middle UV region, there are no tryptophan but three tyrosines and three phenylalanines within the sequence of the MADS box. Due to the low absorption and quantum yield of the phenylalanine, the tyrosines can be used as spectroscopic inner probes sensitive to changes in their environment. It is expected that the spectroscopic characteristics of individual tyrosines largely differ from each other due to the different charges and hydrophobicities of amino acids in their proximity. Tyr195 is situated in the most hydrophobic environment according to Hopp–Woods hydrophobicity scale [63]. Tyr158 is in proximity of two positively charged arginines

(Arg156, Arg157) and Tyr173 is close to two positive lysines (Lys170, Lys171) and one negative glutamic acid (Glu174).

1.3. Tyrosine as an inner probe of the MADS box

Tyrosine can be used as an intrinsic fluorophore and thus to serve as a spectroscopic probe of the MADS box. L-tyrosine exists in the protonated form at neutral pH, its phenolic hydroxyl group has the dissociation constant value of 10.07 [3].

1.3.1. Absorption properties of tyrosine

Tyrosine has two main absorption bands in the region between 200 and 300 nm (see Figure 11). The theoretical interpretation of the UV absorption transitions of its phenol ring is that the lowest energy singlet transition of tyrosine is due to the $1L_b$ band, having a maximum near 277 nm and the much stronger $1L_a$ band near 223 nm (see Figure 12) [64]. Hydrogen bonding is expected to cause a shift to lower energies (red shift) since the absorption transitions to the $1L_a$ and $1L_b$ are of $\pi \rightarrow \pi^*$ type [64-66]. It has also been shown that the hydrogen bonding and solvation increase the extinction [67]. The extent of these changes depends upon the degree of the chromophore interactions with polar solvents.

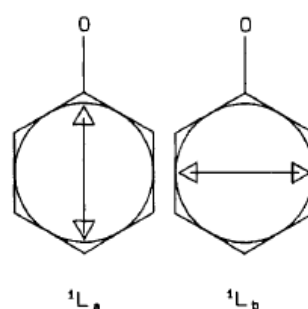


Figure 11. Orientations of the absorption transition moments of the tyrosine lowest-energy singlet-singlet electronic transitions [64].

In a hydrogen bond the phenolic hydroxyl group can act both as a proton acceptor and donor. Aromatic alcohols are hydrogen bonded in water, but if stronger proton acceptors are present, other hydrogen bonds can be formed causing further shifts of the absorption bands. A loss of the hydrogen on a phenol hydroxyl group in

tyrosine shifts the absorption peak at 275 nm to 294 nm and the 223 nm peak to 240nm. The molar extinction coefficients for the 275 nm band increase from about 1400 cm^{-1}/M to 2350 cm^{-1}/M and for the 223 nm band from about 8200 cm^{-1}/M to about 11000 cm^{-1}/M [64].

1.3.2. Fluorescence properties of tyrosine

The fluorescence and phosphorescence emissions of a protein are the sums of contributions from the three aromatic amino acids: tryptophan, tyrosine, and phenylalanine. These three residues have distinct absorption and emission wavelengths and also differ in their quantum yields and lifetimes. Their excitation and emission spectra are shown in Figure 12.

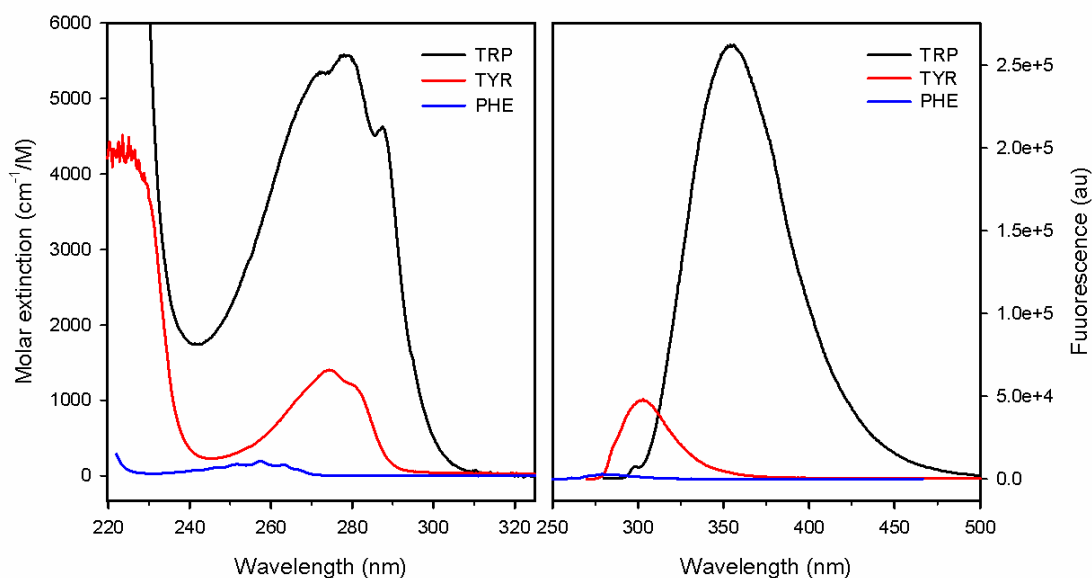


Figure 12. Absorption and emission spectra of aromatic amino acids [68].

The MADS box of SRF has no tryptophan, three phenylalanines and three tyrosines. Considering that phenylalanine has very weak absorption and emission in comparison to tyrosine, we can completely avoid phenylalanine emission by choice of an excitation wavelength above 270 nm.

The tyrosine fluorescence emission spectrum is a single unstructured band with a maximum near 303 nm. Deprotonation of the phenol hydroxyl group leads to a large red shift of the spectrum to about 340 nm and a dramatic decrease of the fluorescence intensity [69].

1.3.3. Raman characteristics of tyrosine

In the Raman spectrum of a protein, there are bands assignable to the tyrosine residues, some of them being nearly free from overlapping of other Raman bands. Raman spectra of L-tyrosine at pH 13 and 1 are shown in Figure 13 [70]. (Tyrosine is not enough soluble at neutral pH to give a concentration sufficient for Raman measurement.) As can be seen, the loss of the hydrogen at Tyr phenol group leads to shifts and intensity changes of several peaks.

The difference between the neutral and negatively charged forms of Tyr is most prominent on the in-plane stretching vibrations $\nu(\text{C}=\text{C})$ of the ring [71-72]. At neutral pH, the pair of bands $\nu_{8a} \sim 1620 \text{ cm}^{-1}$ and $\nu_{8b} \sim 1600 \text{ cm}^{-1}$ (according to the nomenclature of benzene ring modes by Wilson [73] see Figure 14 for the detailed band assignment) are observed while at basic pH only one strong band $\nu_{8a} \sim 1600 \text{ cm}^{-1}$ is present [74].

Moreover, additional information on the ionic form of the hydroxyl group may be provided by a change in the ratio of the bands assigned to the Fermi resonance between the symmetric ring-breathing deformation $\delta(\text{CCC})$, $\nu_1 \sim 850 \text{ cm}^{-1}$ and the overtone of the nonplanar ring vibration $\gamma(\text{CCC})$, $2 \times \nu_{16a} \sim 830 \text{ cm}^{-1}$ [71, 75]. When the phenolic hydroxyl group is a strong hydrogen-bond donor the ratio $I_{850}/I_{830} = 0.3$, when it functions as both a donor and an acceptor $I_{850}/I_{830} = 1.25$ and when it is a strong hydrogen-bond acceptor $I_{850}/I_{830} = 2.5$ [75-76].

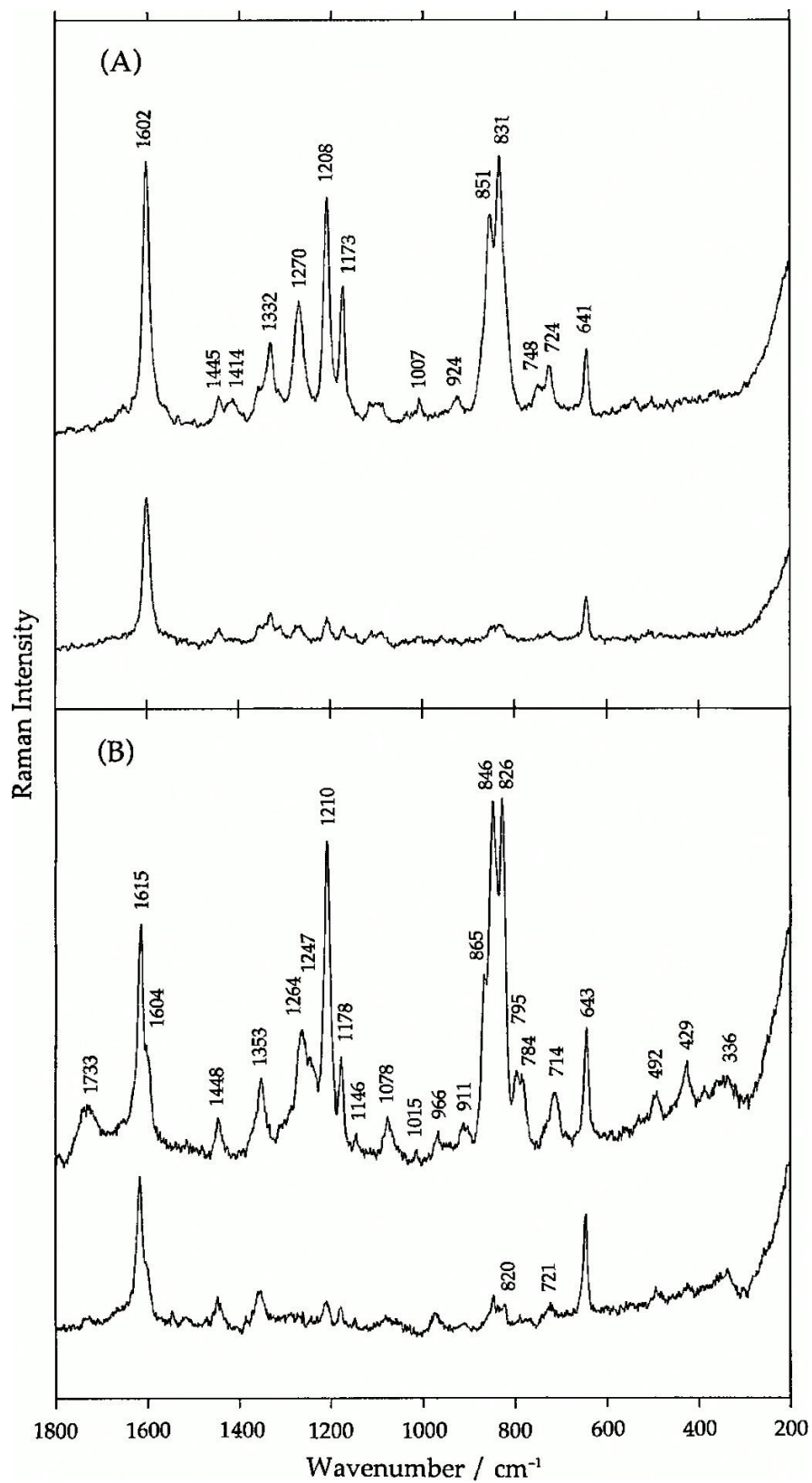


Figure 13. Polarized Raman spectra of L-tyrosine in aqueous solutions of pH 13 (A) and pH 1 (B). Upper curves: the scattered radiation polarized parallel to the polarization direction of the exciting radiation. Lower curves: the scattered radiation polarized perpendicular to the polarization direction of the exciting radiation [70].

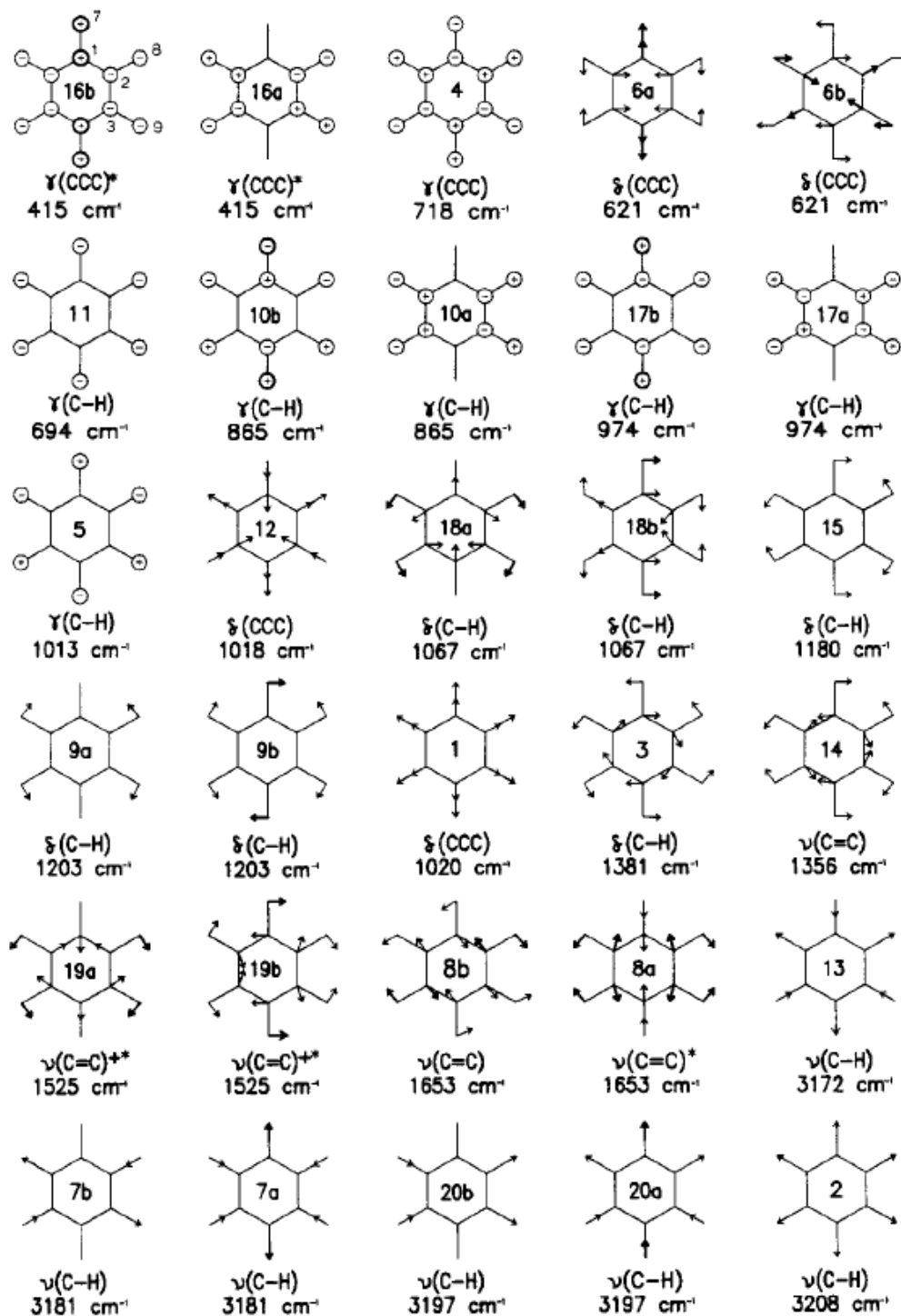


Figure 14. Nomenclature of the ring modes in benzene molecule [73, 77].

(*) The motions appears as (CCC+CH). (+) Vibration degenerated according to Scherer [73].

ν : stretching, δ : in-plane deformation, γ : out-of-plane deformation vibrations.

2. Objectives of the thesis

As follows from the introduction, the MADS box represents a significant family of transcription factors which is widely studied (see Figure 15). Yet still not much is known about the process of DNA recognition and the mechanism of DNA binding. It is now obvious that the structural arrangement of both the DNA chain and the MADS box protein are closely related in the recognition process and that both partners are influenced and maybe even controlled by the state of their hydration shell and its ionic content.

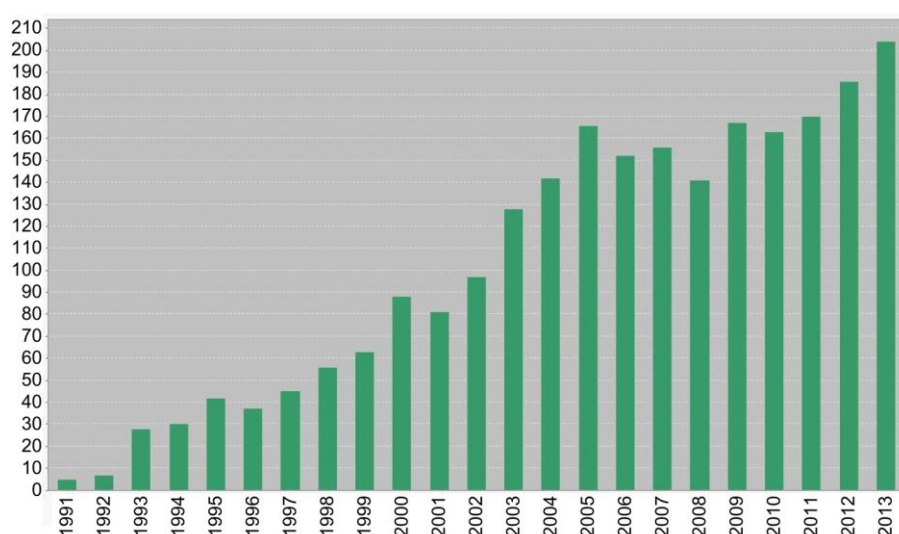


Figure 15. Published articles concerning the MADS box in each year. (Taken from the Web of Science; topic = "MADS box".)

The aim of this study is to gain a deeper understanding of the structure, behaviour and basic functional properties of model oligomers in water solution. The conserved MADS box motif, its shorter segments and analogues with a point mutation are used as basic models for studies of common functional properties of all the protein family. We focus on a number of physico-chemical characteristics of selected molecules; particularly the acid-base equilibria and effect of concentration of selected ions are examined. Essential is also the developed methodology applicable on low amounts of sample that employs fluorescence spectroscopy in combination with UV absorption, Raman and FTIR spectroscopies. Model DNA oligonucleotides are used for pilot interaction experiments.

The French and Czech research groups have built an intensive collaboration on several research projects concerning physico-chemical properties of important

biomolecules and their systems. Within the few last years, structural and dynamical aspects of the transcription factors and their interactions with their DNA target became a new theme of the research cooperation [62]. This thesis that was enabled by a French government scholarship “de doctorat en cotutelle” represents a continuation of this long-term collaboration.

Most of oligopeptides (JS01-6) were purchased from Apigenex (Prague, Czech Republic). Purity and mass weight were tested by HPLC and MS.

MADS box and CH08 were synthesized by Yves-Marie Coïc at Institut Pasteur (Paris, France) according to the Fmoc/tBu solid-phase strategy [98] on a 433A peptide synthesizer (Applied Biosystems) using a Fmoc Polystyrene AM RAM resin (RAPP Polymere, Tübingen, Germany) and Fmoc Amide Resin (Applied Biosystems) respectively. The mass characterization of the purified CH08 oligopeptide was in agreement with the expected value (above 98 % by RP-HPLC). The purified MADS box was quantified by amino acid analysis (total yield 0.72 %) and characterized by positive ion electrospray ionisation mass spectrometry. The experimental data (6512 ± 29 Da) was consistent with the expected mass (6512 Da). The stability of the peptide was checked by fluorescence emission spectra at concentration 1×10^{-5} M.

3.1.2. Model DNA oligonucleotides

For peptide/DNA interaction studies short SRE segments were used as model oligonucleotides. As was revealed in our previous work [78] the original SRE sequence forms a hairpin. Therefore, analogue sequences were also used. These oligonucleotides shared the same DNA base composition as SRE but differed in the order of bases which prevented them to form intramolecular hairpins. Self complementarity of proposed oligonucleotides was checked using Oligo Calc: Oligonucleotide Properties Calculator [79]. All oligonucleotides (see Table 3) were commercially synthesized and purified at Central-European Technology Institute of the Masaryk University (Brno, Czech Republic).

Table 3. Summary of model oligonucleotides. *Extinction coefficients of single stranded (ss) and double stranded (ds) oligonucleotides were calculated using the nearest neighbour model [80].

	Sample	Length	DNA sequence (5' to 3')	Mw (g/mol)	Yield (μ mol)	ϵ_{260}^{ss} * (l/mol/cm)	ϵ_{260}^{ds} * (l/mol/cm)
1	SREfos	20	GGA TGT CCA TAT TAG GAC AT	6156	1.29	202700	320715
2	SREfoscompl	20	ATG TCC TAA TAT GGA CAT CC	6076	1.18	196100	320715
3	modSRE	20	GAG TAG CAT CTT AGG ACA TT	6156	1.49	201500	317659
4	modSREcompl	20	AAT GTC CTA AGA TGC TAC TC	6076	1.37	193500	317659

3.1.3. Other biomolecules and chemicals

L-Tyrosine (Sigma Aldrich) was used in pilot measurements as a testing molecule, e.g. to estimate the effect of various fluorescence quenchers or to verify our new approach for the determination of pKa constants. Due to its low solubility it was used only in fluorescence and absorption experiments.

Other chemicals like KOH (Normapur) and HCl (Merck) of various molarity were used to alter the pH of the sample.

NaCl (Merck) was used at the peptide/DNA interaction experiments in reference solutions.

Ammonium trifluoroacetate (TFA) (Sigma Aldrich) was measured by Raman spectroscopy in order to determine the impurities from the synthesis of oligopeptides.

CsCl, KI and dichloroacetamide (DCA) (all Sigma Aldrich) were used in quenching experiments.

3.1.4. Buffers

For spectroscopic measurements at different pH four different buffer stock solutions were prepared: (A) 50 mM cacodylate buffer pH 7.0 and 6.5 (prepared using $(\text{CH}_3)_2\text{AsO}_2\text{Na}\cdot 3\text{H}_2\text{O}$ (Sigma Aldrich) and HCl (Merck)), (B) 250mM phosphate buffer pH 7.1 (prepared using $\text{NaH}_2\text{PO}_4\cdot\text{H}_2\text{O}$ (Sigma Aldrich) and Na_2HPO_4 (Sigma Aldrich)), (C) 50mM acetate buffer pH 3.2 (prepared using glacial acetic acid (Penta) and CH_3COONa (Lachema)) and (D) 50 mM sodium bicarbonate buffer pH 11.0 (prepared using NaOH (Fluka) and Na_2CO_3 (Lachema)). Buffers A, C, and D were used in majority of Raman, fluorescence, absorption and circular dichroism measurements. Buffer B was used in peptide/DNA interaction experiments.

3.1.5. Sample preparation

Both oligopeptides and oligonucleotides were delivered in a form of lyophilisate. Samples with desired concentration of the studied molecules were prepared by two consecutive dilutions. A stock sample solution was prepared by addition of a small amount of deionized water (0.1 ml) to the sample. In the second dilution a buffer and/or deionized water were used depending on type of experiment. For every sample a reference solution, consisting of the same amount of buffer and deionized water was also prepared.

DNA duplexes were prepared by an annealing procedure. Two complementary single strands in equal molar amounts were mixed in the solvent, then heated to 70° C for 40 min. and after gradually cooled (2 hours) to room temperature. The resulting product was stored frozen at (-20°C).

3.1.6. Oligopeptide repurification

All oligopeptide samples contained small remains of trifluoroacetic acid (TFA) used in Fmoc synthesis to cleave the peptide from the resin and in HPLC purification. TFA persists in the oligopeptide as ammonium trifluoroacetate, bound to cationic amino acids (Lys, Arg...). The salt dissociates in solution and rebinds while drying, which is why it is not detected by mass spectrometry used for the quality control of the synthesised product.

The standard procedure, consisting of several freeze-drying cycles in the presence of HCl excess (stronger acid than TFA) was performed for oligopeptide samples. The procedure was checked up on one of the longer oligopeptides - JS06. By means of Raman spectrum recorded after each step of the procedure, the remaining of TFA was monitored simultaneously with verification that the oligopeptide is not degraded (see Figure 17).

In each cycle i of TFA elution a HCl was added to an eppendorf tube with known amount of JS06 oligopeptide, so that $n_{HCl,i} \gg n_{JS06,i}$. Solution was vortexed, stirred for about 10 minutes and then lyophilized. Sample was then dissolved in water. Small amount of the solution was taken and measured by Raman spectroscopy

(see Figure 17). HCl was added to the rest of the solution and the whole process was repeated. Each cycle of the elution may be characterized by elution ratio.

$$d_i = \prod_1^i \frac{n_{HCl,i}}{n_{JS06,i}}; i = 1, 2, \dots, N;$$

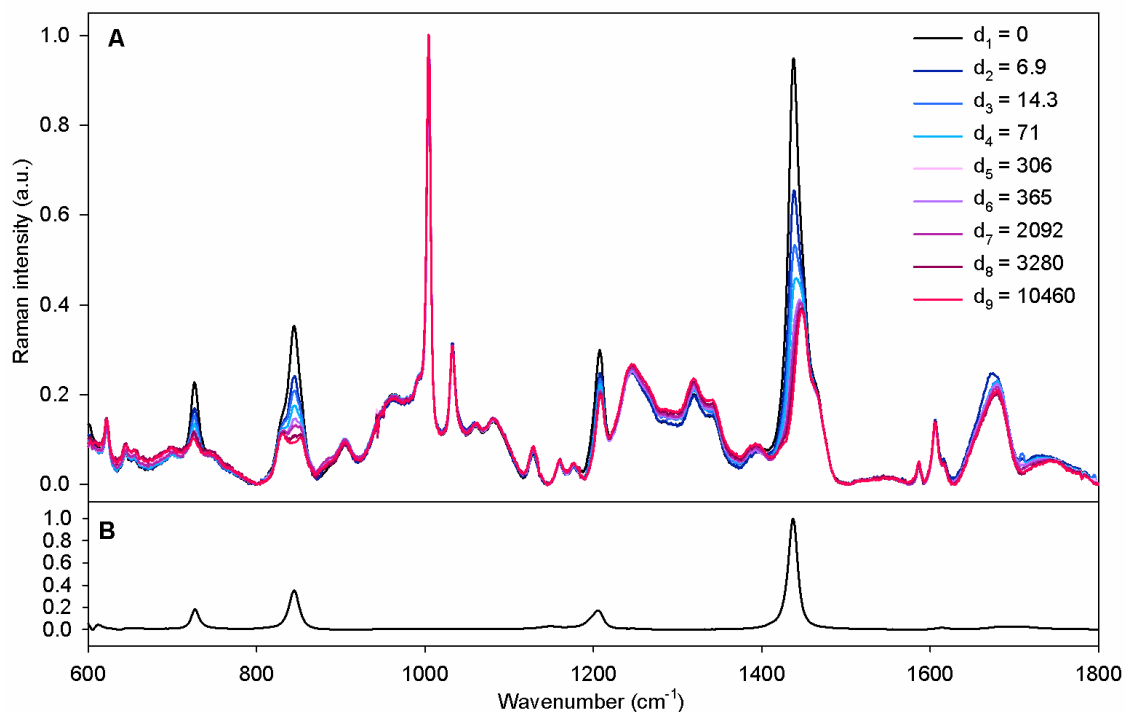


Figure 17. A) Raman spectra of oligopeptide JS06 in water measured after each step of repurification. Spectra are normalized at 1004 cm⁻¹ band. B) Raman spectrum of ammonium trifluoroacetate in water.

3.2. Experimental techniques

3.2.1. Fluorescence spectroscopy

Most of the fluorescence measurements were performed on a SLM Aminco-Bowman series 2 luminescence spectrometer at UPMC. The excitation and emission spectral bandwidths were 4 nm. Emission spectra were measured with a scan rate of 1 nm / sec in the wavelength range 290 - 380 nm. The excitation wavelength was 275 nm for pH titration and protein / DNA interaction experiments, and 278 nm for fluorescence quenching. Excitation spectra of several oligopeptides were measured for emissions at 293, 304 and 325 nm with a scan rate of 1 nm / sec, in the spectral regions below corresponding to emission wavelengths.

Complementary measurements were performed on a Jobin Yvon Spex FluoroMax 2 fluorescence spectrophotometer at Charles University. The excitation and emission spectral bandwidths were 4 nm, excitation wavelength 275 nm and scan rate 10 nm / 1 sec.

Samples were measured in a quartz 10 mm square cuvette (Hellma). Both spectrophotometers were equipped with a thermostated cell holder and a magnetic stirrer.

For acid-base titration measurements the samples were diluted in deionised water. Small amounts of KOH or HCl of various molarity were added gradually to the solution in order to sensitively alter the pH in the range from 3 to 12. After each addition of pH changing solution, the pH value was checked and the sample was placed in a thermostated holder in a fluorimeter and stirred magnetically for 6 min. Then the fluorescence and absorption spectra were recorded. After that pH of the solution was measured again and compared with the value before the spectral measurement. Spectra of reference solution (consisting of the same amount of water, HCl and KOH) undergoing the same procedure was measured immediately after the sample.

Recorded fluorescence spectra were corrected for the Rayleigh and Raman scatterings as well as for the small changes of the sample concentration resulting from addition of quenchers or pH changing solutions. The inner filter effect (IFE) was also corrected taking the optical density at the excitation (OD_{EX}) and emission (OD_{EM}) wavelength into consideration in accordance with [81]

$$\frac{F_{corr}}{F_{obs}} = 10^{\frac{OD_{EX} + OD_{EM}}{2}} \quad (3.1)$$

Maximal absorbance was 0.2 in the spectral range of fluorescence excitation and emission, limiting the concentration of the sample. It was ranging from $8 \cdot 10^{-5}$ M for the shortest oligopeptides with just one tyrosine to $5 \cdot 10^{-6}$ M for the whole MADS box.

Fluorescence quenching was investigated in a 25 mM cacodylate buffer by adding increasing amounts of quenchers Γ , Cs^+ or DCA. A small amount of $\text{S}_2\text{O}_3^{2-}$ ($\sim 10^{-4}$ M) was added in the case of iodide anion to prevent I^{3-} formation. Fluorescence spectra were corrected for the solvent background and for small changes of the sample concentration resulting from the addition of the quencher (dilution method).

3.2.2. UV-VIS Absorption spectroscopy

At UPMC two instruments for measurement of absorption spectra were employed: Cary 3E UV-visible spectrophotometer and UVIKON 923 spectrophotometer (Bio-Tek Kontron Instruments). At Charles University, a spectrophotometer Lambda 12 (Perkin-Elmer) was used. The samples were measured in 1 cm^2 quartz cells.

In the case of combined fluorescence-absorption experiment, absorption spectra were recorded immediately after acquisition of the fluorescence. Otherwise the sample was placed in a temperature stabilized cell-holder and tempered for about 10min. before the measurement. Acquired absorption spectra were corrected for a background threshold and for the sample dilution if necessary.

3.2.3. Raman spectroscopy

Most of the Raman spectra were recorded at Charles University in Prague on a home-made Raman spectrometer in a standard 90° geometry on a multichannel spectrograph Spex 270 M (Jobin Yvon). To excite Raman scattering a $532.15 \text{ nm} / 200 \text{ mW}$ Nd-YAG Verdi V2 laser (Coherent) was used. Data were recorded on a CCD detector (Princeton Instruments) with 1340×100 pixel array cooled by liquid nitrogen. Holographic diffraction grating was used with groove

density of 1800 lines / mm. Elastically scattered light was eliminated by an edge filter. Data were acquired in the spectral range from 600 to 1800 cm^{-1} . The scheme of the setup is depicted on Figure 18.

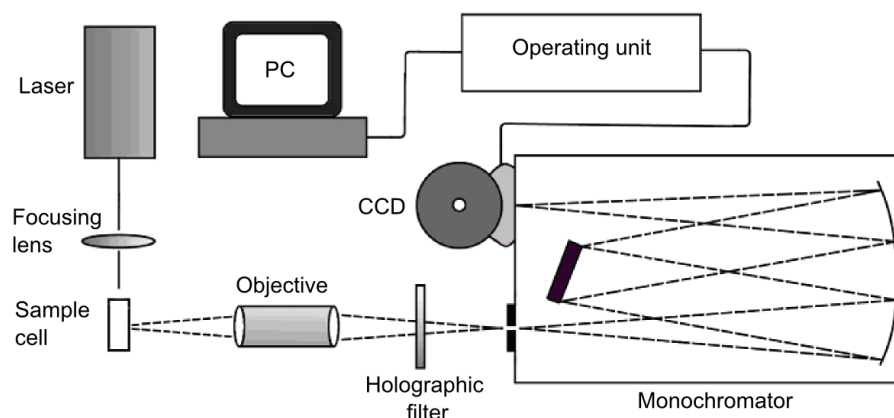


Figure 18. Basic scheme of the Raman scattering apparatus

Samples were placed in a temperature stabilized microcell of 20 μl internal volume (see Figure 19).

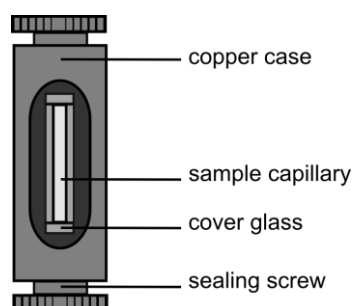


Figure 19. Raman microcell scheme. The microcell is designed for measurements of small amount of sample (12-20 μL according to the sample capillary). Laser beam passes the cell longitudinally through the sample capillary and holes in the sealing screws. Scattered radiation is collected perpendicularly from the central part of the sample capillary. The cell is placed inside a thermostated holder.

Complementary measurements were performed at University of Pierre and Marie Curie in Paris on a Jobin-Yvon T64000 Raman spectrometer in a standard 90° geometry. Samples were placed in a temperature stabilized 3 ml cell with a 20 μl groove for micro-volume measurements, and excited by the 488 nm / 100 mW Ar^+ laser SP Stabilite 2017.

For all experiments the samples were diluted so that their concentration was 7 - 9 mM using either one of the buffers mentioned above or a 0.01 M HCl or KOH solution (to avoid a loss of reliability in some spectral regions caused by the buffer

Raman signal). Samples were placed in a cell and tempered for about 20 minutes before the measurement. The total acquisition time was 20 min. for each measurement.

Every spectrum was calibrated independently by using a spectrum of neon discharge lamp measured immediately afterward. Calibration program NeoKalSPex and Labkal5 was used for spectra measured in Prague and in Paris, respectively. Both programs were developed at Charles University in Prague by assoc. prof. Jiří Bok. Unwanted signal of solvent and impurities from the synthesis of the biomolecules (see Figure 20) was removed with help of a singular value decomposition-based method [82].

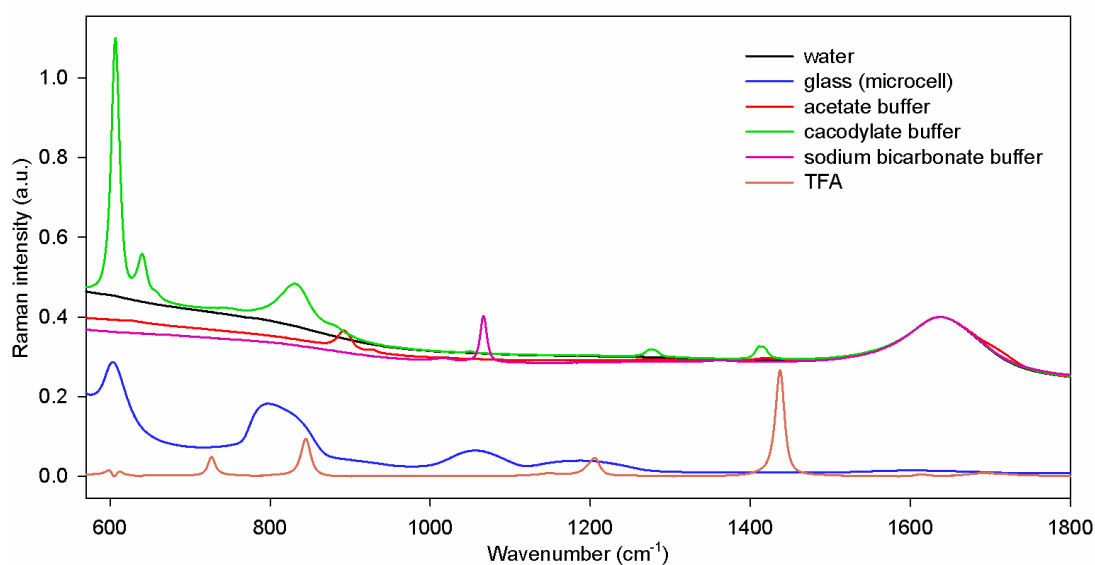


Figure 20. Unwanted signal in Raman spectra. Spectra of used dissolving agents, artefact signal of the microcell glass and possible impurity from the synthesis of oligopeptides (TFA).

3.2.4. Infrared spectroscopy

Infrared spectra were recorded on a Bruker Vector 33 Fourier-transform infrared (FTIR) spectrometer at Charles University in Prague. Spectrophotometer was equipped with a standard MIR global source, a KBr beamsplitter and an MCT detector. 4000 scans were collected with a 2 cm^{-1} spectral resolution and a Blackman-Harris 3-term apodization function. Aqueous 3 mM peptide solutions were measured at room temperature in CaF_2 -cell with an $8\ \mu\text{m}$ path length. Spectral contribution of water was corrected following the standard algorithm [83]. Spectrum

of water vapours was subtracted and finally the spectra were intensity normalized at amide I band.

3.2.5. Circular dichroism

Circular dichroism (CD) spectra of shorter oligopeptides (CH08 and JS01) were recorded on Jasco J-815 spectropolarimeter at Institute of Organic Chemistry and Biochemistry AS CR. The spectra were collected from 180 to 260 nm at room temperature in 0.1 cm quartz cells (peptide concentration 5 mM, 2 scans, 0.5 nm steps, 20 nm/min speed, 8 s time constant, 1 nm spectral bandwidth) and from 230 to 380 nm in 1 cm quartz cells (peptide concentration 23 mM and identical other experimental parameters). After baseline subtraction, final data were expressed as molar ellipticities θ ($\text{deg}\cdot\text{cm}^2\cdot\text{dmol}^{-1}$) per residue.

3.2.6. pH measurement

pH meter IQ170G (IQ Scientific Instruments) equipped with a stainless steel pH probe was used to verify the pH of all buffers and samples during the pH sensitive measurements at UPMC. At Charles University, pH meter Orion PerpHect LogRmeter 350 (Thermo) equipped with a glass electrode was employed.

3.3. Data analysis

3.3.1. Factor analysis

Factor analysis (FA) belongs to multidimensional statistical methods enabling reduction of a set of experimental data without any loss of information. The general task of FA is to reduce the set of random variables Y_1, \dots, Y_N to smaller data set, which represents their best substitution. This task has several solutions. The fundament of the simplest one lies in a consecutive retrieval of random variables, called factors, which were linear combinations of the original variables and gradually reached the greatest part of their variability [84].

We used a Singular Value Decomposition (SVD), one of FA algorithms. The set of N measured spectra $Y_i(\lambda_k)$, where λ_k represents individual spectral points ($k = 1, 2, \dots, K$) and i is the index of the spectrum in the set ($i = 1, 2, \dots, N$), is decomposed into a basis of orthonormal spectral profiles (subspectra) $S_j(\lambda_k)$ ($j = 1, 2, \dots, N$). We obtain singular numbers W_j representing the statistical weights of individual subspectrum and a unitary matrix of normalized coefficients V_{ij} (scores) giving relative portion of j -th subspectrum $S_j(\lambda_k)$ in the i -th measured spectrum $Y_i(\lambda_k)$:

$$Y_i(\lambda) = \sum_{j=1}^N W_j V_{ij} S_j(\lambda_k) \quad (3.2)$$

Both V_{ij} and $S_j(\lambda_k)$ comply with relations of orthonormality:

$$\sum_{k=1}^K S_j(\lambda_k) S_m(\lambda_k) = 0 \text{ for } j \neq m, \quad \sum_{k=1}^K S_j(\lambda_k) S_j(\lambda_k) = 1 \quad (3.3)$$

$$\sum_{i=1}^N V_{ij} V_{im} = 0 \text{ for } j \neq m, \quad \sum_{i=1}^N V_{ji} V_{mi} = 0 \text{ for } j \neq m \quad (3.4)$$

$$\sum_{i=1}^N V_{ij} V_{ij} = 1 \quad (3.5)$$

Singular numbers are ordered in a descending succession:

$$W_k \leq W_l \quad \text{for} \quad k > l \quad (3.6)$$

Each of the terms of the sum in equation (3.2) represents an independent piece of information, which is contained within the spectral dataset. Weight of this information is represented by the corresponding singular number W_j . Therefore SVD enables to extract the main informational content from a series of spectra. The sum on the right side of the equation (3.2) can be limited only to first M terms ($M < N$), thus the best possible approximation of the original spectral set will be obtained using M number of subspectra. Very often the subspectra of higher number contain

only a noise. Therefore omitting these components, a better signal to noise ratio is gained and also a number of data is reduced without any loss of information.

$$Y_i(\lambda_k) \approx \sum_{j=1}^M W_j V_{ij} S_j(\lambda_k) \quad (3.7)$$

The smallest M value, for which both sides of equation (3.7) differ only by an experimental error, represents a meaningful number of subspectra. It is called “factor dimension”. Factor dimension of analysed data should correspond to a number of independent components and can be estimated from the decrease in progression of singular values, or the noise increase in the subspectra succession. Another appropriate criterion is a progress on m of the residual error:

$$\sigma_R = \sqrt{\frac{\sum_{j=m+1}^N W_j^2}{K(N-m)}} \quad (3.8)$$

In the region above the suitable M a weak, almost linear decrease of residual error is usually observed [85].

3.3.2. Fluorescence quenching analysis

FA enables generally distinguishing among individual spectral components in the series of spectra dependent on a certain property. In particular case of fluorescence quenching this concerns the decrease of the fluorescence intensity caused by the addition of quencher.

For a simple photophysical intermolecular deactivation process, the Stern-Volmer relationship holds:

$$\frac{F_0(\lambda_k)}{F(\lambda_k)} = 1 + K_{SV} C^Q \quad (3.9)$$

where F_0 and F are the fluorescence intensities in the absence and presence, respectively, of quencher. C^Q is the quencher concentration and K_{SV} is the Stern-Volmer quenching constant. Quenching data are usually presented as Stern-Volmer plot of F_0/F versus C^Q that should yield a straight line with a slope equal to K_{SV} , which can be expressed as

$$K_{SV} = k_q \tau_0, \quad (3.10)$$

where k_q is the bimolecular quenching rate constant (proportional to the sum of diffusion coefficients for fluorophore and quencher) and τ_0 is the excited state lifetime in the absence of quencher [81].

In our study, quenching measurements of both shorter and longer oligopeptides by various quenchers of different charges were performed. Corrected data (according to the procedure mentioned in chapter 3.2.1) were treated by factor analysis (SVD). The SVD results revealed factor dimension of two for oligopeptides containing several tyrosines. We have thus generalized the Stern-Volmer model for two independently quenched spectral components $F^I(\lambda)$ and $F^{II}(\lambda)$ composing the measured spectrum:

$$Y_i(\lambda) = \frac{F_0^I(\lambda)}{1+K_{SV}^I C_i^Q} + \frac{F_0^{II}(\lambda)}{1+K_{SV}^{II} C_i^Q} , \quad (3.11)$$

where $F_0^I(\lambda)$ and $F_0^{II}(\lambda)$ are the two fluorescence components without quencher, C_i^Q is the concentration of the quencher, and K_{SV}^I , K_{SV}^{II} are the corresponding Stern-Volmer constants. $F_0^I(\lambda)$ and $F_0^{II}(\lambda)$ can be approximated as linear combinations of the first and the second subspectrum:

$$F_0^I(\lambda) = \sum_{j=1}^2 r_j^I S_j(\lambda), \quad F_0^{II}(\lambda) = \sum_{j=1}^2 r_j^{II} S_j(\lambda) , \quad (3.12)$$

where r_j^I and r_j^{II} are coefficients of linear combination. Considering equation (3.7) for $Y_i(\lambda)$ and orthogonality of subspectra equation (3.3) a final set of $2 \times N$ equations is obtained:

$$W_j V_{ij} = \frac{r_j^I}{1+K_{SV}^I C_i^Q} + \frac{r_j^{II}}{1+K_{SV}^{II} C_i^Q}; \quad i = 1, 2, \dots, N; \quad j = 1, 2 \quad (3.13)$$

The six unknown parameters ($K_{SV}^I, K_{SV}^{II}, r_j^I, r_j^{II}, j = 1, 2$) can be determined as a simultaneous non-linear least-square fit of the right sides to the left ones.

3.3.3. pH titration analysis

pH titration was performed on shorter oligopeptides (CH08 and JS01) and on the MADS box. Corrected fluorescence and absorption data were processed by FA and fitted in order to determine the pK_a constants of titratable amino acids.

The derivation of pH as a measure of acidity in a system is described by Henderson-Hasselbalch equation:

$$pH = pK_a + \log_{10} \left(\frac{C_{A^-}}{C_{HA}} \right) . \quad (3.14)$$

Here C_{HA} is the molar concentration of the undissociated weak acid and C_{A^-} is the molar concentration of the acid's conjugate base in the non-specific Brønsted acid-base reaction:



In our experiments an increase of pH causes gradual deprotonation of titratable amino acids (Asp, Glu, His, Cys, Tyr, Lys, Arg) within the oligopeptide. Using fluorescence and absorption spectroscopy only the changes influencing photosensitive residues can be observed and examined. Our approach for the determination of pK_a constant of oligopeptide intrinsic fluorophores and spectral components referring to differently charged states was already published in [I]. In this article the methodology was applied on oligopeptides with only one tyrosine, hence resolving the simplest case of a peptide undergoing only one spectrally sensitive pH transition.

The following theoretical relations represent extension to the most complex case of three distinct constants, with whom we met in the case of MADS box measurement. In this case, four different states of the oligopeptide (A, B, C, D) are considered:



Four spectral components are then resolved in the pH titration spectra, therefore:

$$Y_i(\lambda) = C_i^A F^A(\lambda) + C_i^B F^B(\lambda) + C_i^C F^C(\lambda) + C_i^D F^D(\lambda) \quad (3.17)$$

where $F^A(\lambda)$, $F^B(\lambda)$, $F^C(\lambda)$ and $F^D(\lambda)$ are the spectra of individual components corresponding to its unit concentration. They form the original spectrum $Y_i(\lambda)$ proportionally to their current portions C_i^A , C_i^B , C_i^C and C_i^D ,

$$C_i^A + C_i^B + C_i^C + C_i^D = 1 \quad (3.18)$$

Following equation (3.14) they depend on pH as:

$$\begin{aligned} C_i^A &= \frac{1}{1 + 10^{pH-pK_a^1} + 10^{2pH-pK_a^1-pK_a^2} + 10^{3pH-pK_a^1-pK_a^2-pK_a^3}} \\ C_i^B &= C_i^A 10^{pH-pK_a^1} \\ C_i^C &= C_i^B 10^{pH-pK_a^2} \\ C_i^D &= C_i^C 10^{pH-pK_a^3} \end{aligned} \quad (3.19)$$

On the other hand, the four spectral components can be approximated as linear combinations of FA subspectra:

$$\begin{aligned}
 F^A &= \sum_{j=1}^M r_j^A S_j(\lambda) \\
 F^B &= \sum_{j=1}^M r_j^B S_j(\lambda) \\
 F^C &= \sum_{j=1}^M r_j^C S_j(\lambda) \\
 F^D &= \sum_{j=1}^M r_j^D S_j(\lambda)
 \end{aligned} \tag{3.20}$$

where r_j represent the coefficients of linear combination. Due to the orthogonality of spectral profiles a final set of $M \times N$ equations is obtained:

$$W_j V_{ij} = r_j^A C_j^A + r_j^B C_j^B + r_j^C C_j^C + r_j^D C_j^D; \quad i = 1, 2, \dots, N; \quad j = 1, 2, \dots, M \tag{3.21}$$

In a simultaneous fit of fluorescence and absorbance data, which we also performed, two sets of spectral components (of absorbance and of fluorescence emission) were obtained by fitting two sets of equations (3.21) with help of relations (3.19) using the same triad of pK_a constants.

4. Results and discussion

4.1. Free tyrosine

4.1.1. Concentration dependence of free tyrosine

To correct the inner filter effect (IFE) due to a high optical density, equation (3.1) was mostly employed [81]. This formula is though well applicable only when the absorbance of the examining sample is less than 0.2. As in some cases, in particular those concerning the study of MADS interaction with oligonucleotides the absorbance exceeded 0.2 at the excitation wavelength of 275 nm, a calibration curve for precise correction of the attenuation due to absorption of exciting radiation (primary IFE) was determined.

Tyrosine solution was gradually diluted (from 0.64 to 0.03 mM). After each dilution, fluorescence and absorption spectra were recorded. Measured spectra were treated as described in chapters 3.2.1 and 3.2.2. Factor analysis (SVD) applied to fluorescence emission spectra (see Figure 21) showed that the factor dimension is equal to 1, which confirmed a negligible concentration effect on the shape of the fluorescence spectrum. The dependence of V_1 on the Tyr concentration was fitted by equation derived from equation (3.1.) so that a primary IFE effect was corrected according to:

$$f_{ex} = -5.30 + 1.44 \times 10^{\frac{(1.28+0.24 \cdot OD_{ex})}{2}},$$

where f_{ex} is the factor correcting the absorption of incident light

Since the absorption is below 0.2 in the whole emission region (and the same is expected when oligonucleotides are present in the sample), a recalibration of the fluorescence reabsorption (secondary IFE) is not necessary and can be corrected as in equation (3.1) [81]:

$$f_{em} = 10^{\frac{(OD_{em})}{2}}$$

The IFE corrected fluorescence intensity is then given by:

$$\frac{F_{corr}}{F_{obs}} = f_{ex} \cdot f_{em}$$

Figure 22 shows that observed fluorescence intensities are proportional to the absorbance over only a limited range ($A < 0.05$ [81]). For higher absorption values additional correction is indispensable.

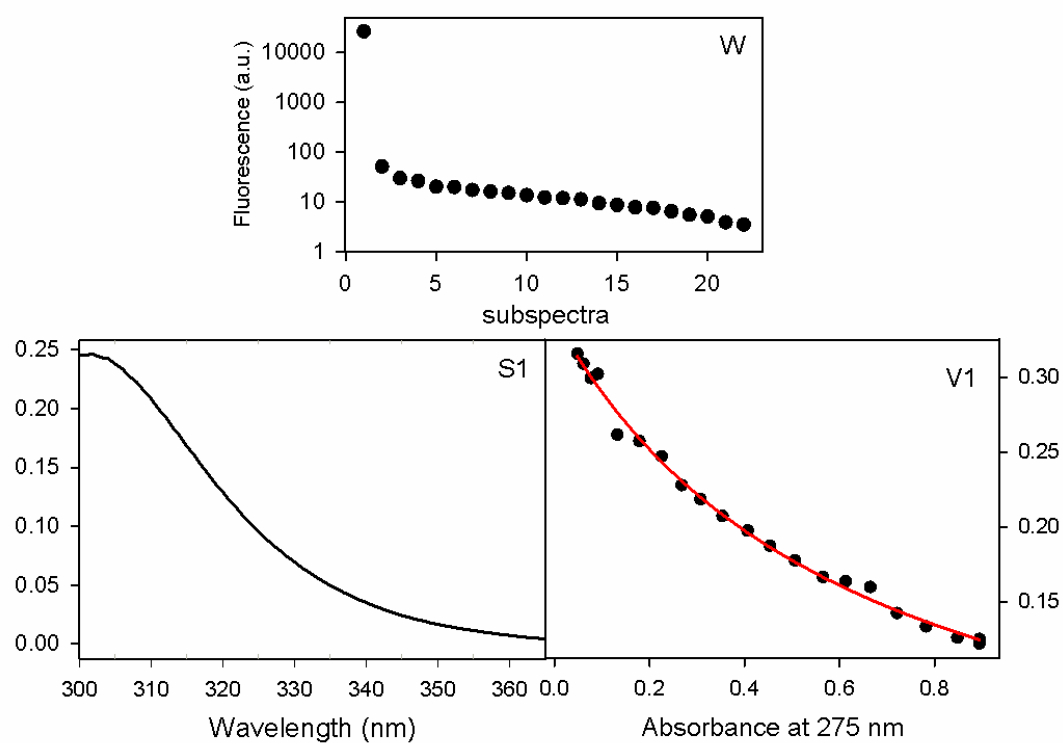


Figure 21. SVD results of the tyrosine fluorescence in dependence on its concentration. (To completely avoid possible contributions from elastic scattering of the excitation, only spectral region 300-370 nm was analysed.) Red line in the graph of V1 corresponds to the fit.

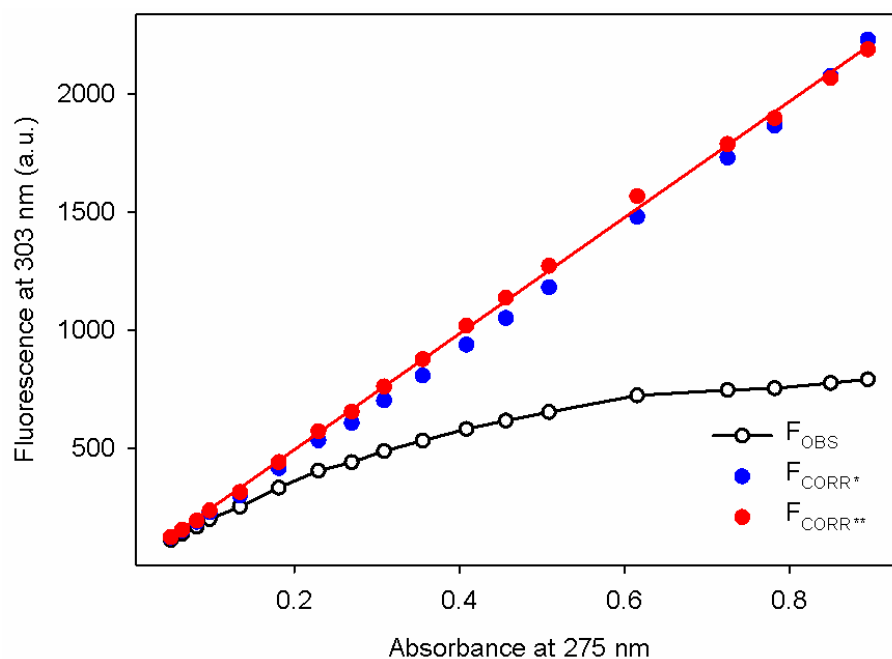


Figure 22. The effect of optical density on the fluorescence intensity of tyrosine and its correction. Black line shows the measured fluorescence intensities. Blue and red circles indicate corrected intensities according to equation (3.1) (*) and to our fit (**). Red curve is a linear regression of (**) corrected intensities. ($OD_{em} = 0$ in both cases).

It can be seen from Figure 22 that application of our formula improves the IFE correction in respect to equation (3.1). This is demonstrated by the coefficient of determination for linear regressions of corrected intensities:

$R_{sqr} = 0.9975$ for IFE according to the equation (3.1),

$R_{sqr} = 0.9993$ for IFE* based on our approach.

4.2. Shorter segments of the MADS box

The N terminal part containing prevalingly basic amino acids of the SRF MADS box is responsible for the DNA binding. To characterize it in a closer detail, model oligomers corresponding its three selected segments (see Figure 23) were investigated. CH08 and JS01 appear in the αI helix, whereas JS02 in the N-extension of the SRF MADS box [26]. Structure and physico-chemical properties of the short oligopeptides in aqueous solution were characterized by fluorescence, Raman, UV and IR absorption, and CD spectra and their dependence on temperature and pH.

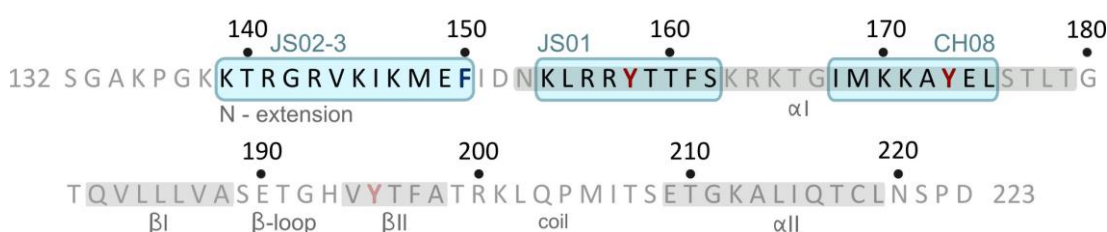


Figure 23. Short model oligopeptides within the sequence of human SRF. Denoted is the secondary structure in single crystal of SRF dimer with target DNA element according to X-ray [26].

4.2.1. Fluorescence and absorption pH dependence of CH08 oligopeptide

Sensitivity of the CH08 segment to pH changes was studied by fluorescence and absorption spectroscopies. Absorption spectra (measured and treated as described in chapter 3.2.2) were almost constant in the pH range 3 - 8. Noticeable changes were observed by further pH increase: the absorption band peaking at 275 nm moved to a longer wavelengths and increased its high - band maximum at 294 nm and 1.5-fold increase of intensity for pH 11 (see Figure 24). Results of factor analysis applied on absorption spectra are shown in Figure 25. The factor dimension is 2, indicating a single acido-basic transition. The first subspectrum S_1 represents certain average of measured spectra - the 1st coefficients V_{i1} thus describe the overall increase of absorbance as a function of pH. The second subspectrum S_2 , with comparable weight as the first one, accounts for the main changes of the spectral shape. The fit according a model of single acido-basic transition between two CH08 forms (see chapter 3.3.3) matched perfectly the pH dependences of V_1 and V_2 values and provided the value of pK_a constant:

$$pK_a = 9.45 \pm 0.05$$

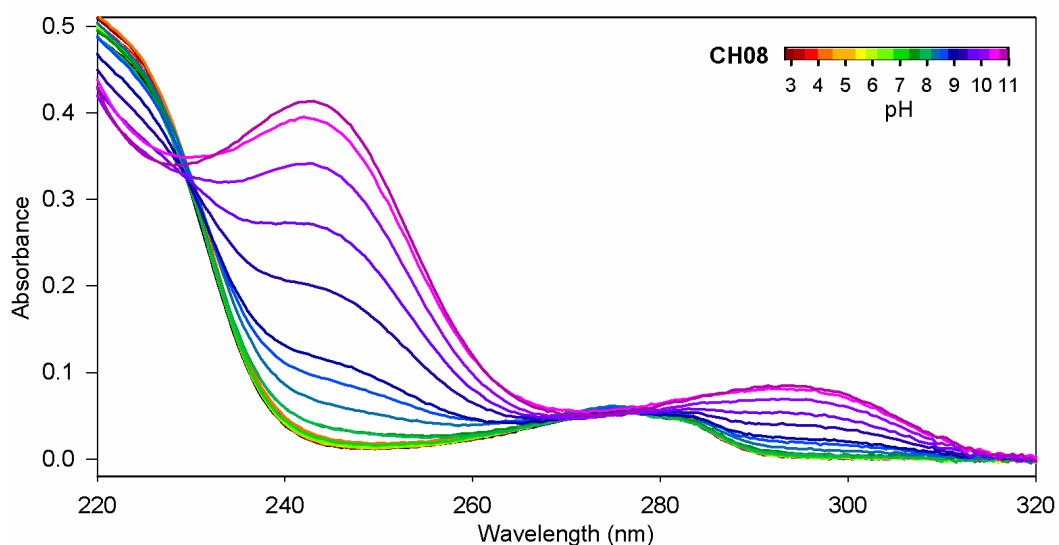


Figure 24. pH dependence of CH08 oligopeptide absorption spectra. From acidic (red) to basic (violet) pH.

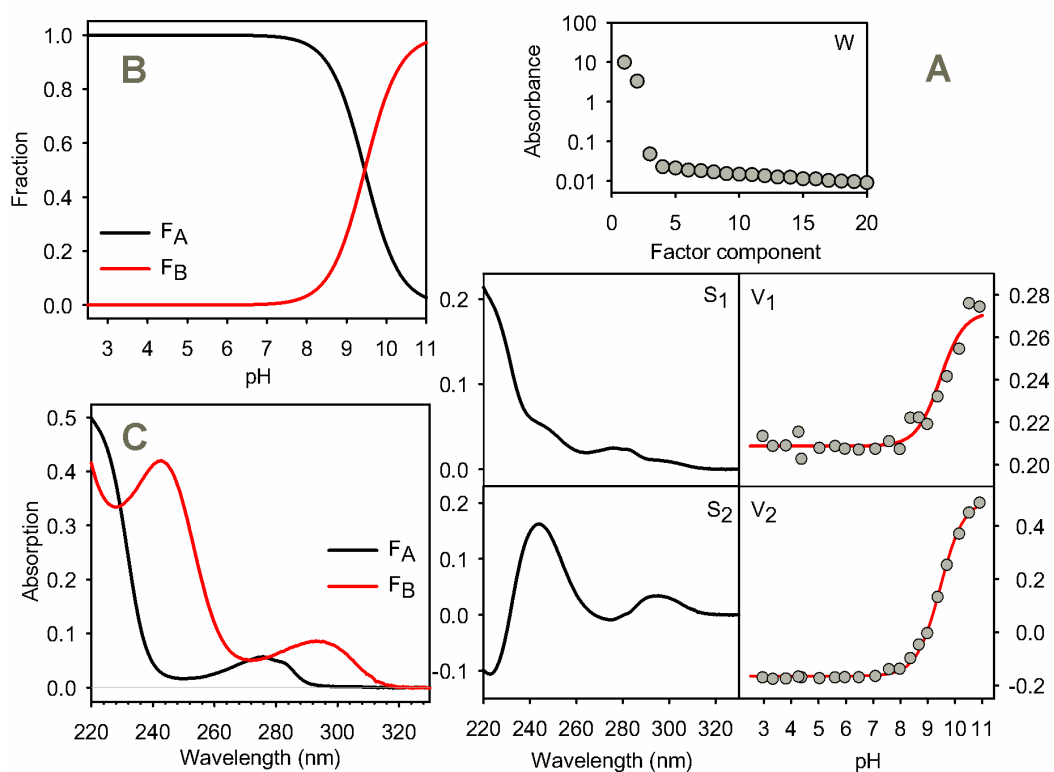


Figure 25. Factor analysis (SVD) of pH dependency of CH08 absorption and its fit according to chapter 3.3.3. (A) SVD characteristics. Red lines show the results of the fit. (B) Determined pH dependences of the two CH08 forms. (C) Isolated absorption spectra of both forms.

In the fluorescence emission spectra of CH08, a characteristic peak at 303 nm typical for tyrosine is observed. With an increase of pH above 8, the emission significantly decreases (see Figure 26). It obviously corresponds to the deprotonation of tyrosine to tyrosinate that is known to reduce substantially the quantum yield of fluorescence. Results of factor analysis applied on fluorescence spectra of the oligopeptide are shown in Figure 27. The factor dimension is 2 as for absorption spectra. The first coefficients V_1 describe the dominant pH effect, i.e. the decrease of the overall spectral intensity. The second subspectrum S_2 accounting for the main changes of the spectral shape is about 100 times less significant than the first one. This correlates with the very weak fluorescence of tyrosinate. The fit to a model considering a single acido-basic transition between two forms analogous to that used for absorption data, provided fluorescence spectra of the two forms (see Figure 27) and a value pKa constant

$$pK_a = 9.43 \pm 0.06$$

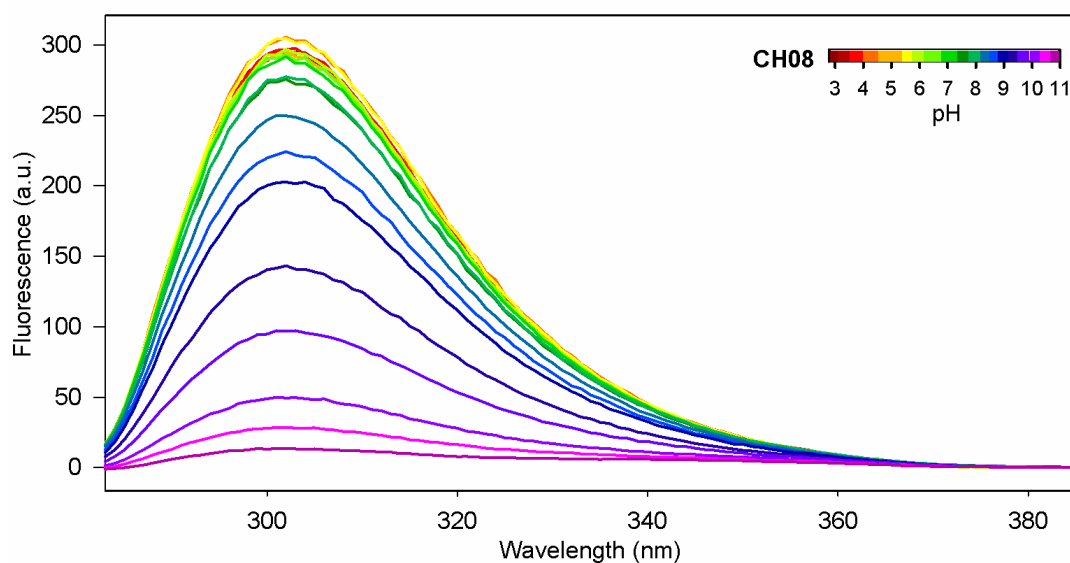


Figure 26. pH dependence of CH08 oligopeptide fluorescence spectra.

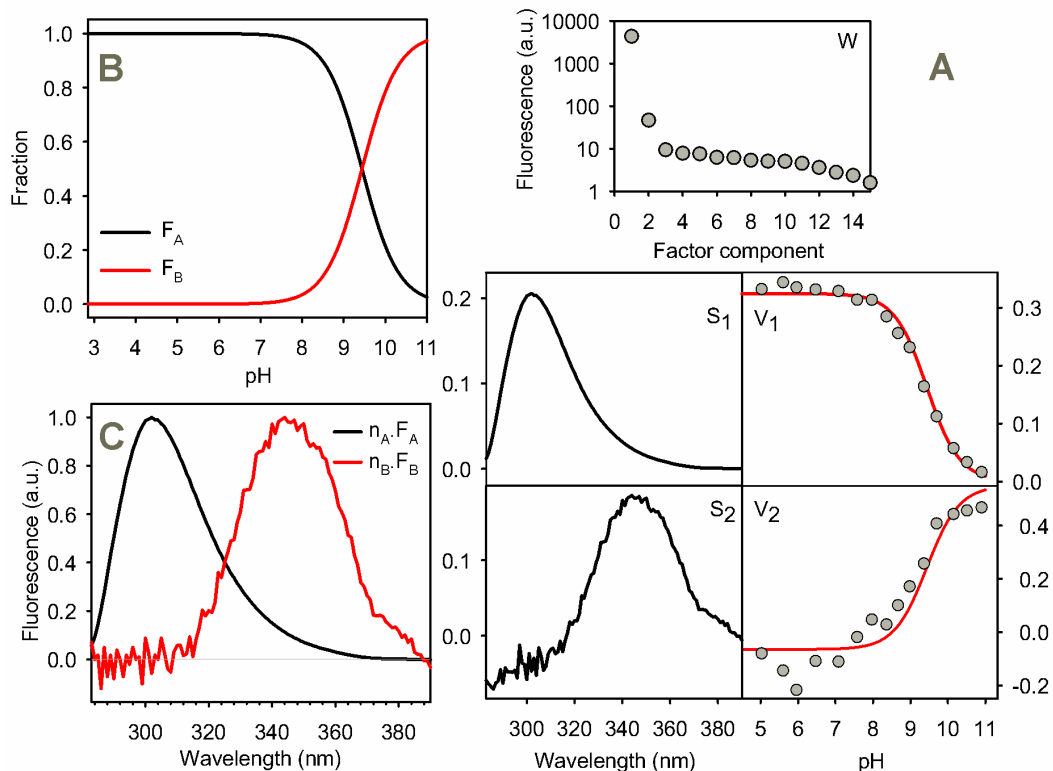


Figure 27. Factor analysis (SVD) of pH dependency of CH08 fluorescence and its fit according to chapter 3.3.3. (A) SVD characteristics. Red lines show the results of the fit. (B) Determined pH dependences of the two CH08 forms. (C) Isolated emission spectra of both forms, normalized by using coefficients $n_A = 0.003$, $n_B = 0.201$.

Perfect agreement of pKa constants obtained independently from absorption and fluorescence experiment verify the reliability of the obtained value. This value is though significantly lower than 10.07 corresponding to free tyrosine [3]. Our explanation is that this shift of pKa is caused by the positively charged environment of tyrosine in CH08 thanks to two positively charged lysines [86], only partly compensated by negatively charged glutamic acid. Results of this experiment were published in [I].

4.2.2. Fluorescence quenching of the CH08

Quenching of CH08 by DCA was performed in 25mM acetate and 25mM cacodylate buffer at pH 3.2 and 7.0, respectively, to disclose whether there is any difference in the structure of the oligopeptide changing the accessibility of the non-ionic quencher to the tyrosine. Sets of obtained fluorescence spectra were treated as described in the chapter 3.2.1. Stern-Volmer constants in both buffers were first

determined using equation (3.9), for the wavelengths of 297, 303 and 325 nm corresponding to the maximum and two shoulders of the MADS box fluorescence emission. The Stern-Volmer plots shown on Figure 28, provided values of Stern-Volmer constant for pH 3.2

$$K_{SV}^{297} = 10.1 \pm 0.1 M^{-1}, \quad K_{SV}^{304} = 10.0 \pm 0.1 M^{-1}, \quad K_{SV}^{325} = 9.9 \pm 0.2 M^{-1}$$

and for pH 7.0

$$K_{SV}^{297} = 10.7 \pm 0.3 M^{-1}, \quad K_{SV}^{304} = 10.5 \pm 0.3 M^{-1}, \quad K_{SV}^{325} = 10.7 \pm 0.4 M^{-1}$$

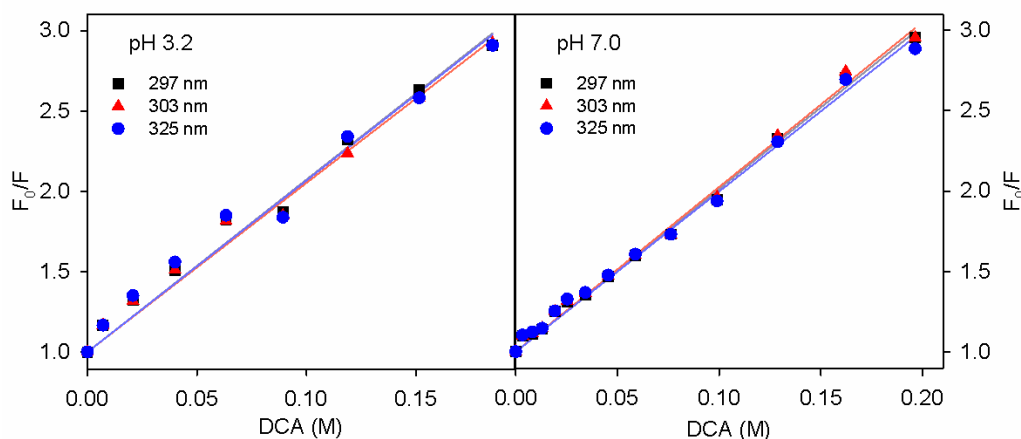


Figure 28. Stern-Volmer plots of CH08 fluorescence quenching by DCA. Left: CH08 in 25mM acetate buffer, pH 3.2. Right: CH08 in 25mM cacodylate buffer, pH 7.0.

To investigate the possible existence of weak effects going beyond the standard Stern-Volmer theory, we also treated the sets of fluorescence spectra by joint FA (see Figure 29 for the result). The factor dimension equals to one as can be seen from progress of singular values W . This means that there is no detectable difference of the fluorescence spectrum caused either by the changed pH or by addition of the quencher. The fit applied (according to the method introduced in chapter 3.3.2) to the dependence of the coefficients V_I on the quencher concentration matched the experimental data perfectly, which verified pure Stern-Volmer quenching process. The Stern-Volmer constants obtained by the fit

$K_{SV} = 10.0 \pm 0.3 M^{-1}$ for pH 3.2 and $K_{SV} = 10.3 \pm 0.3 M^{-1}$ for pH 7.0 are in a perfect agreement with those obtained from the Stern-Volmer plots.

As a result, no significant difference in Stern-Volmer constants was observed for neutral and acidic CH08 solution, indicating the same diffusion processes controlling the quenching.

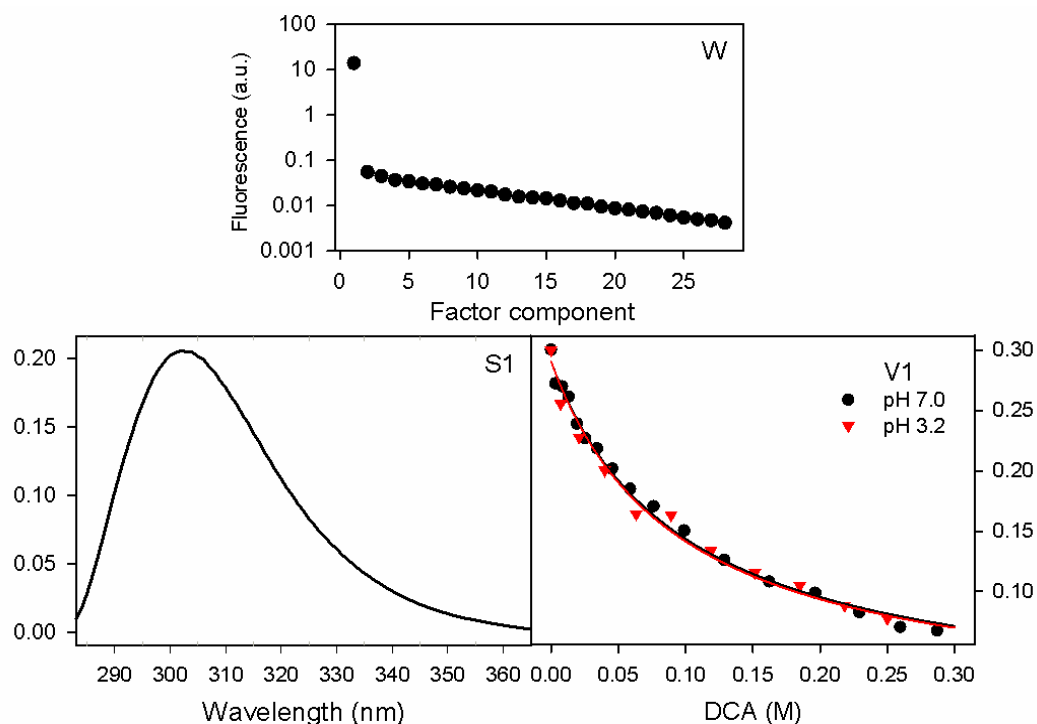


Figure 29. SVD results of CH08 fluorescence quenching by DCA. Black and red lines in the graph of V1 correspond to the fit applied to the values corresponding to neutral and acidic pH, respectively.

4.2.3. CD spectra of CH08 oligopeptide

CD spectra of the CH08 were measured for three pH (acetate buffer - pH 3.2; water - pH 5.0; sodium bicarbonate buffer - pH 11.0). The most intensive CD signal was obtained in the spectral region 190–240 nm where are bands attributed to π - π^* and n - π^* transitions localized at the peptide backbone. A negative band at 196 nm was observed at all measured pH. In acidic and neutral pH it was accompanied by a negative shoulder around 230 nm whereas in the basic pH this shoulder shifted to 225 nm and its intensity increased (see Figure 30). These CD characteristics indicate unordered secondary structure as a main structural motif [87-88]. However, electronic CD is essentially sensitive to long range interactions. Therefore a study by vibrational spectroscopies (Raman and FTIR) which are more sensitive to structural details and local arrangements was necessary for deeper understanding of the structure (see following chapters 4.2.4 and 4.2.5).

As CH08 contains tyrosine residue, one can expect up to four additional π - π^* transitions due to the phenolic chromophore of tyrosine side chain. Although they are partially hidden by a signal of n - π^* transitions of the peptide backbone we

can assume that in CH08 oligopeptide π - π^* B₀ transitions significantly contribute to the weak spectral band observed at ~225 nm.

The distinct contribution of aromatic side chains appeared in the spectral region of 240-320 nm. Weak positive spectral band around 276 nm was observed for acidic and neutral environment. At basic pH a red shift to 294 nm and intensity increase (without change of the sign) occurred. This corresponds to the appearance of tyrosinate form according to published data [89].

Results of this experiment were published in [II].

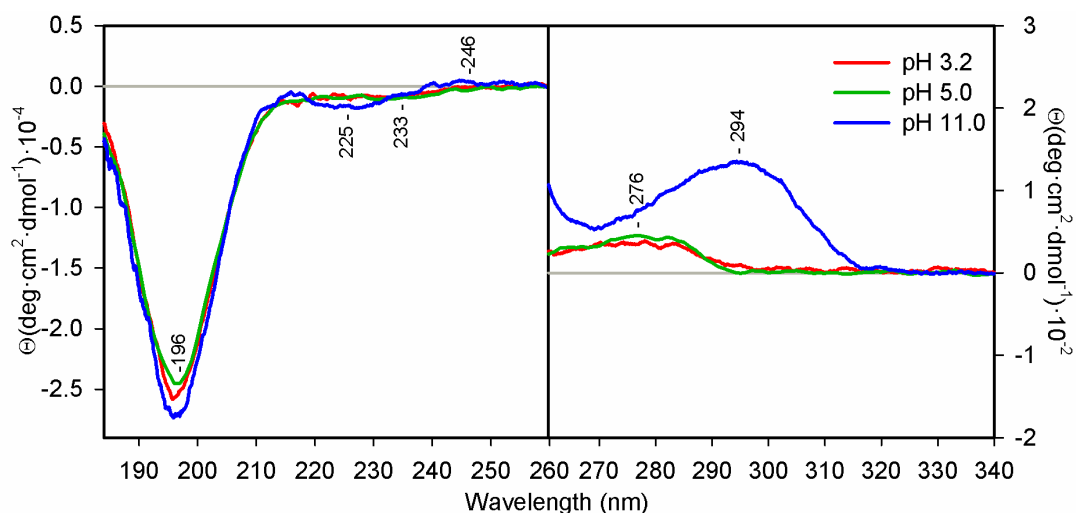


Figure 30. Electronic circular dichroism spectra of CH08 oligopeptide in acetate buffer (red), in water (green) and in a sodium bicarbonate buffer (blue).

4.2.4. Raman spectra of CH08 oligopeptide

Raman spectra of CH08 (Figure 31) were measured at pH 3.2, 5.0 and 12.0 and treated according to chapter 3.2.3. Negligible difference between Raman spectra in acidic and neutral pH indicated that deprotonation of glutamic acid ($pK_A^{Glu} = 4.25$) [3] did not have any effect neither on the secondary structure of the oligomer nor on the polarizability of Glu residue. Further increase of pH resulted in significant changes of several Raman bands. These changes could be divided into two groups, the first corresponding to tyrosine deprotonation and the second to the changes in the secondary structure. No direct spectroscopic markers of deprotonation of the pair of Lys residues ($pK_A^{Lys} = 10.53$) [3] were observed.

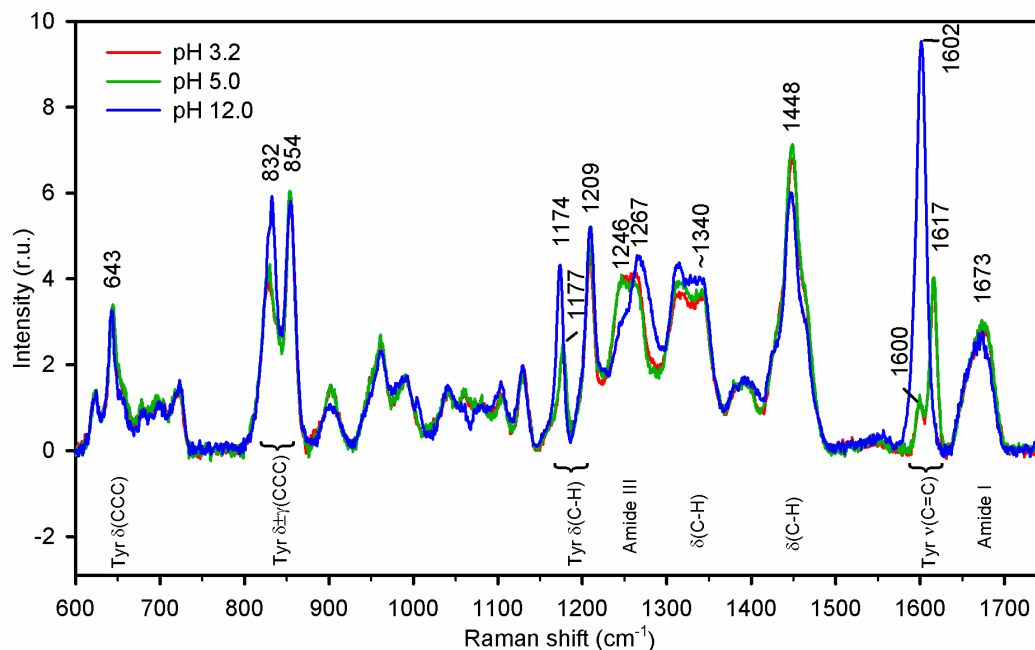


Figure 31. Raman spectra of CH08 measured at acidic (red), neutral (green), and basic pH (blue). The most distinctive bands are assigned according to the literature [71-72, 97].

The loss of a hydrogen at Tyr phenol group leads to a shift and intensity change of several peaks. The difference between the neutral and negatively charged form of Tyr is primarily prominent on the in-plane stretching vibrations $\nu(\text{C}=\text{C})$ of the ring. At neutral pH, the pair of bands at 1617 and 1600 cm^{-1} (ν_{8a} and ν_{8b} respectively, see Table 4 for the detailed band assignment) was observed while at basic pH only one, but very strong band at 1602 cm^{-1} was visible. Ring deformation modes $\delta(\text{C}-\text{H})$ are much less affected by deprotonation. The peak at 1209 cm^{-1} changes neither the position nor the intensity while the band at 1177 cm^{-1} corresponding to ν_{9a} with a contribution from $\text{C}_6\text{H}_5-\text{C}$ stretching increases its intensity and shifts to 1174 cm^{-1} at basic pH. A change in the ratio of the bands at 830 and 854 cm^{-1} assigned to the Fermi resonance between the symmetric ring-breathing deformation $\delta(\text{CCC})$, ν_1 and the overtone of the non-planar ring vibration $\gamma(\text{CCC})$, ν_{16a} (fundamental frequency 413 cm^{-1}) was also observed. At basic pH the lower band shifted to 832 cm^{-1} and increased in intensity. This is in agreement with literature [75] showing that the relative intensity increase of this particular band as compared to the band at 854 cm^{-1} is directly related to the presence of a negative charge (or even partial negative charge) at the oxygen atom. The 643 cm^{-1} band

corresponding to the $\delta(\text{CCC})$ deformation, ν_{6b} appears to be insensitive to the protonation state at all.

Table 4. Frequencies of selected vibrational modes of tyrosine and tyrosinate observed in Raman spectra of CH08 oligopeptide.

Tyrosine			Tyrosinate		
Wilson* nomenclature	Raman shift (cm^{-1})	description	Wilson* nomenclature	Raman shift (cm^{-1})	description
ν_{8a}	1617	$\nu(\text{C}=\text{C})$	ν_{8a}	1602	$\nu(\text{C}=\text{C})$
ν_{8b}	1600	$\nu(\text{C}=\text{C})$	ν_{19b}	1425	$\nu(\text{C}=\text{C})$
ν_{19b}	1448	$\nu(\text{C}=\text{C})$	ν_{14}	1313	$\nu(\text{C}=\text{C})$
ν_3	1341	$\delta(\text{C}-\text{H})$	ν_{9a}	1174	$\delta(\text{C}-\text{H})$
ν_{9a}	1177	$\delta(\text{C}-\text{H})$	ν_{15}	1104	$\delta(\text{C}-\text{H})$
ν_{15}	1129	$\delta(\text{C}-\text{H})$	ν_1	854, 832**	$\delta(\text{CCC})$
ν_{17a}	962	$\gamma(\text{C}-\text{H})$	ν_{17b}	832	$\gamma(\text{C}-\text{H})$
ν_1	854, 830**	$\delta(\text{CCC})$	ν_4	723	$\gamma(\text{CCC})$
ν_{17b}	830	$\gamma(\text{C}-\text{H})$	ν_{6b}	642	$\delta(\text{CCC})$
ν_4	723	$\gamma(\text{CCC})$	ν_{16a}	854, 832**	$\gamma(\text{CCC})$
ν_{6b}	643	$\delta(\text{CCC})$			
ν_{16a}	854, 830**	$\gamma(\text{CCC})$			

* according to the nomenclature of benzene ring modes by Wilson [73, 77], see Figure 14.

** Fermi doublet, the second harmonic of the mode ν_{16a} combined with ν_1

Information about the secondary structure can be derived from the position and shape of the amide I and amide III bands. In acidic and neutral environments, the amide I was located at 1673 cm^{-1} while at basic pH a small downshift to 1671 cm^{-1} was observed. The difference is more obvious in the amide III region consisting of two components. At acidic and neutral pH they are approximately of the same intensity with low and high frequency components at 1246 cm^{-1} and 1262 cm^{-1} , respectively. At basic pH, the relative intensity of the low frequency component decreases while its position remains the same as mentioned above, i.e., 1246 cm^{-1} ; the high frequency component is shifted to 1267 cm^{-1} . This indicates that CH08 adopts a slightly different (average) secondary structure in basic environment than in neutral and acidic one.

Maximum of the amide I at $\sim 1672 \text{ cm}^{-1}$ points on a possible presence of β -sheet, β -turns and β -hairpins along with random coil/unordered structures. The two bands at 1246 and $\sim 1265 \text{ cm}^{-1}$ in the amide III region can be assigned to the same

structures [90-91]. This is in a general agreement with an estimation of the secondary structure from the primary peptide sequence by Garnier-Osguthorpe-Robson method (GOR) [92] and Chou and Fasman [93] algorithms (data not shown). Based on this analysis it may be stated that CH08 tends to form a β -hairpin structure which is in a dynamical equilibrium with an unordered/random coil structure.

At neutral and basic pH, there are also small differences between intensities of the band at 1448 cm^{-1} and the broad band at $\sim 1340\text{ cm}^{-1}$ corresponding to $\delta(\text{C-H})$ deformations (CH_2 and CH_3 bending modes). This could be an effect of both the deprotonation of Lys side chains and the overall influence of the highly basic environment.

The results of this experiment were also published in [II] where the experimentally obtained spectra were compared with the ones calculated by DFT calculations based on the secondary structures obtained from molecular dynamics (MD). The DFT calculations served for more precise and accurate assignment of Raman spectral bands.

4.2.5. Infrared spectra of CH08 oligopeptide

FTIR spectra of CH08 were measured at pH 3.0 and 11.5 (see Figure 32), since at these pH the CH08 tyrosine is fully protonated or deprotonated, respectively. Two major bands, observed at ~ 1649 and $\sim 1543\text{ cm}^{-1}$, are assigned to amide I (arising mainly from $\nu(\text{C=O})$ with minor contributions from out-of-phase $\nu(\text{C-N})$) and amide II (mainly $\delta(\text{N-H})$ and $\nu(\text{C-N})$) vibrations of the backbone chain, respectively [94]. The second derivative, which can resolve overlapping components, reveals the prevalence of either α -helix or unordered structures (these structures are undistinguishable without comparison with measurements in D_2O). Surprisingly, β -sheets are also observable at pH 3.0 owing to the negative band at 1636 cm^{-1} [94]. The second component of β -sheets at 1682 cm^{-1} suggests the presence of antiparallel β -hairpin [94]. Classical Tyr ring vibrations [95] $\nu(\text{C=C})$ are clearly visible at 1618 cm^{-1} , ν_{8a} and 1518 cm^{-1} , ν_{19a} along with a weaker $\nu(\text{C=C})$, ν_{8b} ring vibration [95] at 1599 cm^{-1} . Thus we may conclude that CH08 exists in various geometries;

vibrational spectra contain a mixture of unordered structure and turn characteristics together with that of β -hairpin at pH 3.0.

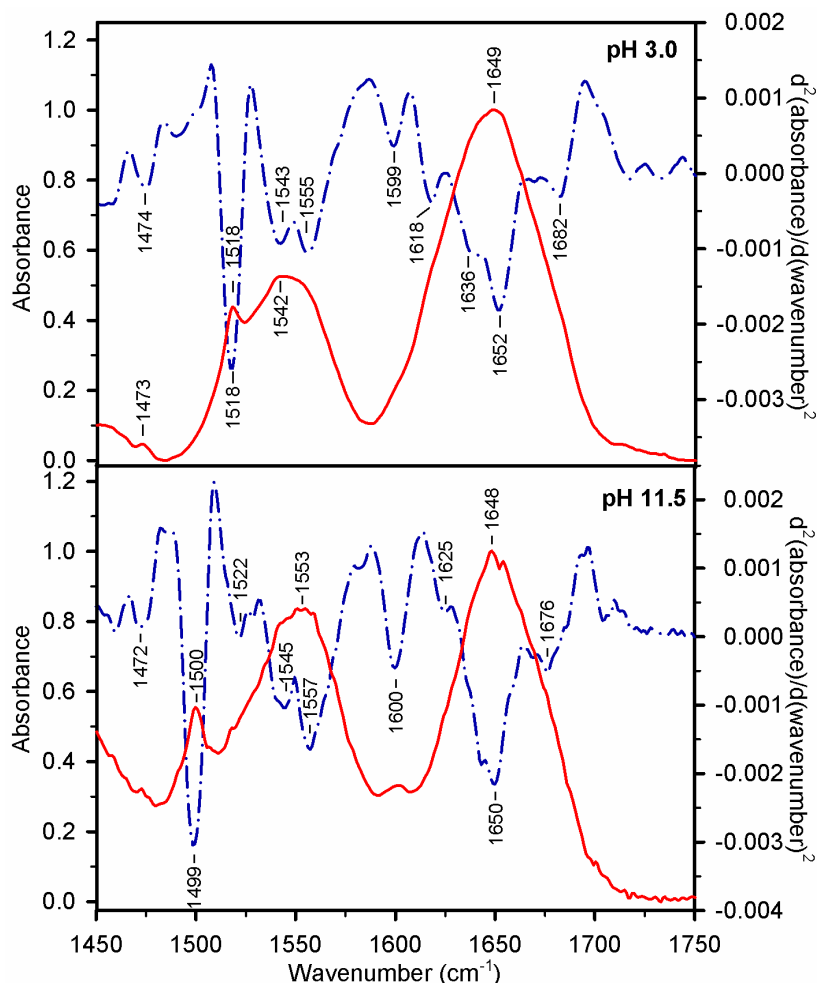


Figure 32. Infrared absorption spectra of CH08 in the region of amide I and amide II bands at various pH. The red solid curves represent the original spectra (normalized) while the blue dash-dot lines are their second derivatives (smoothed by Savitski-Golay function over 21 points).

The most apparent spectral changes at pH 11.5 in respect to pH 3.0 are connected with Tyr deprotonation. The band corresponding to tyrosine ring $\nu(\text{C}=\text{C})$, ν_{19a} vibrations [95] at 1518 cm^{-1} is downshifted by 19 cm^{-1} at 1499 cm^{-1} . The tyrosinate is more polar than the neutral tyrosine and thus the intensity of several other bands increases, e.g., $\nu(\text{C}=\text{C})$ ring vibrations at 1600 cm^{-1} , ν_{8a} and 1522 cm^{-1} , ν_{8b} . Moreover, it seems that the β -hairpin structure nearly disappears at pH 11.5 and disordered structure (at 1650 cm^{-1}) with turns (at 1676 cm^{-1}) prevails [94]. It indicates that negative charges prevent the formation of any stable compact secondary structure. The results of this experiment were also published in [III].

4.2.6. Fluorescence and absorption pH dependence of JS01 oligopeptide

Sensitivity of JS01 segment of the MADS box to pH was studied by using the same procedures of absorption and fluorescence measurements and data treatment as in the case of CH08 (see chapter 4.2.1). JS01 contains as well as CH08 only one photosensitive amino acid – tyrosine. Therefore, very similar spectral sets were obtained (data not shown). SVD analysis provided factor dimension of 2; the pK_a value determined by a fit of absorption data was

$$pK_a = 9.01 \pm 0.05$$

and that obtained from fluorescence

$$pK_a = 9.03 \pm 0.06 .$$

As in the case of CH08, perfect agreement of pKa constants was achieved for the two kinds of spectroscopic characteristics. The lowering of pKa value in respect to free tyrosine, which is even greater than in the case of CH08 oligopeptide, can be explained by the presence of two positively charged arginines in the tyrosine closest vicinity.

4.2.7. CD spectra of JS01 oligopeptide

CD spectra of JS01 oligopeptide were measured at two pH (water - pH 5.0; sodium bicarbonate buffer - pH 11.0). Similarly to CH08 a negative band at 196 nm was observed in the spectral region 190–240 nm at all measured pH. In neutral pH it was accompanied by a negative shoulder around 230 nm whereas in the basic pH the shoulder shifted to around 225 nm and its intensity increased (see Figure 33).

Bands at 196 nm and about 230 nm can be attributed to π - π^* and n - π^* backbone transitions and assigned to revealing unordered conformation. Likewise CH08, we assume that π - π^* B_b transitions of the tyrosine in JS01 significantly contribute to the weak spectral band observed at ~225 nm.

In spectral region 240-320 nm of distinct tyrosine bands a weak positive spectral band around 276 nm was observed for the oligomer at neutral environment. At basic pH it shifted to 294 nm and gained substantially keeping the sign of the

band. As in the case of CH08, this change of CD spectra corresponds to the acidobasic transition from tyrosine to tyrosinate [89].

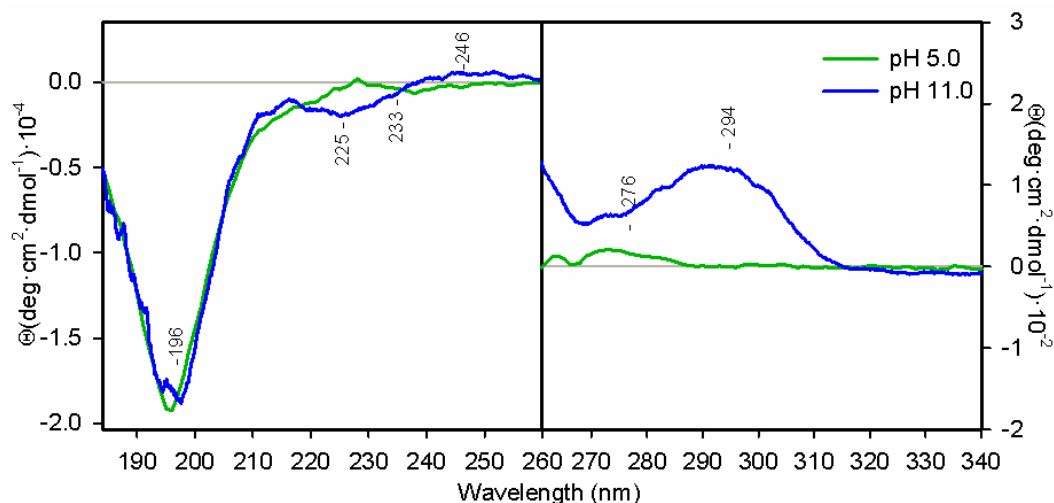


Figure 33. Electronic circular dichroism spectra of the JS01 oligopeptide in water pH 5.0 (green) and in a sodium bicarbonate buffer pH 11.0 (blue).

4.2.8. Raman spectra of JS01 oligopeptide

Raman spectrum of JS01 (Figure 34) was measured in water at pH 5.0 and treated according to the procedure described in chapter 3.2.3. Like CH08, JS01 contains one tyrosine residue and its vibrations appeared at approximately the same wavenumbers (for neutral pH). ν_{8a} and ν_{8b} bands were observed at 1617 and 1604 cm^{-1} , respectively, ring deformation modes $\delta(\text{C-H})$ at 1208 cm^{-1} and at 1177 cm^{-1} corresponding to ν_{9a} with a contribution from $\text{C}_6\text{H}_5\text{-C}$ stretching were also distinguishable as well as the bands at 832 and 855 cm^{-1} of the Fermi doublet and 643 cm^{-1} band of the $\delta(\text{CCC})$ deformation, ν_{6b} .

Besides the tyrosine, JS01 contains also one phenylalanine residue whose vibrations significantly contribute to Raman spectra. Among the in-plane ring bending modes, noticeable are the strong trigonal breathing mode, ν_{12} , at 1003 cm^{-1} and the weak degenerate mode of quadratic ring deformation ν_{6b} at 621 cm^{-1} [96]. $\delta(\text{C-H})$ deformation modes are present by bands at 1033 cm^{-1} , ν_{18a} ; 1159 cm^{-1} , ν_{15} ; 1170 cm^{-1} , ν_{9a} and 1466 cm^{-1} , ν_{19b} [96]. The band at 1206 cm^{-1} corresponds to ring C stretching vibration. Quadratic ring stretching modes ν_{8b} and ν_{8a} appear at 1583 cm^{-1} and 1604 cm^{-1} respectively [96].

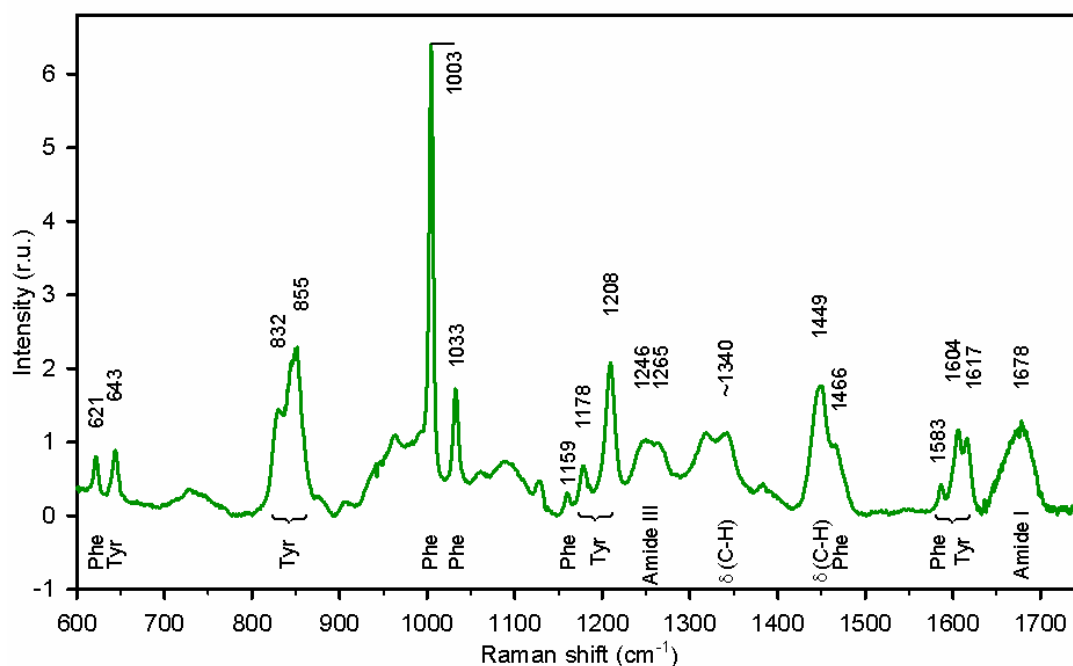


Figure 34. Raman spectrum of JS01 oligopeptide measured in water at pH 5.0. Most distinctive bands are assigned according to the literature [71-72, 96-97].

Information about secondary structure can be derived from the position and shape of the amide I and amide III bands. The amide I band is located at 1678 cm^{-1} . The amide III consists of two components (at 1246 cm^{-1} and 1265 cm^{-1}) of approximately the same intensity. Maximum of the amide I at $\sim 1678\text{ cm}^{-1}$ points on a possible presence of β -sheet, β -turns or β -hairpins along with random coil/unordered structures. The two bands at 1246 and $\sim 1265\text{ cm}^{-1}$ in the amide III region confirm this conclusion [90-91]. It is in a general agreement with an estimation of the secondary structure from the primary peptide sequence by GOR [92] and Chou and Fasman [93] algorithms (data not shown).

4.2.9. Raman spectra of JS03 oligopeptide

Raman spectrum of JS03 (Figure 35) was measured in water at pH 5.0 and treated according to the procedure described in chapter 3.2.3. Like JS01, JS03 contains one phenylalanine residue and its vibrations appeared at approximately the same wavenumbers. Noticeable in-plane ring bending modes are the strong ν_{12} at 1003 cm^{-1} and the weak ν_{6b} at 621 cm^{-1} [96]. $\delta(\text{C-H})$ deformation modes are present by bands at 728 cm^{-1} (ν_{11}), 1033 cm^{-1} (ν_{18a}), 1159 cm^{-1} (ν_{15}), and a shoulder at 1470 cm^{-1} (ν_{19b}) [76, 96]. The band at 1207 cm^{-1} corresponds to ring C stretching vibration. Quadratic ring stretching modes ν_{8b} and ν_{8a} appear at 1584 cm^{-1} and 1605 cm^{-1} respectively [96].

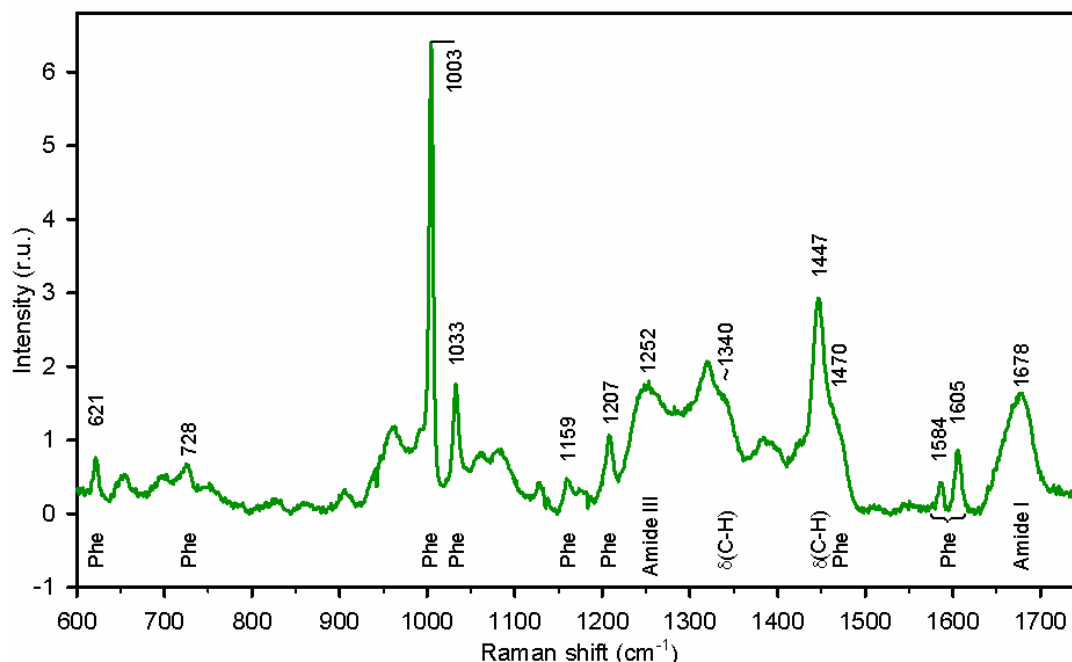


Figure 35. Raman spectrum of JS03 oligopeptide measured in water at pH 5.0. Most distinctive bands are assigned according to the literature [71, 76, 96].

The secondary structure is estimated from the position and shape of the amide I and amide III bands at 1678 cm^{-1} and 1252 cm^{-1} respectively. Maximum of the amide I at $\sim 1678\text{ cm}^{-1}$ points on a possible presence of β -sheet, β -turns and β -hairpins along with random coil/unordered structures. The band at 1252 cm^{-1} in the amide III region confirms this conclusion [90-91]. It is in a general agreement with the estimation of the secondary structure from the primary peptide sequence by GOR [92] and Chou and Fasman [93] algorithms (data not shown). Based on this analysis

it may be stated that the JS03 tends to form β -hairpin structure (with about the same probability as CH08) that is in a dynamical equilibrium with an unordered/random coil structure.

4.2.10. Raman spectra of JS02 oligopeptide

Raman spectrum of JS02 (Figure 36) was measured in water at pH 5.0 and treated according to the procedure described in chapter 3.2.3. Oligopeptide JS02 has the same sequence as JS03 except a point mutation at position of phenylalanine (Phe \rightarrow Trp). Tryptophan vibrations significantly contribute to Raman spectra. Its Fermi doublet appears at 1340 and 1360 cm^{-1} [76, 99]. The band at 877 cm^{-1} corresponds to mode ν_{17} [76, 99]. Indole ring vibrations appear at 1620 cm^{-1} (ν_1 mode), 1579 cm^{-1} (ν_2), 1553 cm^{-1} (ν_3), 1012 cm^{-1} (ν_{16}) and indole ring-breathing vibration ν_{18} at 759 cm^{-1} [76, 100]. The band at 1130 cm^{-1} belongs to indole ring bending and the bands at 1236 and 1253 cm^{-1} can be assigned to pyrrole ring vibrations [101].

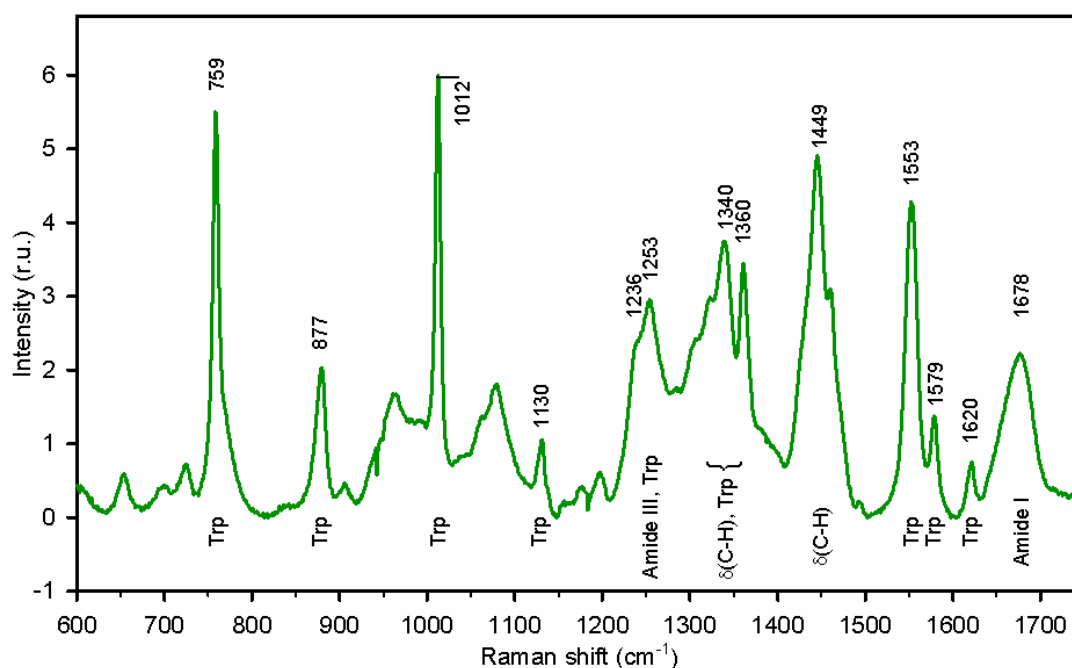


Figure 36. Raman spectrum of JS02 oligopeptide measured in water at pH 5.0. Most distinctive bands are assigned according to the literature [71, 76, 99-101].

Secondary structure of this oligomer was determined similarly to its analog JS03 described in the chapter 4.2.9. JS02 oligopeptide also tends to form a β -hairpin structure (with about the same probability as CH08 and JS02) that is in a dynamical equilibrium with an unordered/random coil structure.

4.3. Longer segments of MADS box

Oligopeptides of 42 amino-acid length (see Figure 37) were used to examine interaction of the MADS box with its DNA target. These oligomers (residues 139-180) contain the N-extension and α 1-helix of the human SRF which is responsible for DNA binding. The two tyrosines Y173 and Y158 serve as inner spectroscopic probes sensitive to changes in their closest environment, therefore in different parts of the oligopeptide. To determine, which part of the oligopeptide is influenced by the interaction, two analogue sequences with a single point mutation (Tyr \rightarrow Phe) in either tyrosine position were employed as reference samples.

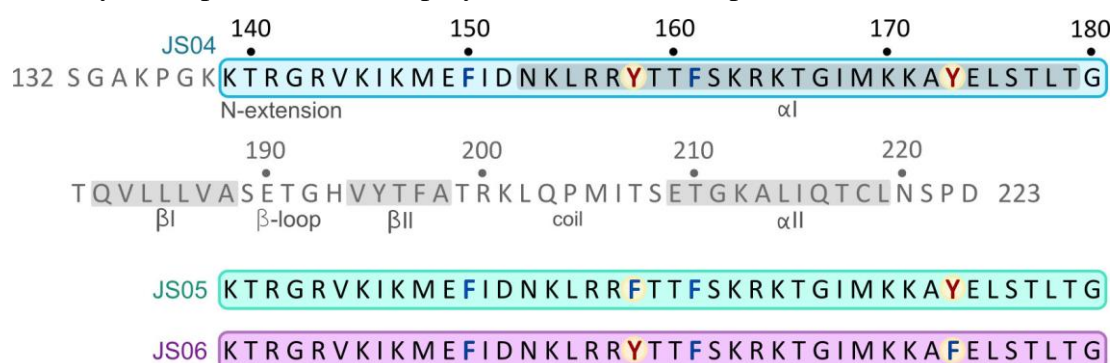


Figure 37. Longer model oligopeptides within the sequence of human SRF. Secondary structure according to X-ray [26].

4.3.1. Raman spectra of longer oligopeptides

Raman spectra of JS04-6 (Figure 38) were measured in water at pH 4.0 and treated according to chapter 3.2.3. The three spectra have been scaled to match the intensities at 1447 cm^{-1} . These oligomers contain both tyrosine and phenylalanine residues whose vibrations dominate their spectra.

At pH 4, the pair of bands at 1617 and 1606 cm^{-1} corresponding to the in-plane stretching vibrations of the tyrosine ring ν_{8a} and ν_{8b} , respectively, was observed. Raman bands resulting from the ring deformations occur at 1208 cm^{-1} and at

1178 cm^{-1} (ν_{9a} with a contribution from $\text{C}_6\text{H}_5\text{-C}$ stretching) [71]. The bands at 831 and 854 cm^{-1} are assigned to the tyrosine Fermi resonance (modes ν_1 and ν_{16a}) [75]. The 644 cm^{-1} band corresponds to tyrosine ν_{6b} mode.

Phenylalanine also generates numerous prominent Raman bands. Notable are in-plane ring bending modes: the strong trigonal breathing mode ν_{12} at 1003 cm^{-1} and the weak degenerate mode of quadratic ring deformation ν_{6b} at 622 cm^{-1} [96, 102]. $\delta(\text{C-H})$ deformation modes occur at 1032 cm^{-1} (ν_{18a}) and 1159 cm^{-1} , (ν_{15}) [96]. Ring C stretching vibration corresponds to the band at 1208 cm^{-1} . The 1586 cm^{-1} and 1606 cm^{-1} lines result from quadratic ring stretching ν_{8b} and ν_{8a} , respectively [96].

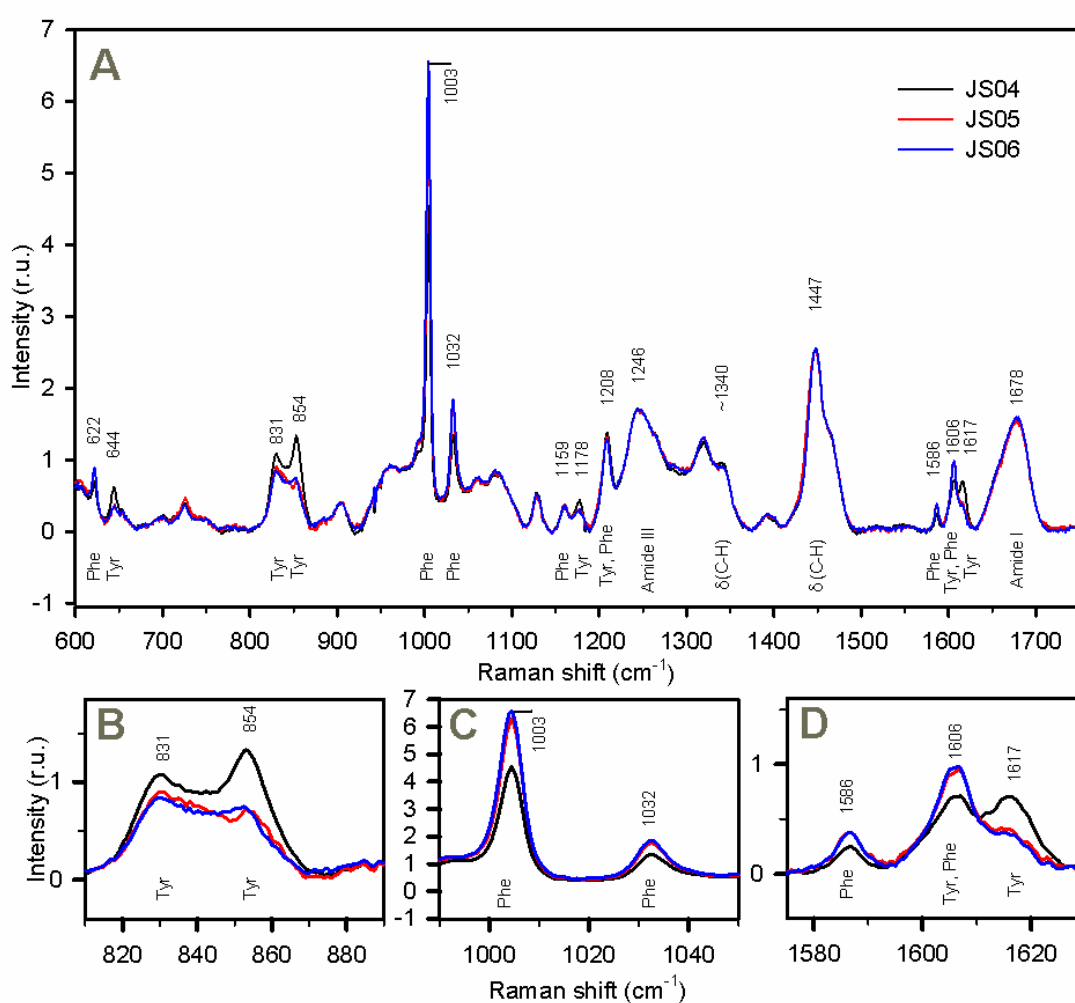


Figure 38. Raman spectra of JS04, JS05, and JS06 oligopeptides measured in water at pH 4.0. Most distinctive bands are assigned according to the literature [71, 75-76, 96, 102]. Besides the overall spectra (A), details of important spectral regions are shown below: (B) Tyrosine Fermi doublet, (C) Characteristic phenylalanine vibrations, (D) In-plane stretching vibrations of tyrosine and phenylalanine rings.

A tyrosine to phenylalanine substitution does not cause any measurable change of the shape of amide I and III bands, which indicates that the structure of the oligopeptide remains unchanged. Estimation of the secondary structure content was achieved by using least-square analysis method in the region of amide III band. We have found 48 % of β -sheet content, 15 % of β -turn content and 29 % of α -helix content. Structural difference between the three oligopeptides JS04-6 was negligible.

4.3.2. Absorption and fluorescence spectra of longer oligopeptides

Absorption and fluorescence spectra of 50 μ M JS04-6 oligopeptides were measured in 5 mM phosphate buffer pH 7.1 and treated according to chapters 3.2.1 and 3.2.2 (see Figure 39). In the fluorescence emission spectra of JS04-6 oligopeptides, a characteristic peak at 303 nm was observed. These spectra emitted by tyrosines within large molecules are red shifted about 1 nm compared to a free tyrosine residue. Absorption spectra of JS05 and JS06 (both possessing 1 Tyr and 3 Phe) are about the same and differ from JS04 which, in respect to them, lack one phenylalanine and possess one additional tyrosine residue (i.e. it has 2 Tyr and 2 Phe).

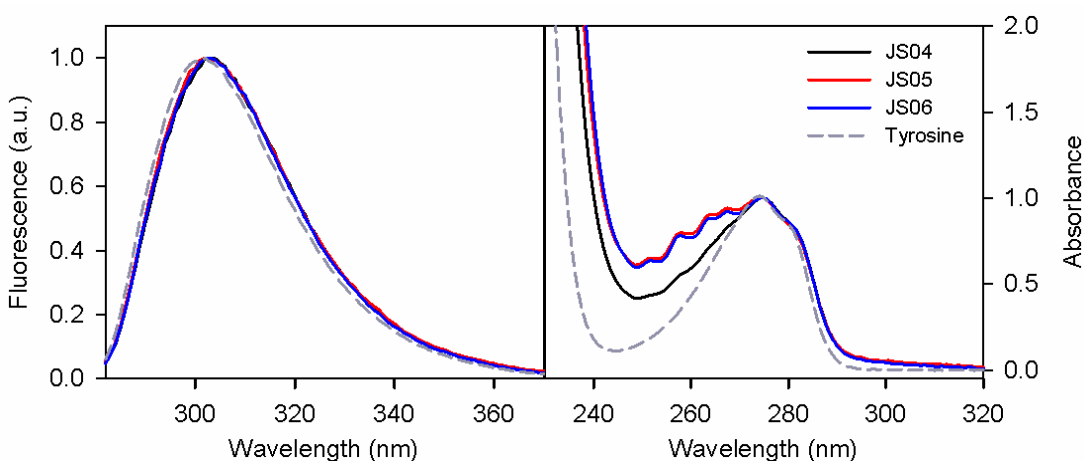


Figure 39. Comparison of JS04-6 oligopeptide and tyrosine corrected fluorescence (left) and absorption (right) spectra. Fluorescence and absorption spectra are normalized at 302 nm and 275 nm respectively.

4.4. MADS box

The conserved sequence of the MADS box forms a part of core domain of many members of the MADS box family of transcription factors (see Figure 40). Therefore its study may underline basic functional properties of the whole protein family. Its N-terminal basic part enables DNA specific sequence recognition and binding, whereas the C-terminal hydrophobic segment forms a protein dimerization domain. The three tyrosine residues of the MADS box were used as spectroscopic internal probes. To distinguish their individual contributions to the spectra and their further characterization, the effect of small changes of the environmental conditions especially the effect of pH and presence of variously charged quenchers were examined. The results of the MADS box study are part of the submitted article [III].

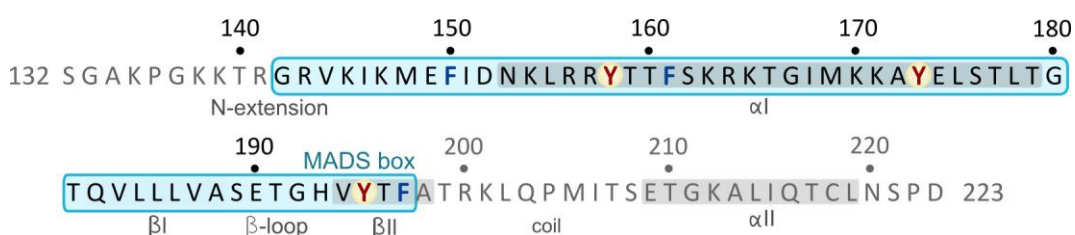


Figure 40. The MADS box segment of human SRF. Secondary structure according to X ray [26].

The secondary structure of the MADS box has been first estimated from its primary sequence using Chou and Fasman and GOR algorithms [III]. They predicted that the C-terminal part (amino acids 181–197) folds into β -strands and adopts a β -hairpin like topology, while the N-terminal part (amino acids 142–180) forms a strand of alternating short β -sheet and α -helical segments. This estimation well corresponded to the analysis of the amide I and III bands of Raman spectra [III]. A 64-69 % of β -sheet content, 22–25 % of β -turn content and ~2 % of α -helix content was found. Structural difference between the MADS box at pH 4.5 and 7.0 was found to be negligible. The intensity of the tyrosine doublet $I_{854}/I_{828} = 1.3$ reflected that the majority of tyrosines is placed on the surface of the peptide, and exposed to weak or moderate H-bonding as both donors and acceptors.

4.4.1. Fluorescence of the MADS box

The fluorescence emission spectrum of the MADS box displays a three-humped emission composed of a shoulder on the shorter wavelengths (ca. 293 nm), a peak at 304 nm, and a weak shoulder on the longer wavelengths of the spectrum around 325 nm (see Figure 41). Fluorescence excitation spectra of the MADS were recorded for fluorescence emitted at the above mentioned wavelengths (see Figure 41). While the excitation spectrum for emission at 293 nm has a simple shape with maximum at 277 nm, spectra for emissions at 304 and 325 nm manifest an additional shoulder at ~268 nm and the latter also a weak band at ~300 nm.

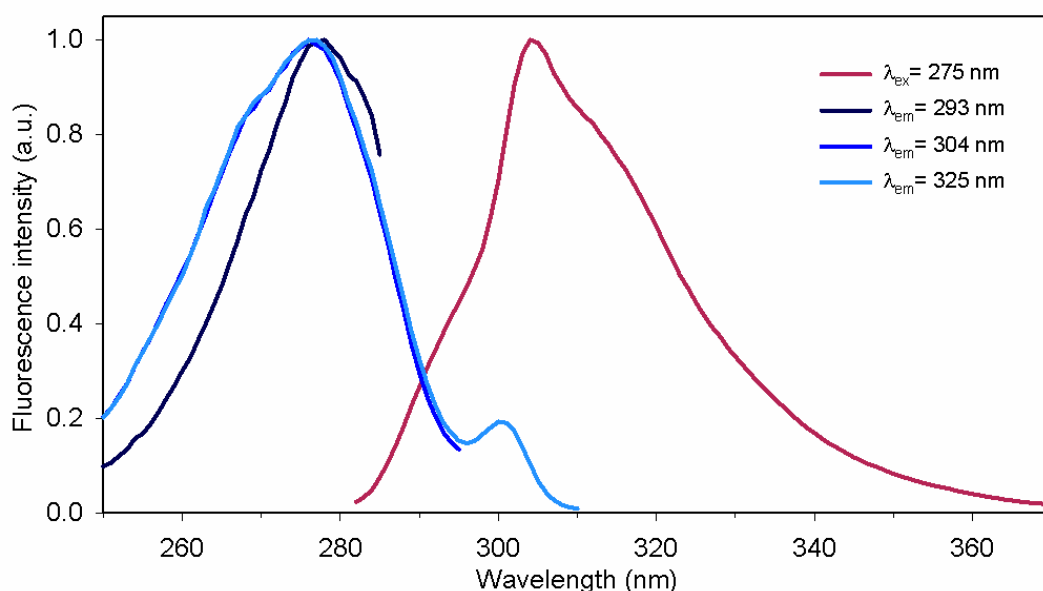


Figure 41. Normalized fluorescence emission (red) and excitation (blue) spectra of the MADS box in water. The emission spectrum was excited at 275 nm. The excitation spectra were recorded for emissions at 293 nm, 304 nm, and 325 nm.

The additional fluorescence features indicate either presence of tyrosine in its deprotonated form (tyrosinate) or engaged in a strong or unusual hydrogen bond (i.e. between charged residues) [64, 103]. Both emission and excitation spectra were measured in water at pH 5.6, therefore, presence of tyrosinate seems to be unlikely. On the other hand, formation of internal H-bond is possible between Tyr195 and His193 (the His residue is positively charged at the given pH). To check the possibility of H-bond presence, hydrogen atoms were added to the published X-ray structure of SRF dimer bound to target DNA [26] (see Figure 42). In this H-bond

tyrosine probably acts as a proton acceptor and histidine as a donor (similar case is described in Fernandez-Recio, 1999 [104]). The distance of H...O is ca. 1.91 Å, which corresponds to the standard H-bond length. While the length 1.01 Å of the chemical N–H bond in histidine is standard.

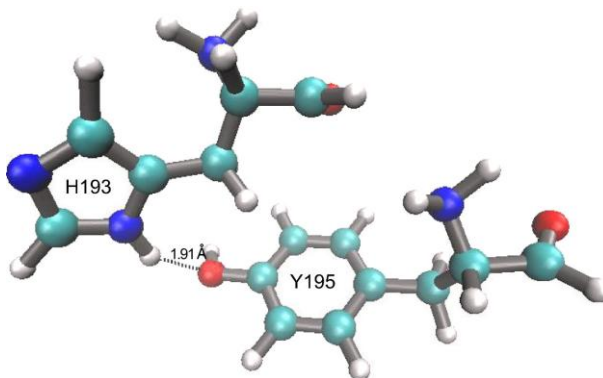


Figure 42. Possible H-bond formation between tyrosine and histidine in the X-ray structure of the SRF MADS box [26] (visualized using the VMD [61]). The distance of H..O is ca.1.9 Å.

4.4.2. MADS box fluorescence quenching

To determine the accessibility of the tyrosine residues to solvent and charges, quenching of 10 μM MADS box oligopeptide fluorescence by charged quenchers (Cs^+ and Γ) were performed in 25 mM cacodylate buffer pH 6.5. Increasing the concentration of the quencher a decrease of the fluorescence intensity was observed, while the absorption spectra remained almost unaffected by the quencher adding (data not shown). Measured spectra were treated as described in chapter 3.2.1 and 3.2.2.

The sets of fluorescence spectra obtained for various concentrations of either of the quenchers were individually subjected to factor analysis (SVD), for details see chapter 3.3.1. In both cases the factor dimension equals to two, meaning that all fluorescence spectra can be reconstructed as linear combinations of just two subspectra, S_1 and S_2 . Figure 43 shows the SVD results of the quenching by iodide. By a fit of V_1 and V_2 dependences to Stern–Volmer equation (for details see chapter 3.3.2.) we obtained the same two major components of emission spectrum for both quenchers, F_I and F_{II} (see Figure 44) for fluorescence components revealed by iodide quenching).

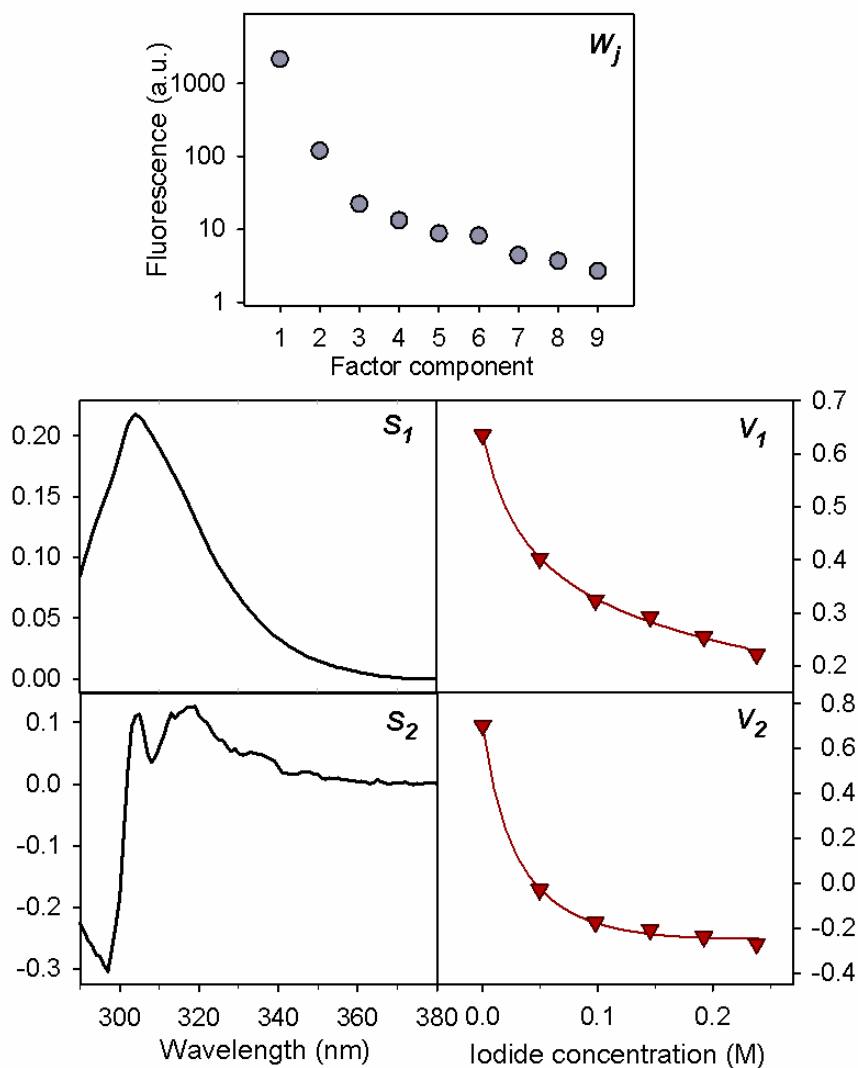


Figure 43. The factor analysis (SVD) results of the MADS-box emission spectra quenched by iodide. Red solid lines represent the fit of coefficients according to Stern-Volmer equation.

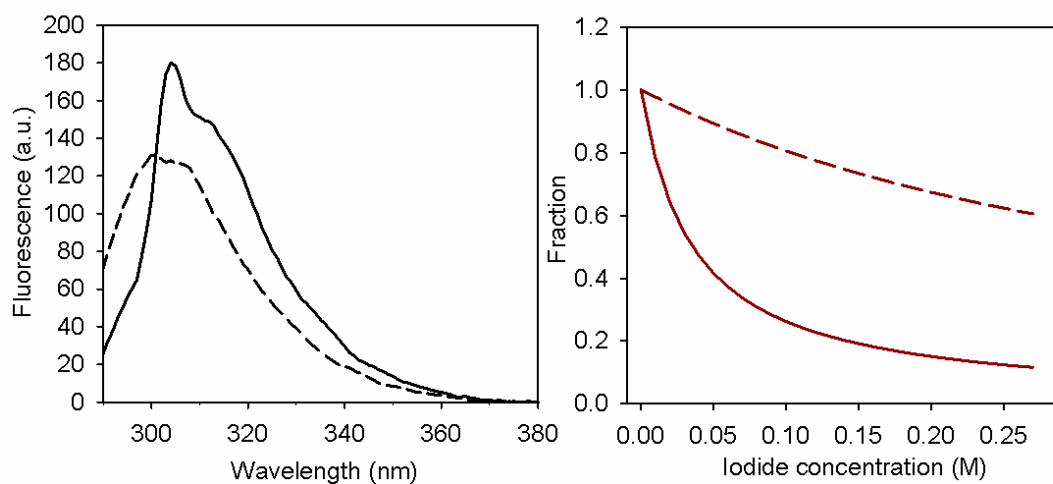


Figure 44. Two differently quenched spectral components (left) and their decreasing fractions in the spectra of the MADS box with increasing iodide concentrations (right). Solid lines correspond to the more efficiently quenched F_I component and dashed lines to the second component F_{II} .

Due to the similarity of SVD results for both quenchers (factor dimension of two; similar shapes of subspectra S_1 and S_2 ; and also of the spectral components F_I and F_{II} obtained by an analogous fit) a joint fit as described in chapter 3.3.2 was performed (see Figure 45). Two common components, F_I and F_{II} were obtained (see Figure 46) each of them characterized with a certain Stern–Volmer constant K^Q , a measure of the quenching efficacy. In particular, for spectral component F_I : $K_I^I = 33.2 \pm 7.0 \text{ M}^{-1}$ and $K_I^{\text{Cs}} = 3.4 \pm 0.5 \text{ M}^{-1}$ and, for component F_{II} : $K_{II}^I = 2.5 \pm 0.8 \text{ M}^{-1}$ and $K_{II}^{\text{Cs}} = 0.2 \pm 0.2 \text{ M}^{-1}$.

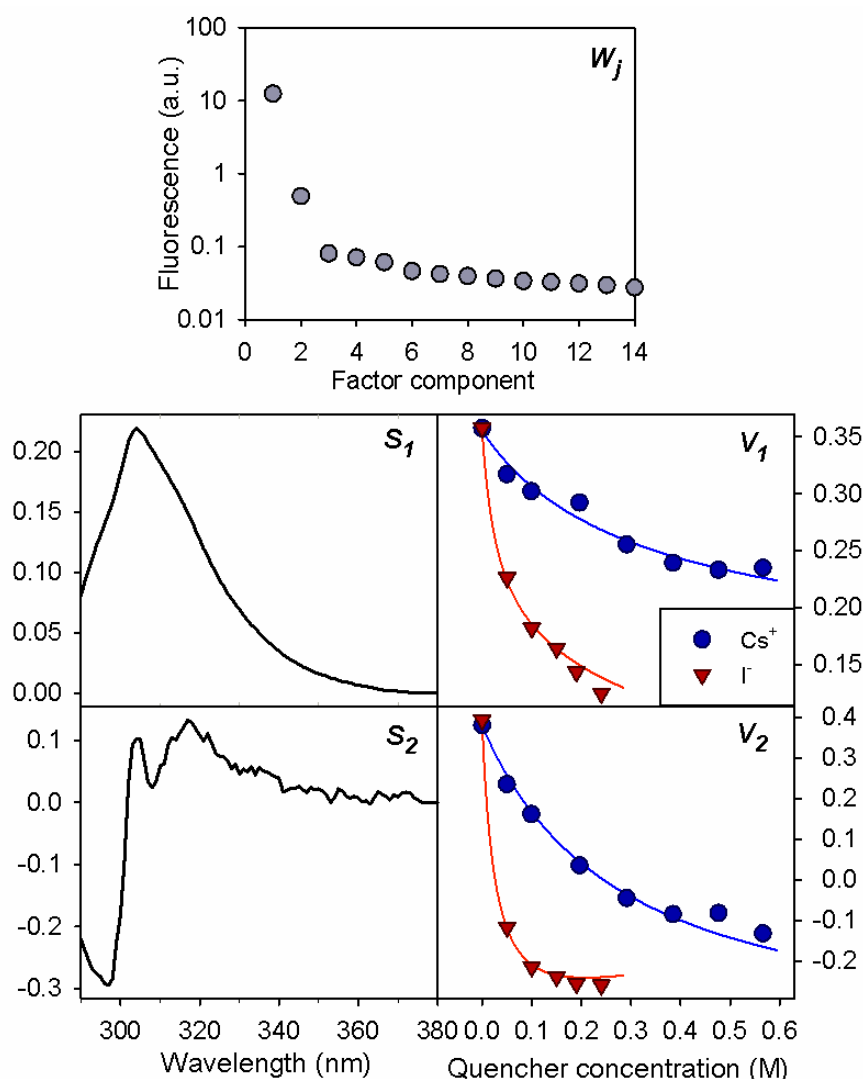


Figure 45. The factor analysis (SVD) results of the MADS-box emission spectra quenched by iodide (red triangles) and cesium (blue circles). Solid lines represent the fit of coefficients according to Stern-Volmer equation.

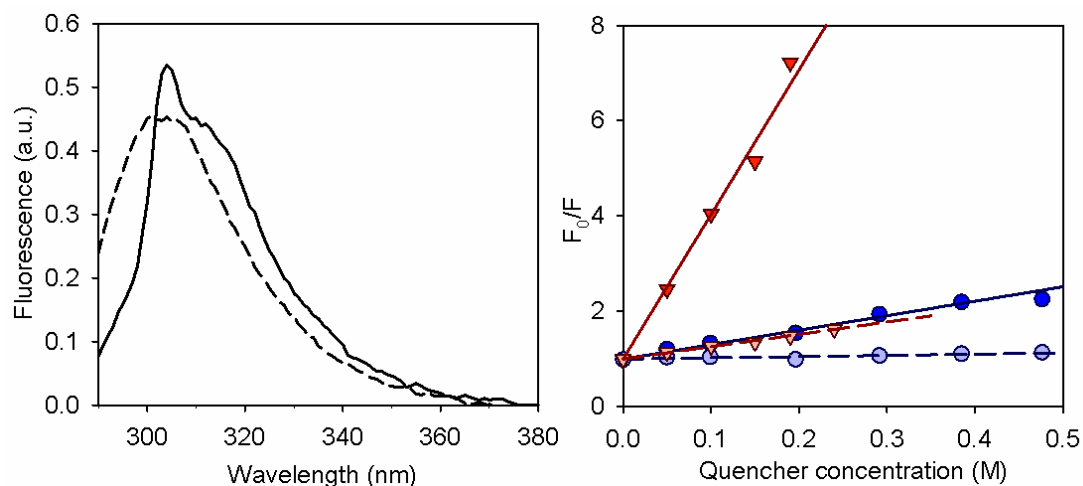


Figure 46. Two differently quenched spectral components (left) and their Stern-Volmer representation (right). Solid lines correspond to the more efficiently quenched F_I component and dashed lines to the second component F_{II} . Circles and red color correspond to Cs^+ , triangles and blue to Γ quenching.

The more efficiently quenched component F_I possesses the more complicated shape (with maximum at 304 nm). The spectral shape of the less efficiently quenched component F_{II} is simpler and similar to the emission spectra of free tyrosine. The ratios of Stern-Volmer constants of iodide over caesium K^I/K^{Cs} are nearly the same for both components F_I and F_{II} and amount to about 10. It means that iodide quenches fluorescence of both components significantly more efficiently than caesium, while the Stern-Volmer constant ratio K_I/K_{II} remains similar independently on the quencher charge.

The Stern-Volmer constant depends on the efficiency of the quencher as well as the quencher diffusion and its influencing by electrostatic effects [105]. As Γ and Cs^+ provide a pair of quenchers with opposite charges and similar diffusion parameters [105], it could be anticipated that due to their different charge they would quench preferentially tyrosines surrounded by environment of opposite charge. Contrary to this assumption the same ratio of the Stern-Volmer constant K^I/K^{Cs} was observed for both components F_I and F_{II} . Therefore, the quenching mainly resolves the global solvent accessibility and does not differentiate between various microenvironments of the Tyr residues.

4.4.3. Fluorescence and absorption pH dependency of the MADS box

The fluorescence and absorption spectra were measured in the pH range from 3.0 to 9.5 at temperature 20°C and concentration of 5 μM . In general, increasing the pH from 3 to 7 causes a decrease of the fluorescence intensity while no significant change in the absorption spectra is observed. Further increase of pH causes that the fluorescence intensity drops even more significantly, while absorption bands shift to higher wavelengths. Above pH 9.5 the MADS box precipitates (the peptide denaturation is irreversible, data not shown). Spectra corrected according to chapters 3.2.1 and 3.2.2 are shown in Figure 47.

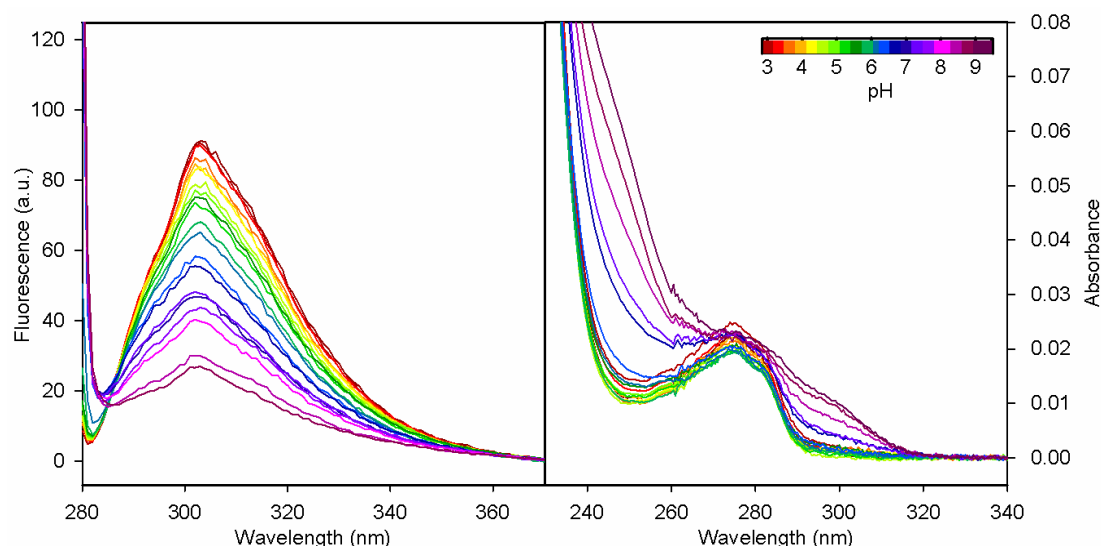


Figure 47. pH dependence of the MADS box fluorescence and absorption spectra. From acidic (red) to basic (violet) pH.

To obtain more specific information about the changes induced by pH variations in the range below the precipitation limit, both spectral sets were subjected to SVD separately. The factor dimension was found to be three in both cases, but the pK_a values obtained by a fit to a model considering two acido-basic equilibria were different for absorption and for fluorescence spectra. Therefore a joint fit of coefficients obtained from SVD was performed (see Figure 48, for details see chapter 3.3.3) and determined three corresponding kinds of acido-basic equilibria and four different spectral components. The acquired values of dissociation constants are: $pK_{a1} = 6.4 \pm 0.2$, $pK_{a2} = 7.3 \pm 0.2$, and $pK_{a3} = 9.6 \pm 0.6$. The isolated four spectral

components of fluorescence emission (F^A , F^B , F^C , F^D) and of UV absorption ($F^{A'}$, $F^{B'}$, $F^{C'}$, $F^{D'}$) are shown in Figure 49.

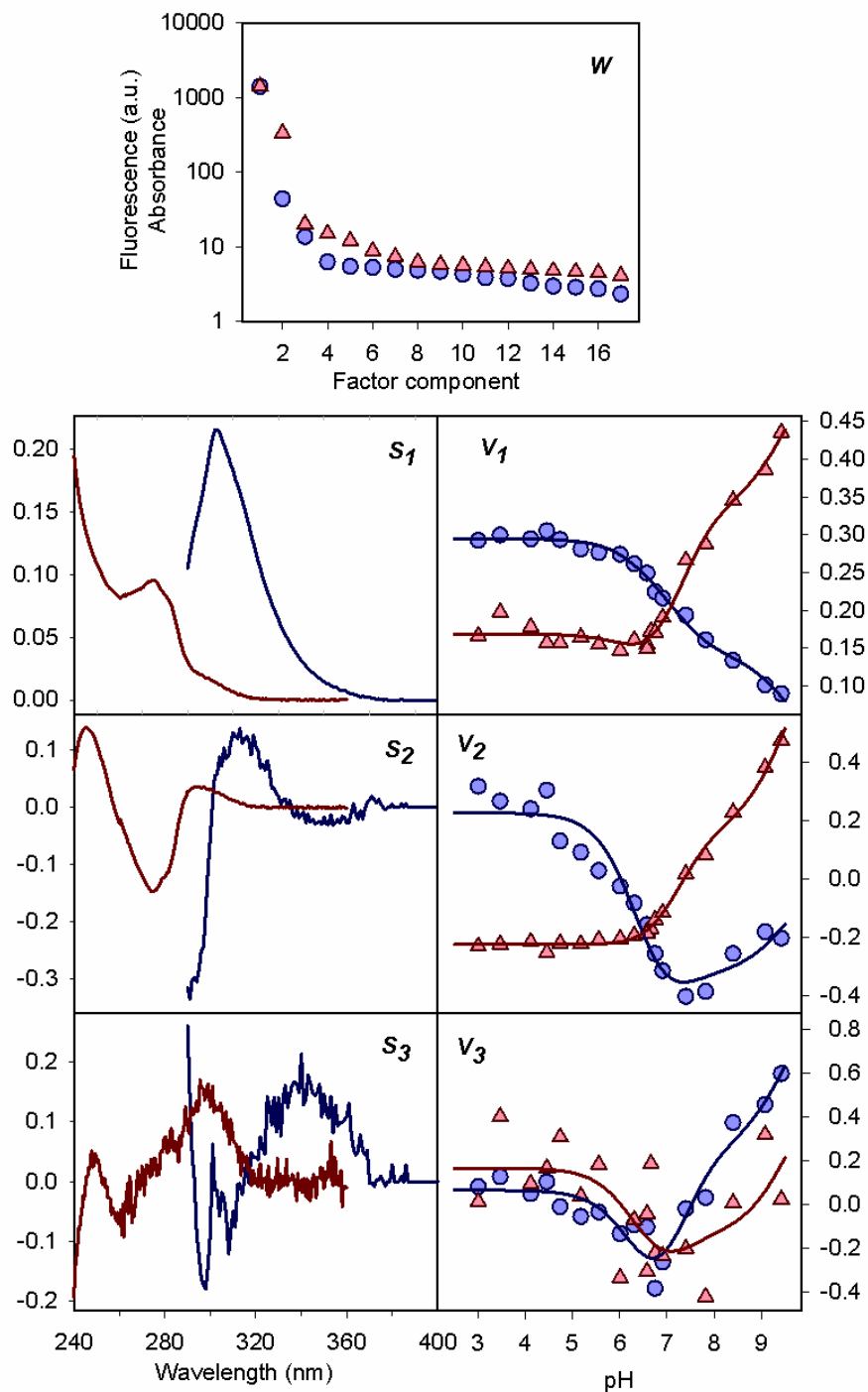


Figure 48. The factor analysis (SVD) results of both fluorescence and absorption spectral pH titration of the MADS box shown in common graphs. Solid curves inside the graphs of coefficients show the joint fit according to the model of three acido-basic equilibria.

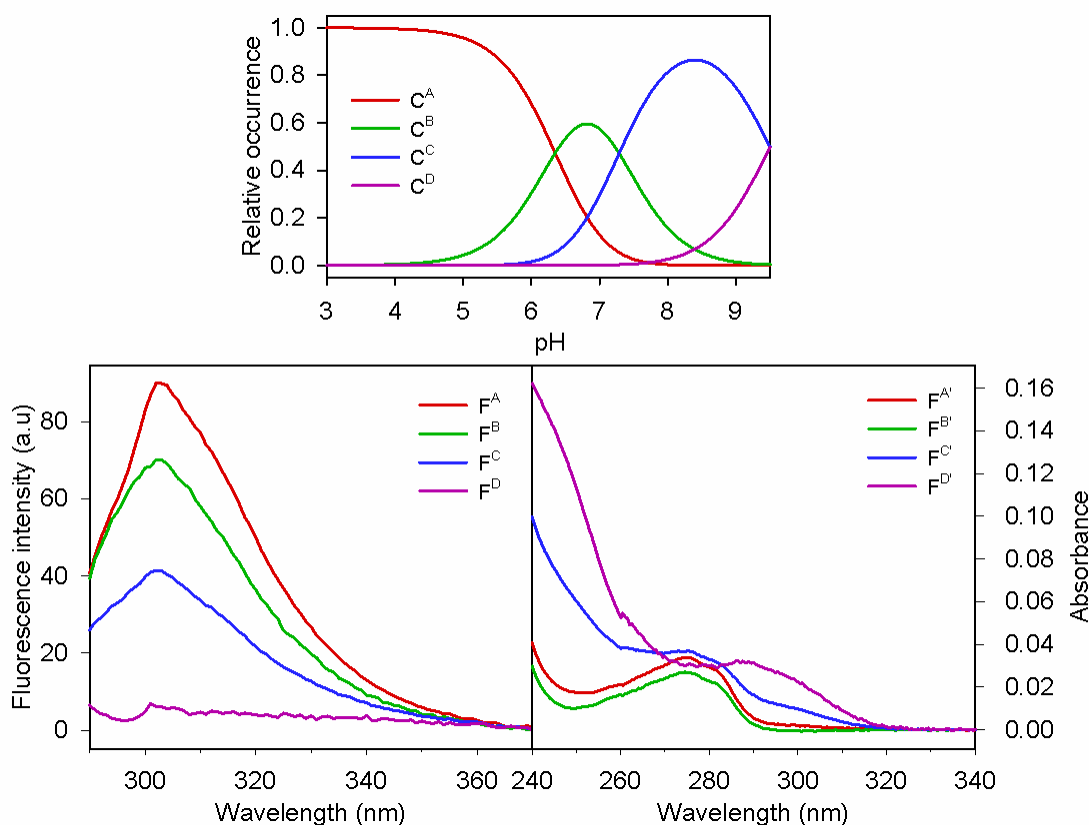


Figure 49. Absorption spectral components $F^{A'}$, $F^{B'}$, $F^{C'}$, $F^{D'}$ (lower right) and fluorescence spectral components F^A , F^B , F^C , F^D (lower left) extracted by a joint fit of the SVD results of the MADS-box pH titration. Relative occurrences of particular components at various pH are shown in the upper graph.

Absorption components $F^{A'}$ and $F^{B'}$ are nearly identical. They resemble the absorption spectrum of free tyrosine and differ from each other only by a multiplication factor close to unity. $F^{D'}$ component resembles the spectrum of free tyrosinate, but still contains some tyrosine contribution. It is probably caused by the restriction of the upper pH limit of the measurement to 9.5 (due to the strong sample precipitation). Component $F^{C'}$ represents a state where part of tyrosines is converted into tyrosinate form. We may consider two possible combinations: (i) $2 \times \text{Tyr}$ and $1 \times \text{tyrosinate}$ or (ii) $1 \times \text{Tyr}$ and $2 \times \text{tyrosinate}$. The resulting spectra, given by such combination of $F^{B'}$ and $F^{D'}$ components, are shown in Figure 50. It is obvious that the variant (i) corresponds, in contrast to the variant (ii), well to the spectral shape of $F^{C'}$ component.

In fluorescence, F^D component shows only a subtle fluorescence, thus it can be assigned to tyrosinate (consistently with absorption). Normalized components F^C and F^B resemble each other; however, F^C has notably stronger fluorescence above

330 nm. It points out that some of tyrosines are transformed into tyrosinate form. Similarly to absorbance, F^C component can be expressed as linear combination of F^B and F^D components in the ratio corresponding to two tyrosines and one tyrosinate (see Figure 50). Normalized components F^A and F^B differ in the region below 305 nm and around 315 nm, and they are nearly identical above 335 nm (see Figure 51). The difference ($F^A - F^B$) is characterized by an absence of low frequency shoulder at 295 nm. A sharp increase is observed up to 304 nm (maximum), then shoulder at 315 nm and subsequent decrease of the signal at higher wavelengths.

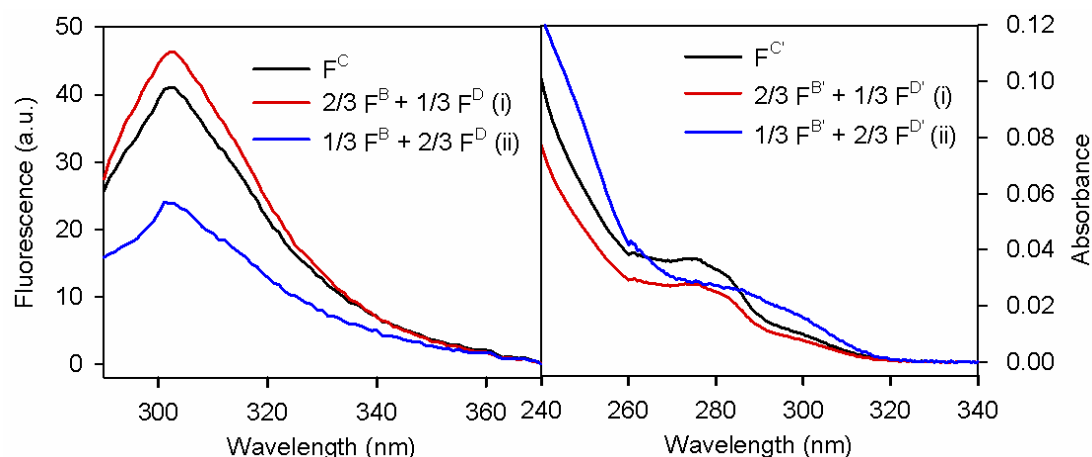


Figure 50. F^C (and $F^{C'}$) fluorescence (and absorption) component and its comparison with two considered linear combination of F^B and F^D ($F^{B'}$ and $F^{D'}$) components.

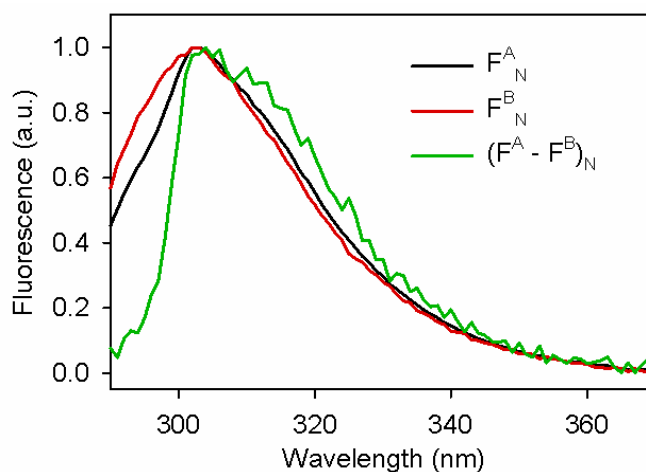


Figure 51. Comparison of components F^A and F^B and their difference spectrum. All spectra are normalized at their maxima.

The apparent analogy of $(F^A - F^B)$ spectral shape with the effect of excitation wavelength on fluorescence spectrum indicates relation between the acidobasic equilibrium with pK_{a1} and a change of Tyr195 H-bonding to His193. This

leads to interpretation of the acido-basic transition as a deprotonation of His193. The pK_a of free histidine side chain is 6.0 [3]; this value can be higher when His is inside the peptide chain: The pK_a of His34 in wild-type apoflavodoxin is 6.36 [104]; pK_a values of protein histidiny residues in unfolded proteins were found in the interval 6.5-6.6 [106-108]. Further, it is known that H-bonds between His and Tyr are stabilizing even in the case of a charged form of His (0.7 kcal/mol) [104]. For the neutral form of His, the energy of H-bond is higher (1.3 kcal/mol). Computations in vacuum imply that H-bond between Tyr and charged His is stronger due to more negative enthalpy [109], however, this decrease of enthalpy is outweighed by increase of entropy (desolvation penalty). In our case, we assume that H-bond is formed between His193 a Tyr195, the excited state of which is affected while His is present in its charged form. This leads to a decrease of the fluorescence contribution ($F^A - F^B$) during the acid-base transition.

Based on the conclusions mentioned above the basic interpretation of the three acido-basic transitions is possible (see Figure 52). The first acid-base transition, given by pK_{a1} = 6.4 ± 0.2, connected with minimal change in the absorption spectrum (i.e., spectra indicate presence of only tyrosines and no tyrosinate) and with significant change in the fluorescence spectrum, can be assigned to deprotonation of His193. Between pK_{a1} and pK_{a2} the prevailing is the state when all tyrosines remain in a neutral form, tyrosines Tyr173 and Tyr158 are H-bonded to the water milieu and Tyr195 to neutral His193 (This is supported by the tyrosine Fermi doublet in Raman spectrum [III]). During the second acid-base transition with pK_{a2} = 7.3 ± 0.2, one of tyrosines is deprotonated. The last pK_{a3} = 9.6 ± 0.6 corresponds to deprotonation of remaining two tyrosines.

A considerable lowering of one of the tyrosines pK_a (to 7.3) was observed, when compared to pK_a of a free tyrosine (10.0) [3]. Such a decrease in pK_a is probably caused by presence of positively charged amino acids in a proximity to tyrosine. This effect was described for the case of tyrosine in the vicinity of Lys or Arg residues in literature [110-111]. The pK_a of tyrosine residues was discerned within short oligopeptide segment of the MADS box in the vicinity of Tyr158, ¹⁵⁴KLRRYTTFS₁₆₂, and Tyr173, ¹⁶⁸IMKKAYEL₁₇₅ (for details see chapters 4.2.1 and 4.2.6). The dissociation constants of Tyr173 and Tyr158 were determined as 9.5 and 9.0, respectively. The decrease of pK_a value of Tyr173 is caused by proximity of

two positively charged lysine residues (Lys170 and Lys171) and one negatively charged Glt174. More significant decrease of Tyr158 pK_a is caused by imminent presence of two positively charged arginine residues (Arg156 and Arg157). The segment containing Tyr195 has not been studied separately as it is predominantly hydrophobic (according to Hopp–Woods hydrophobicity scale [9, 63]).

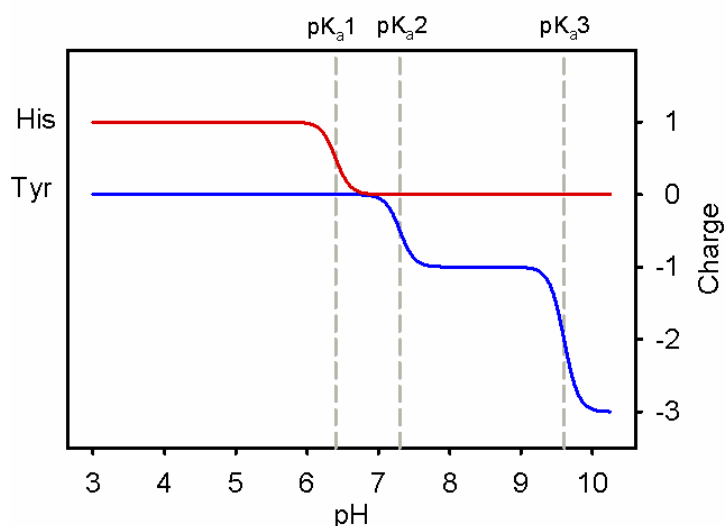


Figure 52. The most important changes of the charges of the MADS box amino acids induced by pH alteration.

Greater decrease of Tyr158 pK_a value indicates that pK_a2 constant determined from pH titration corresponds to this very residue. There is still the 1.7 gap between pH 9.0 and 7.3. However, the secondary structures of shorter sequences are dominated by extended conformation (chapters 4.2.4 and 4.2.8) and substantially differ from the ordering they possess as a part of MADS box – α -helix and β -sheet. This can lead to an additional decrease of pK_a values. Therefore, deprotonation of Tyr158 is the most probable candidate for the acid-base transition at pH 7.3.

4.5. Peptide/DNA interaction

The interaction between the MADS box and DNA was found to be so strong that in concentrations necessary for Raman measurements it immediately precipitated (data not shown). It was known that interaction of tyrosyl residues with nucleic acids leads to a quenching of tyrosine fluorescence [112-5]. Therefore fluorescence and absorption titration experiments were employed to test whether the interaction between the two partners can be examined by using the methods of electron optical spectroscopy. Two types of experiments were performed. Either the oligonucleotide solution was gradually added to oligopeptide sample, or vice versa. In both cases a parallel experiment was performed using solutions with added 0.5 M NaCl to prevent interaction between DNA and the peptide [112].

4.5.1. Addition of the oligonucleotide to the oligopeptide sample

5.7 μM solution of modSRE oligonucleotide was gradually added to 35.3 μM solution of JS06 oligopeptide and simultaneously to the solution of JS06 oligopeptide containing 0.5 M NaCl. All samples were dissolved in 5 mM phosphate buffer pH 7.1; solutions without oligopeptides were also prepared and employed as reference.

Addition of the oligonucleotide resulted in immediate precipitation. Increase of the solution turbidity brought about an additive background to absorption spectrum (see Figure 53, solution without added NaCl). No such effect was observed in spectra of solution with NaCl, where the only visible change is the increase of the absorption band (with maximum at 260 nm) caused by gradual adding the oligonucleotide solution.

Addition of the oligonucleotide caused increase of the elastic scattering of the incident light within fluorescence spectra (see Figure 54). Fluorescence quenching was not observed in such a low ratios of modSRE:JS06.

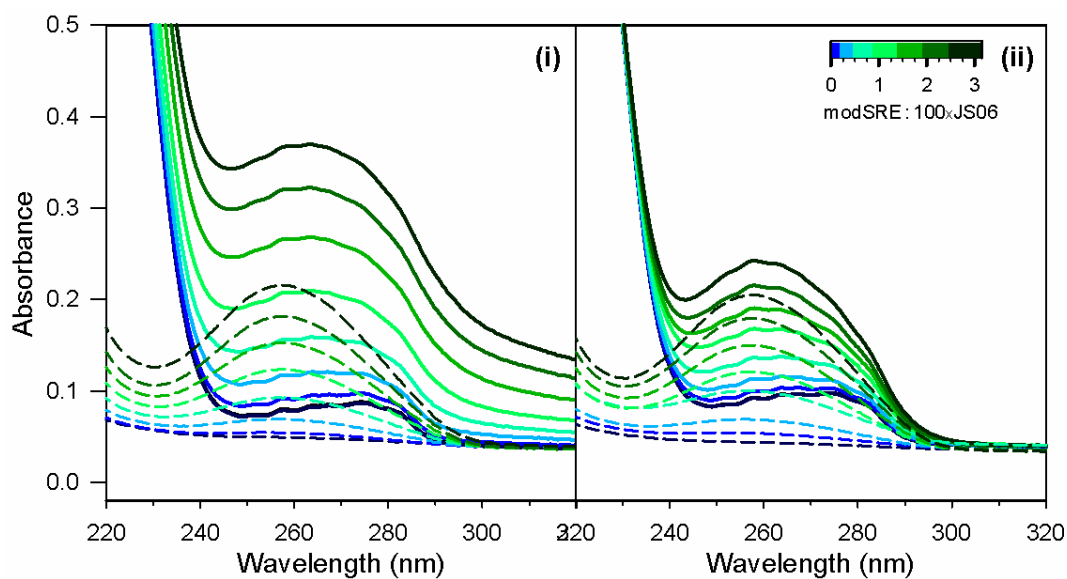


Figure 53. Measured absorption spectra of modSRE addition to JS06 sample. (i) Samples in buffer. (ii) Samples in buffer and 0.5 M NaCl. Solid lines correspond to solutions with oligopeptide, dashed lines to reference solutions.

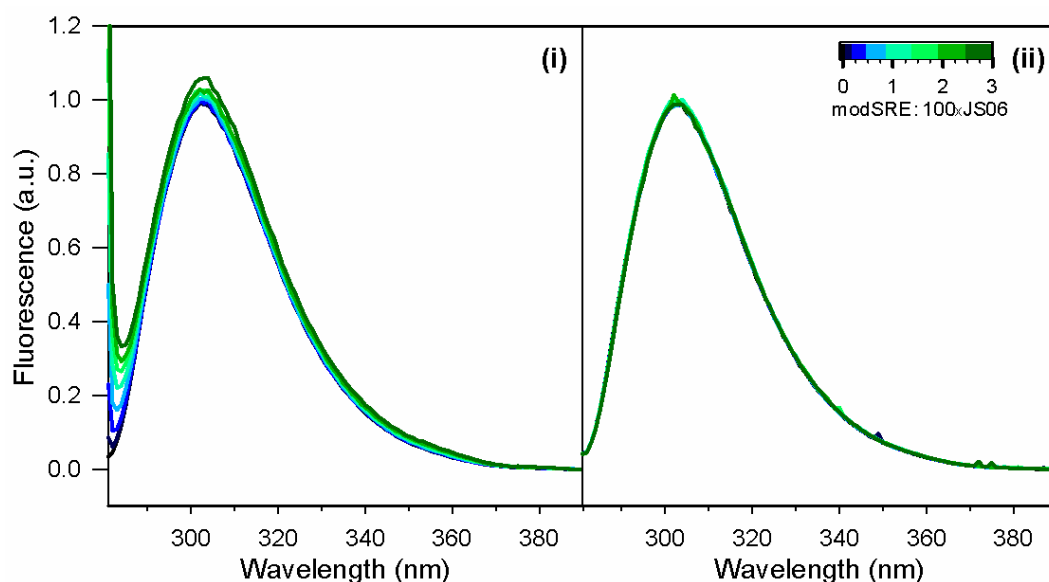


Figure 54. Corrected fluorescence spectra of modSRE addition to JS06 sample. (i) Samples in buffer. (ii) Samples in buffer and 0.5 M NaCl. Spectra were corrected for IFE*, Raman scattering, background and dilution (as described in chapters 3.2.1 and 4.1.1).

Factor analysis (SVD) of fluorescence spectra gave two dimensions (Figure 55). The first subspectrum shows average spectral shape partly distorted by elastic scattering. Second subspectrum, representing the main spectral change, shows mainly the effect of Rayleigh elastic scattering of the excitation light. The presence of the scattering within the spectra is linearly dependent on DNA/protein ratio (see coefficients V_2). This can be explained by a single oligonucleotide binding many

oligopeptides creating a large complex that precipitates. The increase of the sample turbidity is observable by increase of background in absorption spectra and elastic scattering in fluorescence emission spectra.

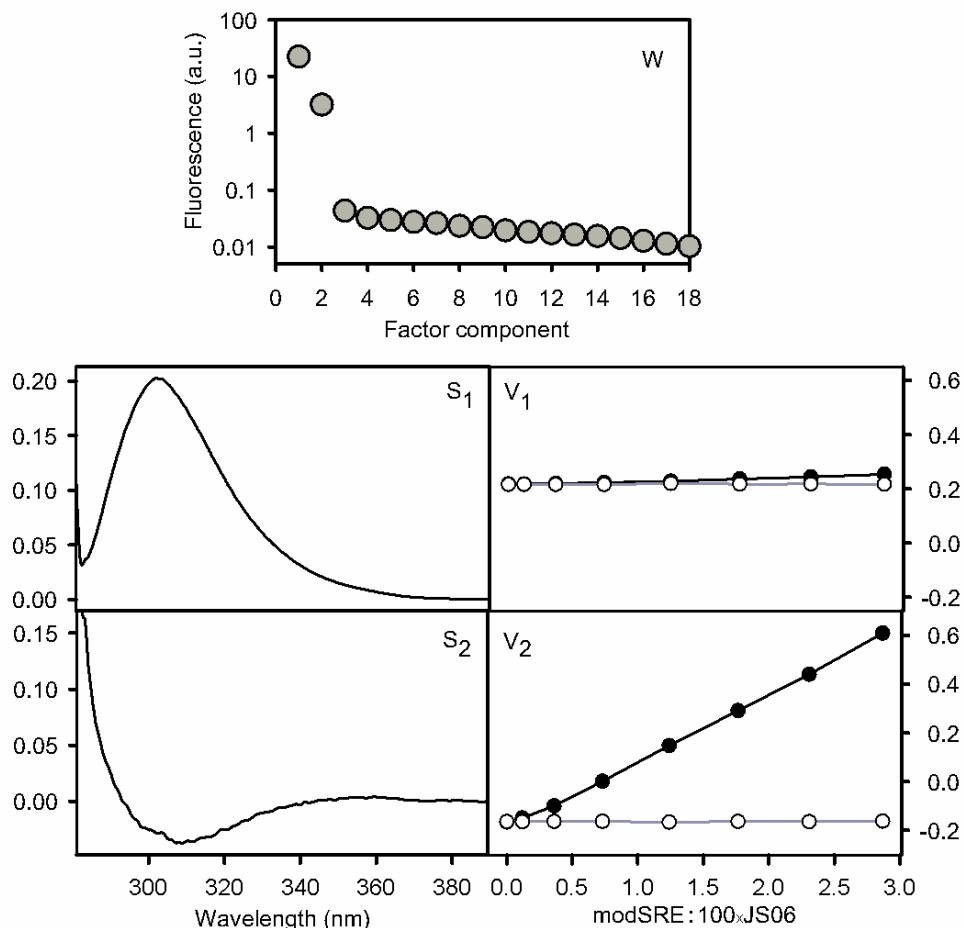


Figure 55. The factor analysis (SVD) results of fluorescence spectra during modSRE addition to JS06 sample. Black circles represent samples dissolved in buffer (i); white circles samples in buffer and 0.5 M NaCl (ii).

4.5.2. Addition of the oligopeptide to the oligonucleotide sample

The titration similar to the one described in chapter 4.5.1 but with the oligopeptide added to oligonucleotide sample, was performed. 58.1 μM solution of JS06 oligopeptide was gradually added to 3.3 μM solution of modSRE oligonucleotide and simultaneously to the solution of modSRE oligonucleotide containing 0.5 M NaCl. All samples were dissolved in 5 mM phosphate buffer pH 7.1; solutions without oligonucleotides were also prepared and employed as reference. As can be seen even from uncorrected absorption spectra, addition of

oligopeptide causes precipitation when certain peptide/DNA ratio is exceeded (see Figure 56, solution without added NaCl). The precipitation increases the solution turbidity, which brings about an additive background to absorption spectrum. No such effect is seen in spectra of solution with NaCl, where the only visible change is the slight decrease of the DNA absorption band (with maximum at 260 nm). It is caused by dilution of the oligonucleotide sample by gradual adding the oligopeptide solution with about hundredfold lower extinction coefficient.

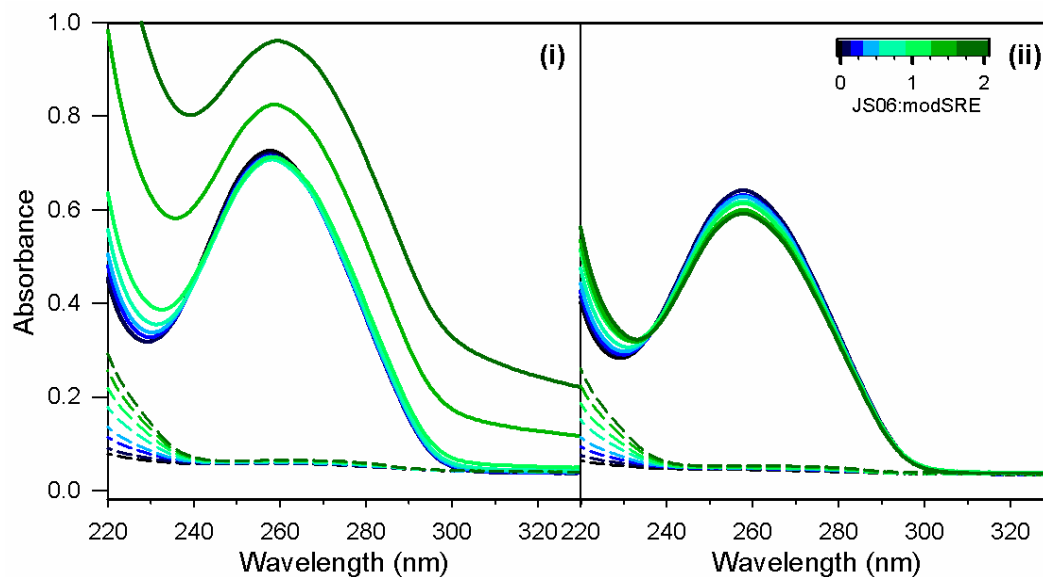


Figure 56. (i) Measured absorption spectra of modSRE solution during gradual addition of JS06 ; (ii) the same experiment for solution with 0.5 M NaCl. Solid lines correspond to the oligonucleotide solution, dashed lines to JS06 added to the reference solvent.

Absorption spectra were treated as described in chapter 3.2.2. Figure 57 shows the results of factor analysis (SVD). Factor dimension is three in this case. S_1 represents the average spectral shape, S_2 shows mainly the distortion resulting from the precipitation of the sample and S_3 shows the spectral change that might be a result of peptide/DNA interaction, since its contribution increases (see coefficients V_3) with increase of the oligopeptide concentration till the precipitation appears (in the solution without NaCl).

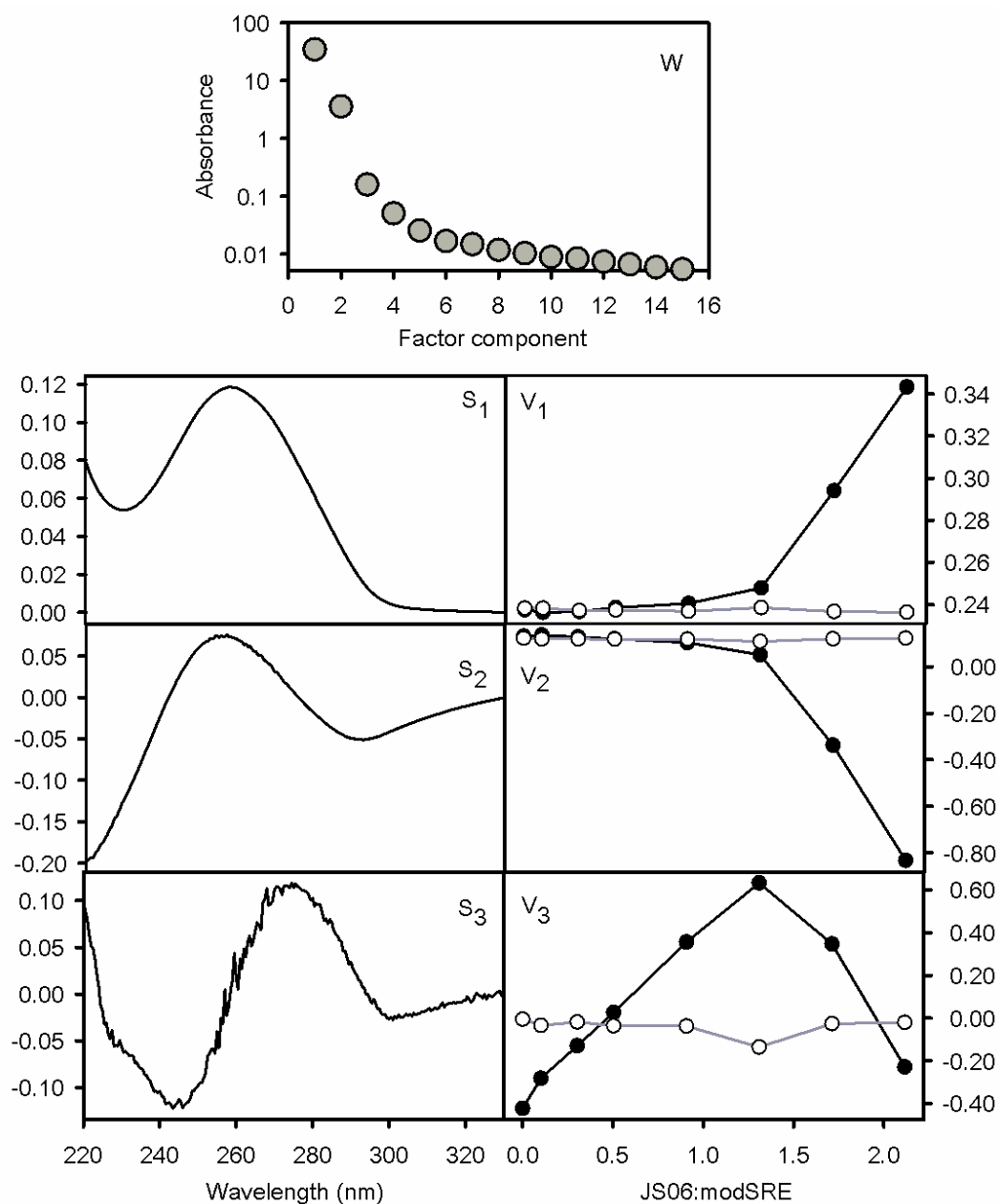


Figure 57. Factor analysis (SVD) of JS06 addition to modSRE solution monitored by UV absorption. Black circles correspond to mixed solutions in buffer, white circles to solutions where peptide/DNA interaction was prevented by high salinity (0.5 M NaCl).

To examine the interaction in closer detail, SVD was next applied only to the low peptide/DNA ratios (see Figure 58). In this case the factor dimension was two. S_1 represents the average spectral shape, S_2 shows the main spectral change. No significant change of the overall absorption intensity was observed (see coefficients V_1). Coefficients V_2 , on the other hand, show that the main spectral change S_2 is significant only in a solution without NaCl and thus can be assigned to JS06/modSRE interaction.

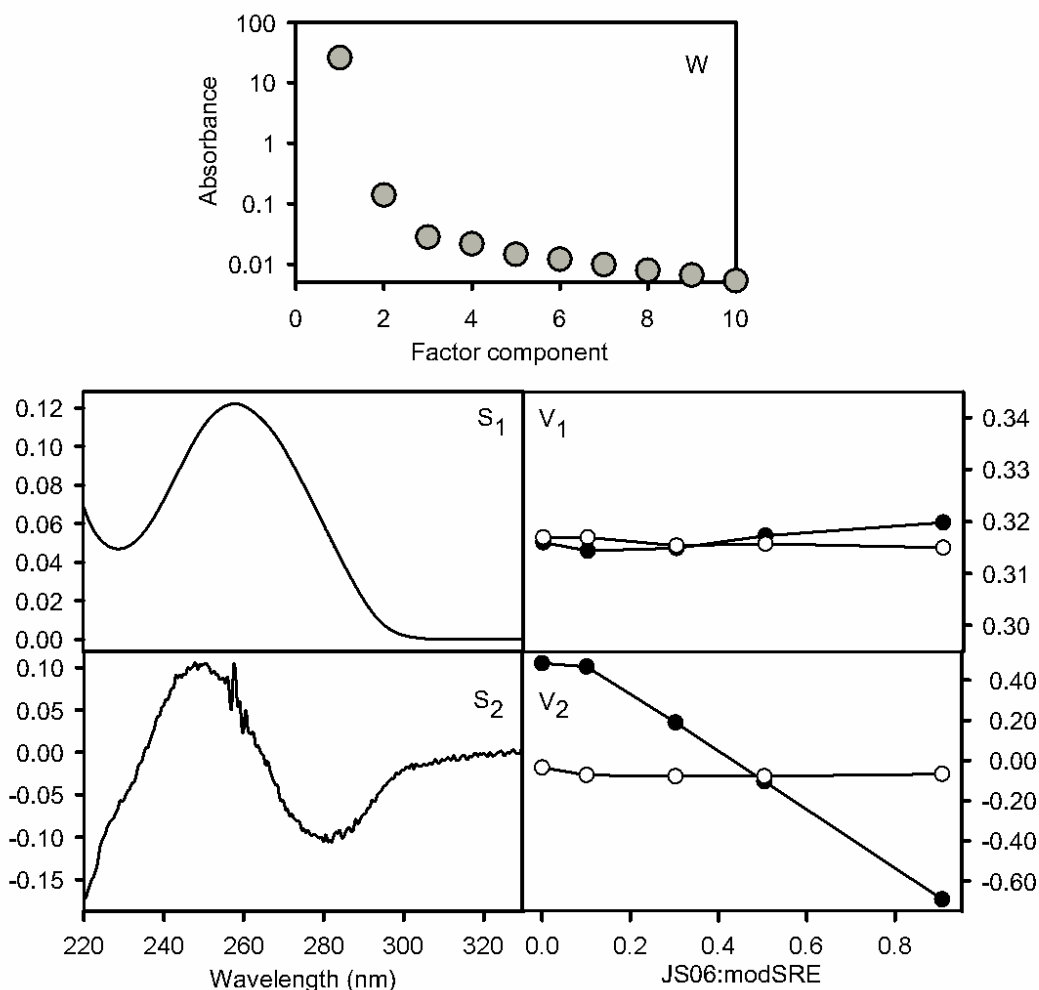


Figure 58. Factor analysis (SVD) of JS06 addition to modSRE solution monitored by UV absorption, limited for low peptide concentrations when no clear signs of precipitation were observed. Black circles correspond to mixed solutions in buffer, white circles to solutions where peptide/DNA interaction was prevented by high salinity (0.5 M NaCl).

Besides the absorption spectra described above, fluorescence spectra were also measured within the titration experiment (see Figure 59). In both reference solutions (with and without NaCl content) the addition of the JS06 oligopeptide resulted in the same increase of tyrosine emission. This confirms that the high salinity of the solution doesn't affect the peptide. Due to the inner filter effect the intensity of the JS06 oligopeptide in solution with both the modSRE oligonucleotide and NaCl was lower than in corresponding reference solution (corrected spectra are shown in Figure 60). On the other hand in the case of the solution without NaCl, the oligonucleotide caused nearly complete quenching of tyrosine fluorescence. The measured spectra represented mainly Raman spectrum of water for lower oligopeptide concentrations). Exceeding 1:1 concentration ratio of JS06:modSRE,

the precipitation occurred and the turbidity of the solutions resulted in false emission bands around 360 and 380 nm and elastically scattered excitation light below 290 nm.

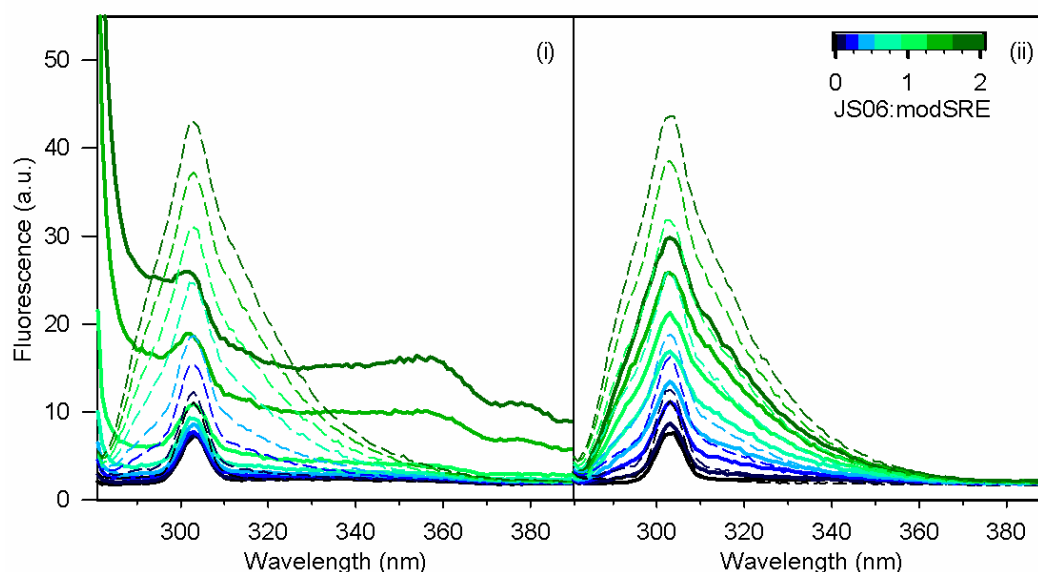


Figure 59. (i) Measured fluorescence spectra of modSRE solution during gradual addition of JS06 oligopeptide; (ii) the same experiment with the oligonucleotide solution of high salinity (0.5 M NaCl). Solid lines correspond to the oligonucleotide solution, dashed lines to the oligopeptide added to the reference solvent.

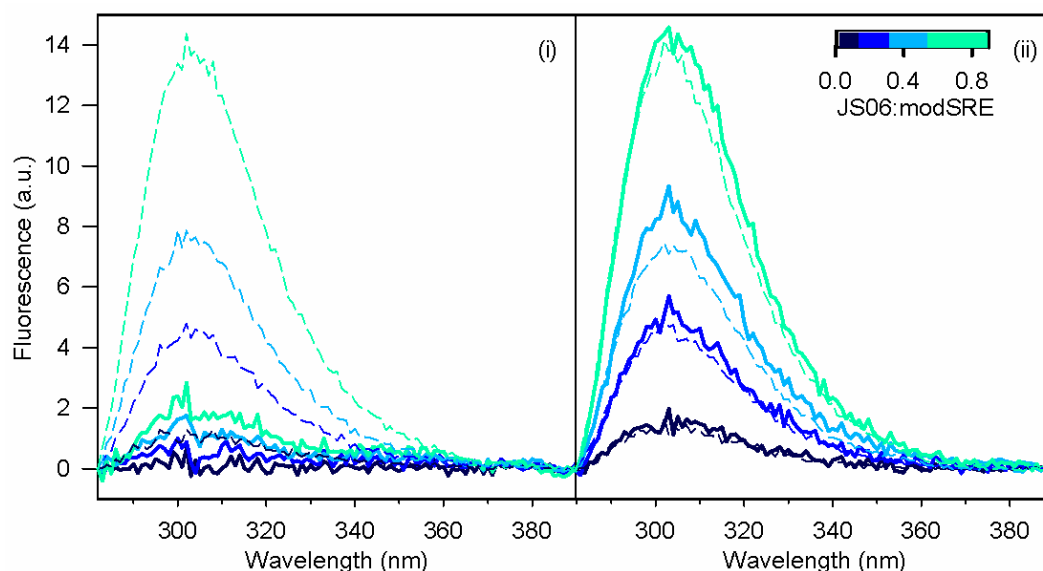


Figure 60. (i) Corrected fluorescence spectra of modSRE solution during gradual addition of JS06 oligopeptide (only spectra before precipitation). Corrections are described in chapters 3.2.1 and 4.1.1). (ii) The same experiment with the oligonucleotide solution of high salinity (0.5 M NaCl). Solid lines correspond to the oligonucleotide solution, dashed lines to the oligopeptide added to the reference solvent.

In order to determine the fluorescence fraction quenched by the interaction with DNA, all sets of corrected spectra (when no clear signs of precipitation were observed) were subjected to factor analysis (SVD) (see Figure 61). The factor dimension equals to one. Excluding turbid samples the first and only subspectrum represents the emission of tyrosine peaking at 302 nm. Absence of second dimension means that the emission spectral shape is not affected by the interaction of the two partners. Using the linear regression on coefficients V_1 it was found that $86 \pm 5 \%$ of the JS06 fluorescence is quenched by interaction with DNA in the solution without NaCl, when compared to the solution with NaCl.

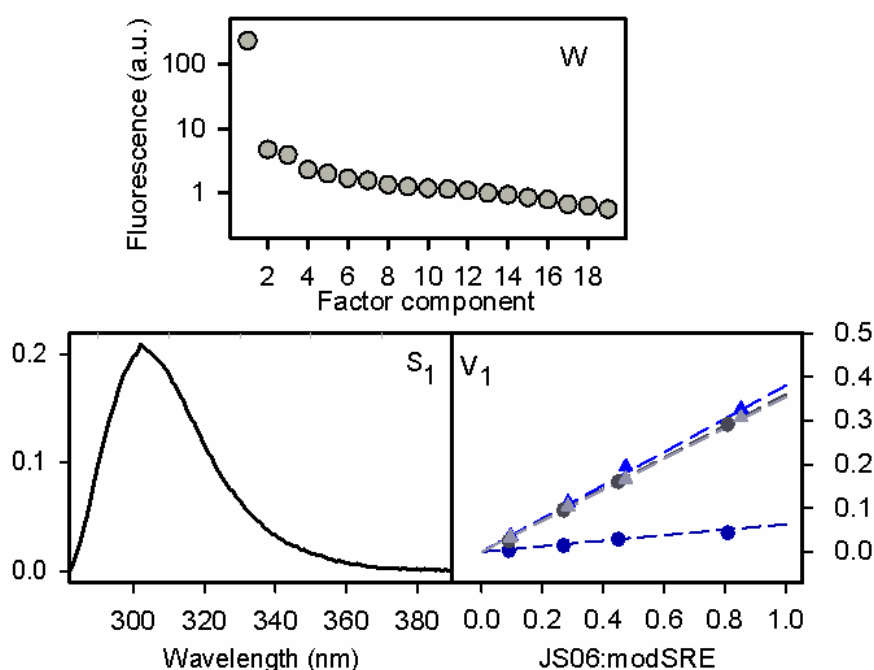


Figure 61. Factor analysis (SVD) of JS06 oligopeptide addition to modSRE sample fluorescence, limited for low peptide concentrations when no clear signs of precipitation were observed. Circles represent the samples dissolved in buffer, and triangles the samples in buffer and 0.5 M NaCl). Blue symbols represent solutions with DNA; grey symbols reference solutions without DNA.

4.5.3. Comparison of the interaction experiments

Titration analogous to the one described in chapter 4.5.1 were performed also with the JS04 and JS05 oligopeptides. Results of these experiments were very similar. Adding aliquots of DNA into a cuvette containing a known amount of model oligopeptide bearing tyrosine residue resulted in immediate aggregation of the samples. This can be explained by the ability of an oligonucleotide to bind many

oligopeptides creating a large precipitating complex. Thus the standard Stern-Volmer characterisation of fluorescence quenching mechanism (described in chapter 3.3.2) could not be applied.

On the other hand, when the oligopeptide was added to the oligonucleotide solution (chapter 4.5.2.) no such behaviour was observed. Titrations analogous to the one described in chapter 4.5.2. were also performed with oligopeptides JS05 and JS04 and different oligonucleotides (see Table 5). Results of these experiments were very similar. The addition of oligopeptide caused precipitation only when the ratio 1:1 peptide:ssDNA was exceeded (in the case of the duplex DNA the ratio 2:1 peptide:dsDNA). Probably each oligopeptide binds preferentially to unengaged oligonucleotide and form a complex which is smaller and do not form a precipitate.

Consecutive addition of oligopeptide to the oligonucleotide solution lead to increase of the tyrosine emission, but with lower quantum yield than in the solution without DNA. This is in agreement with the literature [112, 114-115] stating that the interaction of tyrosine with DNA causes quenching of its fluorescence emission.

In all cases a parallel experiment was performed using solutions with added 0.5 M NaCl. Similarly to literature [112, 114] it was observed that addition of salt to the solution hampered the quenching of tyrosine by DNA. The quantum yield of the tyrosine in the solution with and without DNA content was about the same. Na⁺ ions probably interact with the phosphate backbone of the DNA [114] preventing the peptide/DNA interaction.

Table 5. Summary of interaction experiments – decrease of tyrosine quantum yield comparing the solution with and without DNA (additions of oligopeptide to oligonucleotide solution).

oligonucleotide \ oligopeptide	JS06 (Y158)	JS05 (Y173)	JS04 (Y158, Y173)
ss modSRE	86 ± 5 %	46 ± 5 %	71 ± 6 %
ss SREfos	74 ± 5 %		
ds modSRE	65 ± 5 %		

The addition of the oligopeptides to the oligonucleotide solution can be well compared. Fitting of factor analysis (SVD) fluorescence results limited for low peptide concentrations (when no clear signs of precipitation were observed) served for determination of the fraction of the oligopeptide emission statically quenched after its binding to the oligonucleotide. Comparing the results of the various fits it can be stated that the tyrosine Y173 is quenched by $46 \pm 5 \%$ (in JS05), while Y158 by $86 \pm 5 \%$ (in JS06), by the interaction with the single stranded modSRE. According to our assumptions the fraction of quenched fluorescence of the JS04 oligopeptide bearing both tyrosines is in between of the two previous values, i.e. $71 \pm 5 \%$. Result of joint factor analysis of oligopeptide JS04-6 additions to the modSRE oligonucleotide solution is shown in Figure 62. The factor dimension equals to one. Increase of the first coefficients depends on the quenched fraction of the fluorescence already described in previous paragraph.

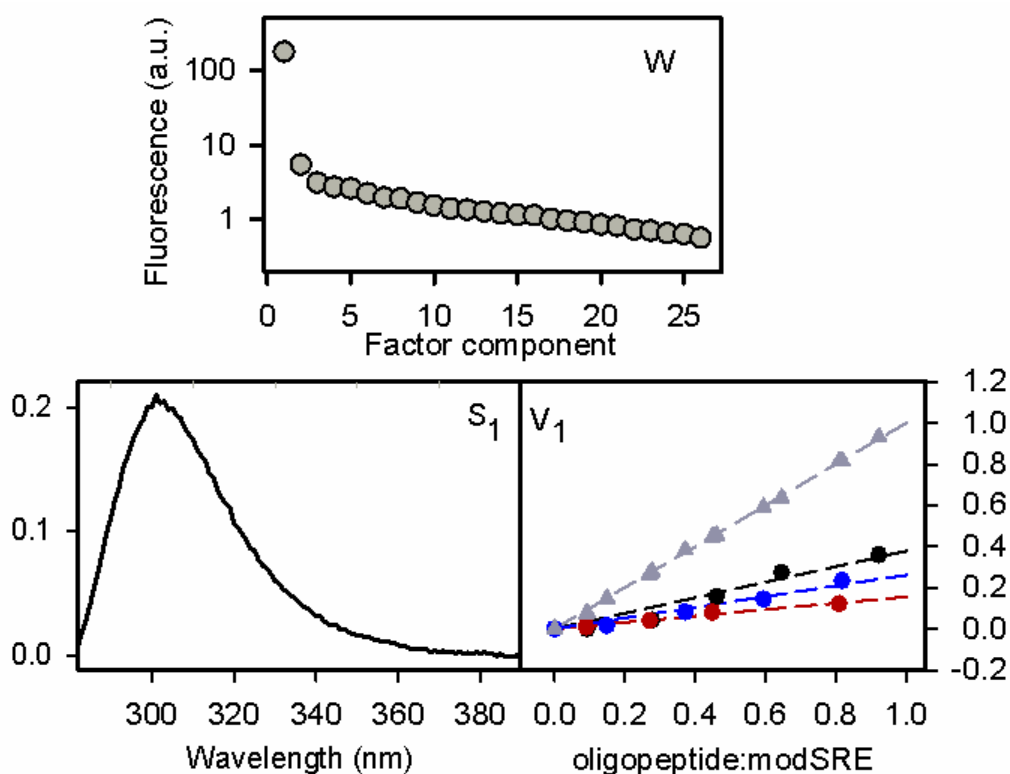


Figure 62. Factor analysis (SVD) of JS04-6 oligopeptide addition to modSRE oligonucleotide sample fluorescence limited for low peptide concentrations. All spectra were normalized according to reference solution. Circles represent samples dissolved in buffer; triangles samples in reference solution without DNA. Black symbols represent JS05; red JS06 and blue JS04 oligopeptide.

Furthermore the JS06 additions to SREfos and ds modSRE (duplex of modSRE and modSREcompl) oligonucleotides were performed. From the separate

analyses of the fluorescence spectra (Table 5) it may be deduced that modSRE quenches the fluorescence of the JS06 more effectively ($86 \pm 5 \%$) than SREfos ($74 \pm 5 \%$) and ds modSRE ($65 \pm 5 \%$).

As a result it may be stated that the MADS-box N-terminal segments possess high affinity to deoxyoligonucleotides, forming soluble complexes when the concentration ratios is optimal for 1:1 stoichiometry, but creating precipitating complexes in the case of the oligopeptide excess. No remarkable binding specificity distinguishing single and double stranded DNA was though observed. Nevertheless, a feasible way for monitoring DNA/MADS-box protein interactions was demonstrated by these pilot experiments.

5. Conclusions

The thesis was devoted to investigation of physico-chemical properties of the Human SRF MADS box in respect to its biological function. The study of the MADS box and its oligopeptide segments was performed in aqueous solution by using a wide range of spectroscopic techniques. The three tyrosine residues (Tyr158, Tyr173 and Tyr195) of the MADS box located in differently charged and differently hydrophobic amino-acid vicinities were used as spectroscopic inner probes. Accordingly a great attention was paid to their spectroscopic characterization. To distinguish their individual contributions to the MADS-box spectra and to reveal their particular physico-chemical characteristics, subtle spectral changes caused by varied environmental conditions were visualized by means of factor analysis. An approach based on a least square fit of the multi-wavelength spectroscopic pH titration data to an adequate thermodynamic model, was developed for determination of pKa constants and spectral characteristics of variously protonated tyrosine forms (published in [I]). It was revealed that the positively charged amino acids in the vicinity of the tyrosine residues Tyr158 and Tyr173 inside short MADS-box segments reduce pKa value in respect to a free tyrosine (9.0 and 9.5 versus 10.0).

The structural properties of the short MADS-box segment around Tyr173 in dependence on the tyrosine protonation state were investigated in details by Raman scattering, infrared and circular dichroism spectroscopies in combination with molecular dynamics simulations (MDS) and density functional theory calculations (published in [II]). The major spectral changes were attributed to the tyrosine deprotonation. All techniques also proved that the short oligopeptide doesn't have a stable secondary structure and exists in a state of dynamical equilibrium among several conformations mostly close to the beta turn, unordered conformation and extended structure. Nevertheless, the quantum chemical calculations of vibrational states of the most populated oligopeptide geometries (obtained by MDS) enabled to simulate Raman spectra for both tyrosine forms. Our approach seems to be generally applicable as a useful tool for study of short oligopeptides.

A thorough study of the MADS box was performed using fluorescence, UV-absorption and Raman spectroscopy, in order to disclose its behavior and basic functional properties in aqueous environment (results published in [III]). The secondary structure of the MADS box was estimated to 64–69 % of β -sheet content,

22–25 % of β -turn content and only ~2 % of α -helix content by analysis of the amide I and III bands of Raman spectra, without any remarkable sensitivity to pH changes. Using factor analysis a two-component fluorescence quenching was revealed and corresponding Stern–Volmer constants determined. Their values indicated prevailing diffusion-limited mechanism of quenching. Simultaneous fit of the results obtained by factor analyses of both UV-absorption and fluorescence pH titration data led to determination of three dissociation constants $pK_{a1} = 6.4 \pm 0.2$, $pK_{a2} = 7.3 \pm 0.2$, and $pK_{a3} = 9.6 \pm 0.6$. Critical comparison of all experiments identified the deprotonation of His193 (hydrogen bonded to Tyr195) as the transition connected with the acid-base equilibrium corresponding to pK_{a1} and that of Tyr158 as a candidate for pK_{a2} . The occurrence of two acid-basic transitions close to a neutral pH leads to a variability in possible electrostatic interactions which seem to be together with the structural flexibility advantageous for recognition and binding to the DNA target.

Attempts to monitor at lower concentrations the interaction between DNA and longer segments of the MADS box, which represented its N-terminal part or analogs with a single point mutation, were performed by UV absorption and fluorescence spectroscopies. It was found out that adding even small aliquots of deoxyoligonucleotides into $\sim 3 \times 10^{-5}$ M oligopeptide solution resulted in immediate precipitation of the sample. This was explained by a capability of deoxyoligonucleotide to bind many MADS-box oligopeptides creating a large precipitating complex. On the other hand, when the oligopeptide was added to the oligonucleotide solution no precipitation was observed (until a molecular ratio 1:1 was reached). Comparing the fluorescence spectra with those of the samples where the oligopeptide was added to a deoxyoligonucleotide solution containing 0.5 M NaCl (which prevents the interaction), it was possible to determine partial quenching of the tyrosine fluorescence. No remarkable binding specificity resolving single stranded and double stranded DNA was though observed. Nevertheless, these pilot experiments showed a feasible way for monitoring DNA/MADS-box protein interactions in future studies.

The acquired data provided a number of physico-chemical characteristics of the MADS box and its segments concerning the structural properties and protonation states. This has gained the understanding to the behaviour of the MADS box and thereby the whole MADS box family of transcription factors. Our results can be

concluded on the fact that the MADS box as an isolated protein exhibits high structural and charge variability enabling to effectively bind to DNA. Reaching the structural arrangement necessary for the recognition and binding to the specific target DNA site requires, though, additional intra- and intermolecular interactions including also the parts of transcription factors situated outside the MADS box domain. The study should therefore continue in the future by investigation of larger parts or even complete molecules of MADS-box transcription factors employing (where possible) the methodological approaches developed and proved within this doctoral work.

6. Dissemination of the thesis results

The results of the thesis were published in two articles in the following two papers available online and one article was currently submitted.

Articles:

- [I] ŘEZÁČOVÁ B., COIC Y.M., ZENTZ C., TURPIN P.Y., ŠTĚPÁNEK J. Spectroscopic Determination of pKa Constants of MADS Box Segments. *Spectrosc. Int. J.* 2012, **27**, 455-461. ISSN: 0712-4813.
Published also as a book chapter in: MARQUES M.P., BATISTA DE CARVALHO L.A.E., HARIS P.I. *Spectroscopy of Biological Molecules*, Amsterdam: IOS Press BV, 2013. ISBN 978-1-61499-183-0.
- [II] PROFANTOVÁ B., PROFANT V., ZÍMA V., KOPECKÝ JR. V., BEDNÁROVÁ L., ZENTZ C., BAUMRUK V., TURPIN P.Y., ŠTĚPÁNEK J. Protonation effect of tyrosine in a segment of the SRF transcription factor: A combined optical spectroscopy, molecular dynamics, and density functional theory calculation study. *J. Phys. Chem. B.* 2013, **117**, 16086-16095. ISSN: 1520-6106
- [III] PROFANTOVÁ B., COIČ Y.M., PROFANT V., ŠTĚPÁNEK J., KOPECKÝ V. JR., TURPIN P.Y., ALPERT B., ZENTZ C. A role of histidine in the MADS Box from Human SRF revealed by tyrosine perturbation. *Biochemistry*, 2014. (submitted).

Conference contributions:

1. PROFANTOVÁ B., ZENTZ C., KOPECKÝ V.JR., TURPIN P.Y., ŠTĚPÁNEK J., poster: "Spectroscopic study of MADS-box segments and their interaction with DNA." *15th European Conference on the Spectroscopy of Biological Molecules (15th ECSBM)*, Oxford, United Kingdom, 25-30.8.2013.
2. PROFANTOVÁ-ŘEZÁČOVÁ B., ZENTZ C., TURPIN P.Y., KRUGLIK S., ŠTĚPÁNEK J., oral contribution: „Boîte MADS et ses segments courts:

- étude physicochimique.“ *Journées de Rentrée ED iViv*, Paris, France, 13-14.11.2012.
3. PROFANTOVÁ-ŘEZÁČOVÁ B., PROFANT V., ZÍMA V., ZENTZ C., KRUGLIK S., BEDNÁROVÁ L., TURPIN P.Y., ŠTĚPÁNEK J., poster: „Raman spectroscopy of a MADS box segment: experiments and calculations.“ *23rd International Conference on Raman Spectroscopy (ICORS 2012)*, Bangalore, India, 12-17.8.2012.
 4. ŘEZÁČOVÁ B., PROFANT V., ZENTZ C., COÏCC Y.M., KRUGLIK, S., TURPIN P.Y., ŠTĚPÁNEK J., poster: „Spectroscopic study of the MADS box.“ *X Discussions in Structural Molecular Biology*, Nové Hradky, Czech Republic, 22-24.3.2012.
 5. ŘEZÁČOVÁ B., COÏC Y.M., ZENTZ C., TURPIN P.Y., ŠTĚPÁNEK J., poster: “Investigation of MADS box intrinsic fluorophores.” *Journées de Rentrée ED iViv*, Paris, France, 25-26.10.2011.
 6. ŘEZÁČOVÁ B., COÏC Y.M., ZENTZ C., TURPIN P.Y., ŠTĚPÁNEK J., poster: “Investigation of MADS box intrinsic fluorophores.” *12th Conference on Methods and Applications of Fluorescence Spectroscopy, Imaging and Probes (MAF12)*, Strasbourg, France, 11-14.9.2011.
 7. ŘEZÁČOVÁ B., ZENTZ C., TURPIN P.Y., KOPECKÝ V., ŠTĚPÁNEK J., poster: “Spectroscopic investigation of the MADS box.” *14th European Conference on the Spectroscopy of Biological Molecules (14th ECSBM)*, Coimbra, Portugal, 28.8-3.9.2011.
 8. ŘEZÁČOVÁ B., ZENTZ C., TURPIN P.Y., ŠTĚPÁNEK J., oral contribution: “Spectroscopic study of MADS box and its interaction with DNA.” *30th European Congress on Molecular Spectroscopy (30th EUCMOS)*, Florence, Italy, 29.8-3.9.2010.
 9. ŘEZÁČOVÁ B., ZENTZ C., TURPIN P.Y., ŠTĚPÁNEK J., oral contribution: “Spectroscopic study of MADS box and its interaction with DNA.” *Week of Doctoral Students 2010 (WDS 2010)*, Prague, Czech Republic, 1-4.6.2010.

7. Bibliography

- [1] ALBERTS B., JOHNSON A., LEWIS J., RAFF M., ROBERTS K., WALTER P. *Molecular Biology of the Cell*. 4th ed. New York: Garland Science, 2002. ISBN 0-8153-3218-1.
- [2] BERG J.M., TYMOCZKO J.L., STRYER L. *Biochemistry*. 5th ed. New York: W H Freeman, 2002. ISBN 0-7167-3051-0. <http://www.ncbi.nlm.nih.gov/books/NBK21154/> (accessed 15.10.2013).
- [3] NELSON D.L., COX M.M., LEHNINGER A.L. *Lehninger Principles of Biochemistry*. 4th ed. New York: W. H. Freeman, 2005. ISBN 0-7167-4339-6.
- [4] LODISH H., BERK A., ZIPURSKY S.L., MATSUDAIRA P., BALTIMORE D., DARNELL J. *Molecular Cell Biology*. 4th ed. New York: W. H. Freeman, 2000. ISBN 0-7167-3136-3. <http://www.ncbi.nlm.nih.gov/books/NBK21475/> (accessed 11.10.2013).
- [5] STRACHAN T., READ A.P. *Human Molecular Genetics*. 2nd ed. New York: Wiley-Liss, 1999. ISBN 1-85996-202-5. <http://www.ncbi.nlm.nih.gov/books/NBK7580/> (accessed 11.10.2013).
- [6] BRIVANLOU A.H., DARNELL J.E. Transcription - Signal transduction and the control of gene expression. *Science*. 2002, **295** (5556), 813-818. ISSN 0036-8075.
- [7.] WINGENDER E., SCHOEPS T., DONITZ J. TFClass: an expandable hierarchical classification of human transcription factors. *Nucleic Acids Res*. 2013, **41** (D1), D165-D170. ISSN 0305-1048.
- [8.] MATYS V., KEL-MARGOULIS O.V., FRICKE E., LIEBICH I., LAND S., BARRE-DIRRIE A., REUTER I., CHEKMENEV D., KRULL M., HORNISCHER K., VOSS N., STEGMAIER P., LEWICKI-POTAPOV B., SAXEL H., KEL A.E., WINGENDER E. TRANSFAC (R) and its module TRANSCompel (R): transcriptional gene regulation in eukaryotes. *Nucleic Acids Res*. 2006, **34**, D108-D110. ISSN 0305-1048.
- [9] SHORE P., SHARROCKS A.D. The MADS-box family of transcription factors. *Eur. J. Biochem*. 1995, **229** (1), 1-13. ISSN 0014-2956.

- [10] FORNARA F., MARZIANI G., MIZZI L., KATER M., COLOMBO L. MADS-box genes controlling flower development in rice. *Plant Biol.* 2003, **5** (1), 16-22. ISSN 1435-8603.
- [11] ADAMCZYK B.J., FERNANDEZ D.E. MIKC* MADS Domain Heterodimers Are Required for Pollen Maturation and Tube Growth in Arabidopsis. *Plant Physiol.* 2009, **149** (4), 1713-1723. ISSN 0032-0889.
- [12] ZHENG Y.M., REN N., WANG H., STROMBERG A.J., PERRY S.E. Global Identification of Targets of the Arabidopsis MADS Domain Protein AGAMOUS-Like15. *Plant Cell.* 2009, **21** (9), 2563-2577. ISSN 1040-4651.
- [13] SHU Y.J., YU D.S., WANG D., GUO D.L., GUO C.H. Genome-wide survey and expression analysis of the MADS-box gene family in soybean. *Mol. Biol. Rep.* 2013, **40** (6), 3901-3911. ISSN 0301-4851.
- [14] SUN Q., CHEN G., STREB J.W., LONG X.C., YANG Y.M., STOECKERT C.J., MIANO J.M. Defining the mammalian CArGome. *Genome Res.* 2006, **16** (2), 197-207. ISSN 1088-9051.
- [15] POTTHOFF M.J., OLSON E.N. MEF2: a central regulator of diverse developmental programs. *Development.* 2007, **134** (23), 4131-4140. ISSN 0950-1991.
- [16] FLAVELL S.W., KIM T.K., GRAY J.M., HARMIN D.A., HEMBERG M., HONG E.J., MARKENSCOFF-PAPADIMITRIOU E., BEAR D.M., GREENBERG M.E. Genome-Wide Analysis of MEF2 Transcriptional Program Reveals Synaptic Target Genes and Neuronal Activity-Dependent Polyadenylation Site Selection. *Neuron.* 2008, **60** (6), 1022-1038. ISSN 0896-6273.
- [17] MCDONALD O.G., WAMHOFF B.R., HOOFNAGLE M.H., OWENS G.K. Control of SRF binding to CArG box chromatin regulates smooth muscle gene expression in vivo. *J. Clin. Invest.* 2006, **116** (1), 36-48. ISSN 0021-9738.
- [18] THEISSEN G., KIM J.T., SAEDLER H. Classification and phylogeny of the MADS-box multigene family suggest defined roles of MADS-box gene subfamilies in the morphological evolution of eukaryotes. *J. Mol. Evol.* 1996, **43** (5), 484-516. ISSN 0022-2844.
- [19] MEAD J., BRUNING A.R., GILL M.K., STEINER A.M., ACTON T.B., VERSHON A.K. Interactions of the Mcm1 MAIDS box protein with cofactors that

regulate mating in yeast. *Mol. Cell. Biol.* 2002, **22** (13), 4607-4621. ISSN 0270-7306.

[20] PASSMORE S., ELBLE R., TYE B.K. A protein involved in minichromosome maintenance in yeast binds a transcriptional enhancer conserved in eukaryotes. *Genes Dev.* 1989, **3** (7), 921-935. ISSN 0890-9369.

[21] YANOFSKY M.F., MA H., BOWMAN J.L., DREWS G.N., FELDMANN K.A., MEYEROWITZ E.M. The protein encoded by the Arabidopsis homeotic gene *agamous* resembles transcription factors. *Nature.* 1990, **346** (6279), 35-39. ISSN 0028-0836.

[22] SOMMER H., BELTRAN J.P., HUIJSER P., PAPE H., LONNIG W.E., SAEDLER H., SCHWARZSOMMER Z. *Deficiens*, a homeotic gene involved in the control of flower morphogenesis in *Antirrhinum majus*: the protein shows homology to transcription factors. *Embo J.* 1990, **9** (3), 605-613. ISSN 0261-4189.

[23] NORMAN C., RUNSWICK M., POLLOCK R., TREISMAN R. Isolation and properties of cDNA clones encoding SRF, a transcription factor that binds to the c-fos serum response element. *Cell.* 1988, **55** (6), 989-1003. ISSN 0092-8674.

[24] BECKER A., THEISSEN G. The major clades of MADS-box genes and their role in the development and evolution of flowering plants. *Mol. Phylogenet. Evol.* 2003, **29** (3), 464-489. ISSN 1055-7903.

[25] MUNSTER T., PAHNKE J., DIROSA A., KIM J.T., MARTIN W., SAEDLER H., THEISSEN G. Floral homeotic genes were recruited from homologous MADS-box genes preexisting in the common ancestor of ferns and seed plants. *Proc. Natl. Acad. Sci. U. S. A.* 1997, **94** (6), 2415-2420. ISSN 0027-8424.

[26] PELLEGRINI L., SONG T., RICHMOND T.J. Structure of Serum Response Factor Core Bound to DNA. *Nature.* 1995, **376** (6540), 490-498. ISSN 0028-0836.

[27] HASSLER M., RICHMOND T.J. The B-box dominates SAP-1-SRF interactions in the structure of the ternary complex. *Embo J.* 2001, **20** (12), 3018-3028. ISSN 0261-4189.

[28] TAN S., RICHMOND T.J. Crystal structure of the yeast MAT alpha 2/MCM1/DNA ternary complex. *Nature.* 1998, **391** (6668), 660-666. ISSN 0028-0836.

- [29] SANTELLI E., RICHMOND T.J. Crystal structure of MEF2A core bound to DNA at 1.5 angstrom resolution. *J. Mol. Biol.* 2000, **297** (2), 437-449. ISSN 0022-2836.
- [30] HUANG K., LOUIS J.M., DONALDSON L., LIM F.L., SHARROCKS A.D., CLORE G.M. Solution structure of the MEF2A-DNA complex: structural basis for the modulation of DNA bending and specificity by MADS-box transcription factors. *Embo J.* 2000, **19** (11), 2615-2628. ISSN 0261-4189.
- [31] WU W.W., SHEN X., TAO S.H. Characteristics of the CARG-SRF binding context in mammalian genomes. *Mamm. Genome.* 2010, **21** (1-2), 104-113. ISSN 0938-8990.
- [32] GOSSETT L.A., KELVIN D.J., STERNBERG E.A., OLSON E.N. A New Myocyte-Specific Enhancer-Binding Factor That Recognizes a Conserved Element Associated with Multiple Muscle-Specific Genes. *Mol. Cell. Biol.* 1989, **9** (11), 5022-5033. ISSN 0270-7306.
- [33] SCHROTER H., MUELLER C.G.F., MEESE K., NORDHEIM A. Synergism In Ternary Complex-Formation between the Dimeric Glycoprotein P67SRF, Polypeptide P62TCF and the C-fos Serum Response Element. *Embo J.* 1990, **9** (4), 1123-1130. ISSN 0261-4189.
- [34] PRIMIG M., WINKLER H., AMMERER G. The DNA-Binding and Oligomerization Domain of MCM1 is Sufficient for its Interaction with other Regulatory Proteins. *Embo J.* 1991, **10** (13), 4209-4218. ISSN 0261-4189.
- [35] MOLKENTIN J.D., OLSON E.N. Combinatorial control of muscle development by basic helix-loop-helix and MADS-box transcription factors. *Proc. Natl. Acad. Sci. U. S. A.* 1996, **93** (18), 9366-9373. ISSN 0027-8424.
- [36] LEATHERWOOD J., FUTCHERT B. King of the Castle: Competition between Repressors and Activators on the Mcm1 Platform. *Mol. Cell.* 2010, **38** (1), 1-2. ISSN 1097-2765.
- [37] PRAMILA T., MILES S., GUHATHAKURTA D., JEMIOLO D., BREEDEN L.L. Conserved homeodomain proteins interact with MADS box protein Mcm1 to restrict ECB-dependent transcription to the M/G1 phase of the cell cycle. *Genes Dev.* 2002, **16** (23), 3034-3045. ISSN 0890-9369.
- [38] DARIEVA Z., CLANCY A., BULMER R., WILLIAMS E., PIC-TAYLOR A., MORGAN B.A., SHARROCKS A.D. A Competitive Transcription Factor

Binding Mechanism Determines the Timing of Late Cell Cycle-Dependent Gene Expression. *Mol. Cell.* 2010, **38** (1), 29-40. ISSN 1097-2765.

[39] SENGUPTA P., COCHRAN B.H. MAT alpha 1 can mediate gene activation by a-mating factor. *Genes Dev.* 1991, **5** (10), 1924-1934. ISSN 0890-9369.

[40] OEHLLEN L., MCKINNEY J.D., CROSS F.R. Ste12 and Mcm1 regulate cell cycle-dependent transcription of FAR1. *Mol. Cell. Biol.* 1996, **16** (6), 2830-2837. ISSN 0270-7306.

[41] EL BAKKOURY M., DUBOIS E., MESSENGUY F. Recruitment of the yeast MADS-box proteins, ArgRI and Mcm1 by the pleiotropic factor ArgRIII is required for their stability. *Mol. Microbiol.* 2000, **35** (1), 15-31. ISSN 0950-382X.

[42] THEISSEN G., BECKER A., DI ROSA A., KANNO A., KIM J.T., MUNSTER T., WINTER K.U., SAEDLER H. A short history of MADS-box genes in plants. *Plant Mol.Biol.* 2000, **42** (1), 115-149. ISSN 0167-4412.

[43] SMACZNIAK C., IMMINK R.G.H., ANGENENT G.C., KAUFMANN K. Developmental and evolutionary diversity of plant MADS-domain factors: insights from recent studies. *Development.* 2012, **139** (17), 3081-3098. ISSN 0950-1991.

[44] WEIGEL D., MEYEROWITZ E.M. The ABCs of Floral Homeotic Genes *Cell.* 1994, **78** (2), 203-209. ISSN 0092-8674.

[45] GRAMZOW L., THEISSEN G. A hitchhiker's guide to the MADS world of plants. *Genome Biol.* 2010, **11** (6). ISSN 1474-7596.

[46] GREENBERG M.E., SIEGFRIED Z., ZIFF E.B. Mutation of the c-fos gene dyad symmetry element inhibits serum inducibility of transcription in vivo and the nuclear regulatory factor binding in vitro. *Mol. Cell. Biol.* 1987, **7** (3), 1217-1225. ISSN 0270-7306.

[47] BOXER L.M., PRYWES R., ROEDER R.G., KEDES L. The sarcomeric actin CArG-binding factor is indistinguishable from the c-fos serum response factor. *Mol. Cell. Biol.* 1989, **9** (2), 515-522. ISSN 0270-7306.

[48] CHEN C.Y., SCHWARTZ R.J. Recruitment of the tinman homolog Nkx-2.5 by serum response factor activates cardiac alpha-actin gene transcription. *Mol. Cell. Biol.* 1996, **16** (11), 6372-6384. ISSN 0270-7306.

[49] BELAGULI N.S., SEPULVEDA J.L., NIGAM V., CHARRON F., NEMER M., SCHWARTZ R.J. Cardiac tissue enriched factors serum response factor and

GATA-4 are mutual coregulators. *Mol. Cell. Biol.* 2000, **20** (20), 7550-7558. ISSN 0270-7306.

[50] BELAGULI N.S., SCHILDMEYER L.A., SCHWARTZ R.J. Organization and myogenic restricted expression of the murine serum response factor gene - A role for autoregulation. *J. Biol. Chem.* 1997, **272** (29), 18222-18231. ISSN 0021-9258.

[51] HILL C.S., TREISMAN R. Transcriptional Regulation by Extracellular signals: Mechanisms and Specificity. *Cell.* 1995, **80** (2), 199-211. ISSN 0092-8674.

[52] BLACK B.L., OLSON E.N. Transcriptional control of muscle development by myocyte enhancer factor-2 (MEF2) proteins. *Annu. Rev. Cell Dev. Biol.* 1998, **14**, 167-196. ISSN 1081-0706.

[53] MESSENGUY F., DUBOIS E. Role of MADS box proteins and their cofactors in combinatorial control of gene expression and cell development. *Gene.* 2003, **316**, 1-21. ISSN 0378-1119.

[54] LIN Q., SCHWARZ J., BUCANA C., OLSON E.N. Control of mouse cardiac morphogenesis and myogenesis by transcription factor MEF2C. *Science.* 1997, **276** (5317), 1404-1407. ISSN 0036-8075.

[55] LILLY B., ZHAO B., RANGANAYAKULU G., PATERSON B.M., SCHULZ R.A., OLSON E.N. Requirement of MADS domain transcription factor D-MEF2 for muscle formation in *Drosophila*. *Science.* 1995, **267** (5198), 688-693. ISSN 0036-8075.

[56] TREISMAN R. Identification and purification of a polypeptide that binds to the c-fos serum response element. *Embo J.* 1987, **6** (9), 2711-2717. ISSN 0261-4189.

[57] MIANO J.M., LONG X.C., FUJIWARA K. Serum response factor: master regulator of the actin cytoskeleton and contractile apparatus. *Am. J. Physiol.-Cell Physiol.* 2007, **292** (1), C70-C81. ISSN 0363-6143.

[58] POSERN G., TREISMAN R. Actin' together: serum response factor, its cofactors and the link to signal transduction. *Trends Cell Biol.* 2006, **16** (11), 588-596. ISSN 0962-8924.

[59] MUELLER C.G.F., NORDHEIM A. A protein domain conserved between yeast MCM1 and human SRF directs ternary complex formation. *Embo J.* 1991, **10** (13), 4219-4229. ISSN 0261-4189.

- [60] MINTY A., KEDES L. Upstream Regions of the Human Cardiac Actin Gene That Modulate Its Transcription in Muscle Cells: Presence of an Evolutionarily Conserved Repeated Motif. *Mol. Cell. Biol.* 1986, **6** (6), 2125-2136. ISSN 0270-7306.
- [61] HUMPHREY W., DALKE A., SCHULTEN K. VMD: Visual molecular dynamics. *J. Mol. Graph.* 1996, **14** (1), 33-38. ISSN 1093-3263.
- [62] STEPANEK J., VINCENT M., TURPIN P.Y., PAULIN D., FERMANDJIAN S., ALPERT B., ZENTZ C. C→G base mutations in the CArG box of c-fos serum response element alter its bending flexibility. Consequences for core-SRF recognition. *FEBS J.* 2007, **274**, 2333-2348.
- [63] HOPP T.P., WOODS K.R. Prediction of protein antigenic determinants from amino acid sequences. *Proc. Natl. Acad. Sci. USA* 1981, **78**, 3824–3828. ISSN: 0027-8424.
- [64] ROSS J. B. A., LAWS W.R., ROUSSLANG K.W., WYSSBROD H.R., *Topics in Fluorescence Spectroscopy: Tyrosine Fluorescence and Phosphorescence from Proteins and Polypeptides*, E Lakowicz, Springer, **vol. 3**, 2002, 1-64. ISBN 978-0-306-47059-2.
- [65] PIMENTEL G. C. Hydrogen bonding and electronic transitions: The role of the Franck–Condon principle. *J. Am. Chem. Soc.* 1957, **79**, 3323–3326. ISSN 0002-7863.
- [66] BREALEY G. J., KASHA M. The role of hydrogen bonding in the blue-shift phenomenon. *J. Am. Chem. Soc.* 1955, **77**, 4462–4468. ISSN: 0002-7863.
- [67] CHIGNELL D. A., GRATZER W. B. Solvent effects on aromatic chromophores and their relation to ultraviolet difference spectra of proteins, *J. Phys. Chem.* 1968, **72**, 2934–2941. ISSN 0022-3654.
- [68] DU H., FUH R. A., LI J., CORKAN A., LINDSEY J. S. PhotochemCAD: A computer-aided design and research tool in photochemistry. *Photochem. Photobiol.* 1998, **68**, 141-142.
- [69] RAYNER D.M., KRAJCARSKI D.T., SZABO A.G., Excited-state acid–base equilibrium of tyrosine, *Can. J. Chem.* 1978, **56**, 1238–1245. ISSN 0008-4042.
- [70] TSUBOI M., EZAKI Y., AIDA M., SUZUKI M., YIMIT A., USHIZAWA, K.; UEDA, T. Raman Scattering Tensors of Tyrosine. *Biospectroscopy.* 1998, **4**, 61-71. ISSN: 1075-4261.

- [71] TUMA R. Raman Spectroscopy of Proteins: from Peptides to Large Assemblies. *J. Raman Spectrosc.* 2005, **36**, 307-319. ISSN: 0377-0486
- [72] LUDWIG M., ASHER S. A. Ultraviolet Resonance Raman Excitation Profiles of Tyrosine: Dependence of Raman Cross Sections on Excited-State Intermediates. *J. Am. Chem. Soc.* 1988, **110**, 1005-1011. ISSN: 0002-7863
- [73] WILSON E. B. JR. The Normal Modes and Frequencies of Vibration of the Regular Plane Hexagon Model of the Benzene Molecule. *Phys. Rev.* 1934, **45**, 706-714.
- [74] LEE H.I., KIM M.S., SUH S.W. Raman-spectroscopy of L-Phenylalanine, L-tyrosine, and their Peptides absorbed on silver surface. *Bull. Korean Chem. Soc.* 1988, **9**, 218-223. ISSN: 0253-2964.
- [75] SIAMWIZA M. N., LORD R. C., CHEN M. C., TAKAMATSU T. , HARADA I., MATSUURA H., SHIMANOUCI T. Interpretation of the Doublet at 850 and 830 cm^{-1} in the Raman Spectra of Tyrosyl Residues in Proteins and Certain Model Compounds. *Biochemistry.* 1975, **14**, 4870-4876. ISSN: 0006-2960.
- [76] NEMECEK D., STEPANEK J., THOMAS G.J.JR. Raman Spectroscopy of Proteins and Nucleoproteins *Curr. Protoc. Protein Sci.* 2013, 71, 17.8.1-17.8.52.
- [77] PALAFOX M.A. Scaling Factors for the Prediction of Vibrational Spectra. I. Benzene Molecule. *Int. J. Quant. Chem.* 2000, **77**, 661-684. ISSN: 0020-7608.
- [78] REZACOVA B. Diploma thesis: Strukturní flexibilita regulačního segmentu DNA, 2009.
- [79] KIBBE W.A. OligoCalc: an online oligonucleotide properties calculator. *Nucleic Acids. Res.* 2007, **35**, W43-W46. ISSN: 0305-1048. <http://www.basic.northwestern.edu/biotools/oligocalc.html> (accessed 28.3.2012).
- [80] TATAUROV A.V., YOU Y., OWCZARZY R. Predicting ultraviolet spectrum of single stranded and double stranded deoxyribonucleic acids, *Biophys. Chem.* 2008, **133**, 66-70. ISSN: 0301-4622.
- [81] LAKOWICZ J.R. *Principles of fluorescence spectroscopy.* 3rd ed. New York: Springer, 2006. ISBN 0-387-31278-1.
- [82] PALACKY J., MOJZES P., BOK J. SVD-Based Method for Intensity Normalization, Background Correction and Solvent Subtraction in Raman Spectroscopy Exploiting the Properties of Water Stretching Vibrations. *J. Raman Spectrosc.* 2011, **42**, 1528-1539. ISSN: 0377-0486.

- [83] DOUSSEAU F., THERRIEN M., PEZOLET M. On the Spectral Subtraction of Water from the FT-IR Spectra of Aqueous Solutions of Proteins. *Appl. Spectrosc.* 1989, **43**, 538-542. ISSN: 0003-7028.
- [84] ANDEL J. *Matematická statistika*, 2nd ed., Praha: SNTL, 1985.
- [85] MALINOWSKI E.R. *Factor Analysis in Chemistry*, 3rd ed. New York: Wiley-Interscience, 2002. ISBN 0471134791.
- [86] SELA M., KATCHALSKI E. Spectrophotometric Titration of Alpha-Amino Acid Copolymers Containing Tyrosine. *J. Am. Chem. Soc.* 1956, **78**, 3986-3989. ISSN: 0002-7863.
- [87] DRAKE A.F., SILIGARDI G., GIBBONS W.A. Reassessment of the Electronic Circular-Dichroism Criteria for Random Coil Conformations of Poly(L-Lysine) and the Implications for Protein Folding and Denaturation Studies. *Biophys. Chem.* 1988, **31**, 143-146. ISSN: 0301-4622.
- [88] GOKCE I., WOODY R.W., ANDERLUH G., LAKEY J.H. Single Peptide Bonds Exhibit Poly(pro)II ("Random Coil") Circular Dichroism Spectra. *J. Am. Chem. Soc.* 2005, **127**, 9700-9701. ISSN: 0002-7863.
- [89] SIMMONS N.S., GLAZER A.N. An Analysis of the Tyrosine Circular Dichroism Bands in Ribonuclease. *J. Am. Chem. Soc.* 1967, **89**, 5040-2. ISSN: 0002-7863.
- [90] TENSMEYER L.G., KAUFFMAN E.W. Protein Structure as Revealed by Nonresonance Raman Spectroscopy. In *Spectroscopic methods for determining protein structure in solution*, New York: VCH Publishers, 1996, 69-95.
- [91] PELTON J.T., MCLEAN L.R. Spectroscopic Methods for Analysis of Protein Secondary Structure. *Anal. Biochem.* 2000, **277**, 167-176. ISSN: 0003-2697.
- [92] GARNIER J., GIBRAT J.F., ROBSON B. GOR Method for Predicting Protein Secondary Structure from Amino Acid Sequence. *Methods Enzymol.* 1996, **266**, 540-553. ISSN: 0076-6879.
- [93] CHOU P.Y., FASMAN G.D. Conformational Parameters for Amino Acids in Helical, β -Sheet, and Random Coil Regions Calculated from Proteins. *Biochemistry* 1974, **13**, 211-222. ISSN: 0006-2960.
- [94] BARTH A. Infrared Spectroscopy of Proteins. *Biochim. Biophys. Acta-Bioenerg.* 2007, **1767**, 1073-1101. ISSN 0005-2728.

- [95] BARTH A. The Infrared Absorption of Amino Acid Side Chains. *Prog. Biophys. Mol. Biol.* 2000, **74**, 141-173. ISSN: 0079-6107.
- [96] RAJKUMAR B.J.M., RAMAKRISHNAN V. Infrared and laser Raman studies of l-phenylalanine l-phenylalaninium perchlorate and bis(dl-phenylalaninium) sulphate monohydrate, *Spectrochim. Acta A.* 2002, **58**, 1923-1934. ISSN 1386-1425.
- [97] JOHNSON C.R., LUDWIG M., ASHER S.A. Ultraviolet Resonance Raman Characterization of Photochemical Transients of Phenol, Tyrosine, and Tryptophan. *J. Am. Chem. Soc.* 1986, **108**, 905-912. ISSN: 0002-7863.
- [98] CHAN W.C., WHITE P.D., *Fmoc solid phase peptide synthesis: A practical approach*, London: Oxford University Press, 2000. ISBN 0199637245.
- [99] HARADA I., MIURA T., TAKEUCHI H. Origin of the doublet at 1360 and 1340 cm^{-1} in the Raman spectra of tryptophan and related compounds. *Spectrochim. Acta A.* 1986, **42**, 307-312. ISSN: 0584-8539.
- [100] MIURA T., TAKEUCHI H., HARADA I. Tryptophan Raman bands sensitive to hydrogen-bonding and side-chain conformation. *J. Raman Spectrosc.* 1989, **20**, 667-671. ISSN: 0377-0486.
- [101] MAITI N, THOMAS S., JACOB J.A., CHADHA R., MUKHERJEE T., KAPOOR S. DFT and surface-enhanced Raman scattering study of tryptophan-silver komplex. *J. Colloid Interface Sci.* 2012, **380**, 141-149. ISSN: 0021-9797.
- [102] HERNANDEZ B, PFLUGER F., KRUGLIK S.G., GHOMI M. TI Characteristic Raman lines of phenylalanine analyzed by a multiconformational approach. *J. Raman Spectrosc.* 2013, **44**, 827-833. ISSN: 0377-0486.
- [103] DIETZE E.C., WANG R.W., LU A.Y.H., ATKINS W.M. Ligand effects on the fluorescence properties of tyrosine-9 in alpha 1-1 glutathione S-transferase. *Biochemistry* 1996, **35**, 6745-6753. ISSN: 0006-2960.
- [104] FERNANDEZ-RECIO J., ROMERO A., SANCHO J. Energetics of a hydrogen bond (charged and neutral) and of a cation-pi interaction in apoflavodoxin. *J. Mol. Biol.* 290, 1999, 319-330. ISSN: 0022-2836.
- [105] HOMER R.B., ALLSOPP S.R. An investigation of the electronic and steric environment of tyrosyl residues in ribonuclease a and Erwinia Caroto-voral-asparaginase through fluorescence quenching by caesium, iodide and phosphate. *Biochim. Biophys. Acta.* 1976, **434**, 297-310.

- [106] MATTHEWS C.R., WESTMORELAND D.G. Nuclear magnetic resonance studies of residual structure in thermally unfolded ribonuclease A. *Biochemistry* 1975, **14**, 4532-4538. ISSN: 0006-2960.
- [107] ANDERSON D.E., BECKTEL W.J., DAHLQUIST F.W. pH-induced denaturation of proteins: a single salt bridge contributes 3-5 kcal/mol to the free energy of folding of T4 lysozyme. *Biochemistry* 1990, **29**, 2403-2408. ISSN: 0006-2960.
- [108] SANCHO J., SERRANO L., FERSHT A.R. Histidine residues at the N- and C-termini of alpha-helices: perturbed pK_as and protein stability. *Biochemistry* 1992, **31**, 2253-2258. ISSN: 0006-2960.
- [109] WEINER S.J., KOLLMAN P.A., CASE D.A., SINGH U.C., GHIO C., ALAGONA G., PROFETA S., WEINER P. A new force-field for molecular mechanical simulation of nucleic-acids and proteins. *J. Am. Chem. Soc.* 1984, **106**, 765-784. ISSN: 0002-7863.
- [110] SELA M., KATCHALSKI E. Spectrophotometric titration α -amino acid copolymers containing tyrosine. *J. Am. Chem. Soc.* 1956, **78**, 3986-3989. ISSN: 0002-7863.
- [111] VINOGRADOV S.N., LINNELL R.H. *Hydrogen Bonding*. New York: Van Nostrand Reinhold, 1971.
- [112] MAYER R., TOULME F., MONTENAYGARESTIER T. HELENE C. The role of tyrosine in the association of proteins and nucleic-acids. Specific recognition of single-stranded nucleic-acids by tyrosine-containing peptides. *J. Biol. Chem.* 1979, **254**, 75-82. ISSN: 0021-9258.
- [113] AKAMA K., SATO H., FURIHATA-YAMAUCHI M., KOMATSU Y., TOBITA T., NAKANO M. Interaction of Nucleosome Core DNA with Transition Proteins 1 and 3 from Boar Late Spermatid Nuclei. *J.Biochem.* 1996, **119**, 448-455. ISSN: 0021-924X.
- [114] TAN L., YAO S.Z., XIE Q.J., ZHANG Y.Y. Studies on interaction of tyrosine with DNA by fluorescence spectra. *Anal. Lett.* 2003, **36**, 2167-2181. ISSN: 0003-2719.
- [115] FOTOUHI L., TABATABAEE R. A study of the interaction tyrosine and DNA using voltammetry and spectroscopy methods. *Spectrochim. Acta A.* 2014, **121**, 152-156. ISSN: 1386-1425.

8. List of abbreviations

ARG	Arginine
CArg box	DNA sequence CC(A/T)6GG
CD	circular dichroism
DCA	Dichloroacetamide
DNA	deoxyribonucleic acid
ds DNA	double stranded DNA
FA	factor analysis
Fmoc	fluorenylmethyloxycarbonyl
FTIR	Fourier-transform infrared spectroscopy
GLU	glutamic acid
GOR	Garnier-Osguthorpe-Robson method
GTF	general transcription factor
HIS	Histidine
HPLC	high-performance liquid chromatography
IFE	inner filter effect
LYS	Lysine
MADS box	family of TF, abbreviation of its earliest four founded members: MCM1, Agamous , Deficiens and SRF
MIR	mid-infrared
OD	optical density
PDB	protein data bank
PHE	Phenylalanine
RNA	ribonucleic acid
SRE	serum response element
SRF	serum response factor
ss DNA	single stranded DNA
SVD	singular value decomposition
TF	transcription factor
TFA	ammonium trifluoroacetate
TRP	Tryptofan
TYR	Tyrosine
UV	Ultraviolet
VMD	visual molecular dynamics

9. List of Figures

Figure 1. Expression of genetic information [1].	7
Figure 2. Initiation of transcription in eukaryotic cell (adapted from [1]). Transcription factors are marked as A,B...H.	9
Figure 3. Binding of transcription factors to the regulatory promoter elements in eukaryotes [5]. Abbreviations: TATA box (sequence TATA(A/T)A(A/T)), BRE (TFIIB Recognition Element), DPE (Downstream Promoter Element), CCAAT box (sequence GGCCAATCT).	10
Figure 4. General scheme of response to signals from extracellular signalling proteins through cell surface receptors to the nucleus. Latent cytoplasmatic factors activated by phosphorylation (green), regulated phosphorylation or proteolysis (light purple), and second messenger fluctuations (light blue). Internal signals regulate proteolysis at the plasma membrane liberating some transcription factors (dark purple). Resident nuclear proteins (yellow, □) may be phosphorylated on serine and thus activated either by binding to DNA or free at nucleus) [6].	12
Figure 5. Relative sizes of the 10 human TF superclasses distinguished according to the type of DNA binding domain [7].	13
Figure 6. Protein sequences of non-identical MADS domains aligned to show their homology. The amino acid positions involved in DNA contacts, dimerization interactions and α , β structure are indicated below for the core SRF [26].	15
Figure 7. Structure of MADS-domain proteins and their function in determining floral organ identity [45]. Structures of 'floral quartets'. Multimeric complexes of MIKCC-group proteins, bound to two DNA sequence elements (CArG-boxes) present in numerous target genes, determine floral organ identity.	16
Figure 8. Model of two principal pathways regulating SRF activity in non-muscle cells [58].	18
Figure 9. Core SRF sequence (residues 132-223). The α and β secondary structure assignment are boxed, MADS box region is marked by purple (according to Pellegrini, et al. [26]).	18
Figure 10. The core SRF/DNA complex (PDB file 1srs [26] visualized by VMD [61]). Left: Position of the MADS box within the core SRF (marked by violet colour). Middle: View perpendicular to the molecular two-fold and overall DNA helix axes. Right: View revealing the stab-like structure of the monomers. The two SRF-core monomers (blue and red) have highly similar conformations. DNA recognition segment is in dark grey colour (middle and right).	19
Figure 11. Orientations of the absorption transition moments of the tyrosine lowest-energy singlet-singlet electronic transitions [64].	21
Figure 12. Absorption and emission spectra of aromatic amino acids [68].	22
Figure 13. Polarized Raman spectra of L-tyrosine in aqueous solutions of pH 13 (A) and pH 1 (B). Upper curves: the scattered radiation polarized parallel to the polarization	

direction of the exciting radiation. Lower curves: the scattered radiation polarized perpendicular to the polarization direction of the exciting radiation [70].	24
Figure 14. Nomenclature of the ring modes in benzene molecule [73, 77].	25
Figure 15. Published articles concerning the MADS box in each year. (Taken from the Web of Science; topic = "MADS box".)	26
Figure 16. Studied model oligopeptides of the human SRF MADS box (in boxes). The MADS box sequence within the SRF is highlighted by grey background. Green colour shows hydrophobic, red colour positively charged and blue negatively charged amino acids at neutral pH).	28
Figure 17. A) Raman spectra of oligopeptide JS06 in water measured after each step of repurification. Spectra are normalized at 1004 cm ⁻¹ band. B) Raman spectrum of ammonium trifluoroacetate in water.	32
Figure 18. Basic scheme of the Raman scattering apparatus	35
Figure 19. Raman microcell scheme. The microcell is designed for measurements of small amount of sample (12-20uL according to the sample capillary). Laser beam passes the cell longitudinally through the sample capillary and holes in the sealing screws. Scattered radiation is collected perpendicularly from the central part of the sample capillary. The cell is placed inside a thermostated holder.	35
Figure 20. Unwanted signal in Raman spectra. Spectra of used dissolving agents, artefact signal of the microcell glass and possible impurity from the synthesis of oligopeptides (TFA).	36
Figure 21. SVD results of the tyrosine fluorescence in dependence on its concentration. (To completely avoid possible contributions from elastic scattering of the excitation, only spectral region 300-370 nm was analysed.) Red line in the graph of V1 corresponds to the fit.	44
Figure 22. The effect of optical density on the fluorescence intensity of tyrosine and its correction. Black line shows the measured fluorescence intensities. Blue and red circles indicate corrected intensities according to equation (3.1) (*) and to our fit (**). Red curve is a linear regression of (**) corrected intensities. (ODem = 0 in both cases).	44
Figure 23. Short model oligopeptides within the sequence of human SRF. Denoted is the secondary structure in single crystal of SRF dimer with target DNA element according to X-ray [26].	46
Figure 24. pH dependence of CH08 oligopeptide absorption spectra. From acidic (red) to basic (violet) pH.	47
Figure 25. Factor analysis (SVD) of pH dependency of CH08 absorption and its fit according to chapter 3.3.3. (A) SVD characteristics. Red lines show the results of the fit. (B) Determined pH dependences of the two CH08 forms. (C) Isolated absorption spectra of both forms.	47
Figure 26. pH dependence of CH08 oligopeptide fluorescence spectra.	48
Figure 27. Factor analysis (SVD) of pH dependency of CH08 fluorescence and its fit according to chapter 3.3.3. (A) SVD characteristics. Red lines show the results of the	

fit. (B) Determined pH dependences of the two CH08 forms. (C) Isolated emission spectra of both forms, normalized by using coefficients $n_A = 0.003$, $n_B = 0.201$	49
Figure 28. Stern-Volmer plots of CH08 fluorescence quenching by DCA. Left: CH08 in 25mM acetate buffer, pH 3.2. Right: CH08 in 25mM cacodylate buffer, pH 7.0.....	50
Figure 29. SVD results of CH08 fluorescence quenching by DCA. Black and red lines in the graph of V1 correspond to the fit applied to the values corresponding tot neutral and acidic pH, respectively.	51
Figure 30. Electronic circular dichroism spectra of CH08 oligopeptide in acetate buffer (red), in water (green) and in a sodium bicarbonate buffer (blue).	52
Figure 31. Raman spectra of CH08 measured at acidic (red), neutral (green), and basic pH (blue). The most distinctive bands are assigned according to the literature [71-72, 97].	53
Figure 32. Infrared absorption spectra of CH08 in the region of amide I and amide II bands at various pH. The red solid curves represent the original spectra (normalized) while the blue dash-dot lines are their second derivatives (smoothed by Savitski-Golay function over 21 points).	56
Figure 33. Electronic circular dichroism spectra of the JS01 oligopeptide in water pH 5.0 (green) and in a sodium bicarbonate buffer pH 11.0 (blue).	58
Figure 34. Raman spectrum of JS01 oligopeptide measured in water at pH 5.0. Most distinctive bands are assigned according to the literature [71-72, 97].	59
Figure 35. Raman spectrum of JS03 oligopeptide measured in water at pH 5.0. Most distinctive bands are assigned according to the literature [71, 76, 96].....	60
Figure 36. Raman spectrum of JS02 oligopeptide measured in water at pH 5.0. Most distinctive bands are assigned according to the literature [71, 76, 100].....	61
Figure 37. Longer model oligopeptides within the sequence of human SRF. Secondary structure according to X-ray [26].	62
Figure 38. Raman spectra of JS04, JS05, and JS06 oligopeptides measured in water at pH 4.0. Most distinctive bands are assigned according to the literature [71, 76, 102]. Besides the overall spectra (A), details of important spectral regions are shown below: (B) Tyrosine Fermi doublet, (C) Characteristic phenylalanine vibrations, (D) In-plane stretching vibrations of tyrosine and phenylalanine rings.....	63
Figure 39. Comparison of JS04-6 oligopeptide and tyrosine corrected fluorescence (left) and absorption (right) spectra. Fluorescence and absorption spectra are normalized at 302 nm and 275 nm respectively.....	64
Figure 40. The MADS box segment of human SRF. Secondary structure according to X ray [26].	65
Figure 41. Normalized fluorescence emission (red) and excitation (blue) spectra of the MADS box in water. The emission spectrum was excited at 275 nm. The excitation spectra were recorded for emissions at 293 nm, 304 nm, and 325 nm.....	66

Figure 42. Possible H-bond formation between tyrosine and histidine in the X-ray structure of the SRF MADS box [26] (visualized using the VMD [61]). The distance of H..O is ca.1.9 Å.	67
Figure 43. The factor analysis (SVD) results of the MADS-box emission spectra quenched by iodide. Red solid lines represent the fit of coefficients according to Stern-Volmer equation.	68
Figure 44. Two differently quenched spectral components (left) and their decreasing fractions in the spectra of the MADS box with increasing iodide concentrations (right). Solid lines correspond to the more efficiently quenched F_I component and dashed lines to the second component F_{II}	68
Figure 45. The factor analysis (SVD) results of the MADS-box emission spectra quenched by iodide (red triangles) and cesium (blue circles). Solid lines represent the fit of coefficients according to Stern-Volmer equation.	69
Figure 46. Two differently quenched spectral components (left) and their Stern-Volmer representation (right). Solid lines correspond to the more efficiently quenched F_I component and dashed lines to the second component F_{II} . Circles and red color correspond to Cs^+ , triangles and blue to I^- quenching.	70
Figure 47. pH dependence of the MADS box fluorescence and absorption spectra. From acidic (red) to basic (violet) pH.	71
Figure 48. The factor analysis (SVD) results of both fluorescence and absorption spectral pH titration of the MADS box shown in common graphs. Solid curves inside the graphs of coefficients show the joint fit according to the model of three acido-basic equilibria.	72
Figure 49. Absorption spectral components $F^{A'}$, $F^{B'}$, $F^{C'}$, $F^{D'}$ (lower right) and fluorescence spectral components F^A , F^B , F^C , F^D (lower left) extracted by a joint fit of the SVD results of the MADS-box pH titration. Relative occurrences of particular components at various pH are shown in the upper graph.	73
Figure 50. FC (and FC') fluorescence (and absorption) component and its comparison with two considered linear combination of FB and FD (FB' and FD') components.	74
Figure 51. Comparison of components FA and FB and their difference spectrum. All spectra are normalized at their maxima.	74
Figure 52. The most important changes of the charges of the MADS box amino acids induced by pH alteration.	76
Figure 53. Measured absorption spectra of modSRE addition to JS06 sample. (i) Samples in buffer. (ii) Samples in buffer and 0.5 M NaCl. Solid lines correspond to solutions with oligopeptide, dashed lines to reference solutions.	78
Figure 54. Corrected fluorescence spectra of modSRE addition to JS06 sample. (i) Samples in buffer. (ii) Samples in buffer and 0.5 M NaCl. Spectra were corrected for IFE*, Raman scattering, background and dilution (as described in chapters 3.2.1 and 4.1.1).	78
Figure 55. The factor analysis (SVD) results of fluorescence spectra during modSRE addition to JS06 sample. Black circles represent samples dissolved in buffer (i); white circles samples in buffer and 0.5 M NaCl (ii).	79

- Figure 56. (i) Measured absorption spectra of modSRE solution during gradual addition of JS06 ; (ii) the same experiment for solution with 0.5 M NaCl. Solid lines correspond to the oligonucleotide solution, dashed lines to JS06 added to the reference solvent. 80
- Figure 57. Factor analysis (SVD) of JS06 addition to modSRE solution monitored by UV absorption. Black circles correspond to mixed solutions in buffer, white circles to solutions where peptide/DNA interaction was prevented by high salinity (0.5 M NaCl). 81
- Figure 58. Factor analysis (SVD) of JS06 addition to modSRE solution monitored by UV absorption, limited for low peptide concentrations when no clear signs of precipitation were observed. Black circles correspond to mixed solutions in buffer, white circles to solutions where peptide/DNA interaction was prevented by high salinity (0.5 M NaCl). 82
- Figure 59. (i) Measured fluorescence spectra of modSRE solution during gradual addition of JS06 oligopeptide; (ii) the same experiment with the oligonucleotide solution of high salinity (0.5 M NaCl). Solid lines correspond to the oligonucleotide solution, dashed lines to the oligopeptide added to the reference solvent..... 83
- Figure 60. (i) Corrected fluorescence spectra of modSRE solution during gradual addition of JS06 oligopeptide (only spectra before precipitation). Corrections are described in chapters 3.2.1 and 4.1.1). (ii) The same experiment with the oligonucleotide solution of high salinity (0.5 M NaCl). Solid lines correspond to the oligonucleotide solution, dashed lines to the oligopeptide added to the reference solvent. 83
- Figure 61. Factor analysis (SVD) of JS06 oligopeptide addition to modSRE sample fluorescence, limited for low peptide concentrations when no clear signs of precipitation were observed. Circles represent the samples dissolved in buffer, and triangles the samples in buffer and 0.5 M NaCl). Blue symbols represent solutions with DNA; grey symbols reference solutions without DNA..... 84
- Figure 62. Factor analysis (SVD) of JS04-6 oligopeptide addition to modSRE oligonucleotide sample fluorescence limited for low peptide concentrations. All spectra were normalized according to reference solution. Circles represent samples dissolved in buffer; triangles samples in reference solution without DNA. Black symbols represent JS05; red JS06 and blue JS04 oligopeptide..... 86

10. List of Tables

Table 1. Properties of amino acids within the SRF MADS box.	20
Table 2. Summary of employed model oligopeptides.	28
Table 3. Summary of model oligonucleotides. *Extinction coefficients of single stranded (ss) and double stranded (ds) oligonucleotides were calculated using the nearest neighbour model [80].	29
Table 4. Frequencies of selected vibrational modes of tyrosine and tyrosinate observed in Raman spectra of CH08 oligopeptide.	54
Table 5. Summary of interaction experiments – decrease of tyrosine quantum yield comparing the solution with and without DNA (additions of oligopeptide to oligonucleotide solution).	85

11. Attachments

- [I] ŘEZÁČOVÁ B., COIC Y.M., ZENTZ C., TURPIN P.Y., ŠTĚPÁNEK J. Spectroscopic Determination of pKa Constants of MADS Box Segments. *Spectrosc. Int. J.* 2012, **27**, 455-461. ISSN: 0712-4813.
- [II] PROFANTOVÁ B., PROFANT V., ZÍMA V., KOPECKÝ JR. V., BEDNÁROVÁ L., ZENTZ C., BAUMRUK V., TURPIN P.Y., ŠTĚPÁNEK J. Protonation effect of tyrosine in a segment of the SRF transcription factor: A combined optical spectroscopy, molecular dynamics, and density functional theory calculation study. *J. Phys. Chem. B.* 2013, **117**, 16086-16095. ISSN: 1520-6106

Attachment I.

Spectroscopic determination of pKa constants of MADS box segments

Barbora Řezáčová^{a,b*}, Yves-Marie Coïc^c Christian Zentz^b, Pierre-Yves Turpin^b and Josef Štěpánek^a

^a *Institute of Physics, Faculty of Mathematics and Physics, Charles University in Prague, Ke Karlovu 5, CZ-12116 Prague 2, Czech Republic*

^b *Laboratoire Acides Nucléiques et Biophotonique, FRE 3207, Université Pierre et Marie Curie, place Jussieu 4, 75252 Paris Cedex 5, France*

^c *Unité de Chimie des Biomolécules, URA 2128 CNRS, Institut Pasteur, Rue Du Dr. Roux 28, 75724 Paris Cedex 15, France*

Abstract: We have introduced a new promising approach for the determination of pKa constants of oligopeptide intrinsic fluorophores and spectral components referring to their differently charged states. The method is based on the factor analysis of multiwavelength spectroscopic pH titration data. As an illustration we present its application on the study of short segments of the MADS box, which is a highly conserved sequence of a so-called family of transcription factors, by techniques of UV absorption and fluorescence spectroscopies. Investigated oligopeptides contain no tryptophan but one tyrosine serving as an intrinsic fluorophore and absorber. The results indicate both good sensitivity and spectroscopic selectivity of our method, which thus may be considered as a complementary technique to conventional electrochemical methods.

Keywords: *factor analysis, dissociation constant, fluorescence spectroscopy, MADS box, tyrosine*

Spectroscopic Determination of pKa Constants of MADS Box Segments

Barbora Řezáčová,^{1,2} Yves-Marie Coïc,³ Christian Zentz,²
Pierre-Yves Turpin,² and Josef Štěpánek¹

¹*Faculty of Mathematics and Physics, Institute of Physics, Charles University in Prague, Ke Karlovu 5, 12116 Prague 2, Czech Republic*

²*Laboratoire Acides Nucléiques et Biophotonique, FRE 3207, Université Pierre et Marie Curie, place Jussieu 4, 75252 Paris Cedex 5, France*

³*Unité de Chimie des Biomolécules, URA 2128 CNRS, Institut Pasteur, rue du Dr. Roux 28, 75724 Paris Cedex 15, France*

Correspondence should be addressed to Barbora Řezáčová, rezacova@karlov.mff.cuni.cz

Copyright © 2012 Barbora Řezáčová et al. This is an open access article distributed under the Creative Commons Attribution License, which permits unrestricted use, distribution, and reproduction in any medium, provided the original work is properly cited.

Abstract. We have introduced a new promising approach for the determination of pKa constants of oligopeptide intrinsic fluorophores and spectral components referring to their differently charged states. The method is based on the factor analysis of multiwavelength spectroscopic pH titration data. As an illustration, we present its application on the study of short segments of the MADS box, which is a highly conserved sequence of a so-called family of transcription factors, by techniques of UV absorption and fluorescence spectroscopies. Investigated oligopeptides contain no tryptophan but one tyrosine serving as an intrinsic fluorophore and absorber. The results indicate both good sensitivity and spectroscopic selectivity of our method, which thus may be considered as a complementary technique to conventional electrochemical methods.

Keywords: Factor analysis, dissociation constant, fluorescence spectroscopy, MADS box, tyrosine

1. Introduction

Proteins are biological molecules that usually contain amino acids with both acidic and basic functional groups. These amino acids can be divided into several categories according to their residue charge, polarity, and hydrophobicity. Titratable amino acids of the protein may be completely exposed to solution or buried inside the 3D structure of the protein. Their pKa constants are thus influenced by protein folding and may be sensitive to protein oligomerization, binding of ligand, denaturation, and so forth.

Determination of pKa constants of proteins is usually done by electrochemical techniques (e.g., polarimetric, potentiometric, and voltammetric titration). Direct techniques such as NMR can be used on small peptides to monitor their ionization state.

There are also several methods of computational biology, molecular modelling, and structural bioinformatics, which can be used to estimate roughly the pKa values of titratable amino acids within proteins.

In this work, we present a highly sensitive method of pKa determination (complementary to the methods mentioned previously), based on a factor analysis of spectroscopic data, obtained namely from UV-visible absorption and fluorescence measurements. Analogous methodology can though be applied to any other kind of spectroscopic data. It should be mentioned that factor analysis has already been used to determine pKa values of small organic molecules [1, 2]; however, it has not been used to study peptides so far (to our current knowledge).

The MADS box family of transcription factors counts over 200 members playing a crucial role in the gene regulation of higher organisms. The MADS box acronym is derived from initials of four of the originally identified members of the family: MCM1, AG, DEFA, and SRF [3]. These transcription factors share a highly conserved DNA binding motif showing a wide sequence homology of 56 amino acids. Still little is known about how targeted DNAs are recognized by these transcription factors. Available structural data reveal that MADS box protein-DNA complexes have a high structure homology, but with differences in the DNA binding process [4–9].

Core SRF contains its own intrinsic fluorophores: three tyrosines with different amino-acidic environments. In order to distinguish between these tyrosines and to see the effect of diverse environments, the pH dependency measurements of two small segments of SRF, each containing one tyrosine, were performed by using UV absorption and fluorescence spectroscopies: $_{154}\text{KLLRYTTFS}_{162}$ and $_{168}\text{IMKKAYEL}_{175}$.

2. Materials and Methods

2.1. Materials

Synthesis of octamer oligopeptide of sequence Ac-IMKKAYEL-amid, average $M_w = 1036.30$, was carried out according to the Fmoc/tBu solid-phase strategy [10] on a 433A peptide synthesizer (Applied Biosystems-Forster City, CA, USA), using a Fmoc Amide Resin (Applied Biosystems). Mass characterization of the purified peptide (above 98% by RP-HPLC) was consistent with the expected value.

HPLC 98% purified oligopeptide Ac-KLRRYTTFS-amid, $M_w = 1212.43$, was purchased from Apigenex (Prague, Czech Republic). Purity and mass weight were tested by HPLC and MS.

Spectroscopically pure KOH and HCl were obtained from Normapur and MERCK.

2.2. Optical Absorbance and Fluorescence Measurements

Optical absorbance spectra were recorded on a Cary 3E UV-visible spectrophotometer. Fluorescence measurements were performed on a SLM Aminco-Bowman series 2 luminescence spectrometer. The excitation and emission spectral bandwidths used were 4 nm. The optical path length was 1 cm. Upon excitation at 276 nm, both tyrosine and tyrosinate contribute to the fluorescence emission. All fluorescence spectra were corrected for a minor inner filter effect (optical density being below 0.1) [11], and contributions of Rayleigh and Raman light scattering were subtracted. Spectra were also corrected

(slight intensity renormalization) for the small changes of concentration of oligopeptides resulting from the addition of HCl and/or KOH.

Fluorescence and absorption spectra of oligopeptides were measured in the pH range from 3 to 11 at room temperature (20°C). Concentration of the oligopeptide was $8 \cdot 10^{-5}$ M. Addition of HCl or KOH caused no precipitation.

Measurements of pH were made on a IQ Scientific Instruments pH meter IQ170G equipped with a stainless steel pH probe.

2.3. Spectra Analysis

To find out the individual components forming the resulting fluorescence or absorption spectra, we submitted the set of spectra $F_i(\lambda)$ obtained at various pH conditions to factor analysis, that is, singular value decomposition (SVD) algorithm decomposing a set of N spectra into a set of orthogonal normalized spectral profiles $S_j(\lambda)$, $j = 1, 2, \dots, N$,

$$F_i(\lambda) = \sum_{j=1}^M V_{ij} W_j S_j(\lambda), \quad (2.1)$$

where the normalized coefficients V_{ij} quote the relative portions of the j th spectral profile $S_j(\lambda)$ in the original spectra $F_i(\lambda)$ [12]. The singular numbers W_j stand for the statistical weights of spectral profiles. As the spectral components are ordered to reach a descending succession of singular values, usually a few first terms at the right side are sufficient to approximate the original spectral set within an experimental error. This value of M is referred to as factor dimension. It represents the minimal number of independent components resolved in the analyzed spectral set.

In case of M equal to two (which is actually the case in the present paper), the spectral components attributable to the two different components A and B in the spectra (from either absorption or fluorescence) can be extracted, so that

$$F_i(\lambda) = F^A(\lambda) * C_i^A + F^B(\lambda) * C_i^B, \quad (2.2)$$

where $F^A(\lambda)$ and $F^B(\lambda)$ are the spectral components forming the original spectra proportionally to their current concentrations C_i^A and C_i^B . These are given by the current pH value as

$$C_i^A = \frac{1}{1 + 10^{\text{pH} - \text{pKa}}}, \quad C_i^B = C_i^A * 10^{\text{pH} - \text{pKa}}, \quad (2.3)$$

where pKa is the dissociation constant of the chromophore (here tyrosine).

Thanks to the factor dimension of two, both $F^A(\lambda)$ and $F^B(\lambda)$ components can be well approximated as linear combinations (with coefficients r_j^A and r_j^B) of the first and the second SVD spectral profiles

$$F^A(\lambda) = \sum_{j=1}^2 r_j^A * S_j(\lambda), \quad F^B(\lambda) = \sum_{j=1}^2 r_j^B * S_j(\lambda). \quad (2.4)$$

Considering the above-mentioned basic SVD formula for $F_i(\lambda)$ and orthogonality of SVD spectral components, we obtained a final set of $2 \times N$ equations

$$W_j V_{ij} = r_j^A * \frac{1}{1 + 10^{\text{pH} - \text{pKa}}} + r_j^B * \left(1 - \frac{1}{1 + 10^{\text{pH} - \text{pKa}}} \right), \quad i = 1, 2, \dots, N, \quad j = 1, 2. \quad (2.5)$$

The five unknown parameters (pKa , r_j^A , r_j^B ; $j = 1, 2$) can be solved by means of a simultaneous nonlinear least-square fit of the right sides in (2.5) to the left ones.

3. Results and Discussion

3.1. Absorption Spectra

In the measured region 220–330 nm, both oligopeptides show a characteristic peak at 275 nm typical for tyrosine. Noticeable changes were observed by increasing the pH: the absorption band moved to longer wavelength at 294 nm, with a 1.5-fold increase of intensity (data not shown).

3.2. Fluorescence Spectra

In the measured region 290–390 nm, both oligopeptides have a characteristic peak at 303 nm typical for tyrosine. With an increase of the pH, the emission significantly decreases thanks to deprotonation of tyrosine to tyrosinate (see Figure 1(a)), which has a much lower fluorescence quantum yield [13] and its emission is shifted to higher wavelengths at about 345 nm [14].

3.3. Analysis of pH Dependent Fluorescence Spectra

Results of factor analysis applied on fluorescence spectra of oligopeptide Ac-IMKKAYEL-amid are shown in Figure 1(d). We obtained a factor dimension of 2 (the same as for absorption spectra). The first spectral profile S_1 represents an average of measured spectra, and the 1st coefficients V_1 thus describe the decrease of the overall spectral intensity as a function of pH. The second spectral profile S_2 , which is about 100 times less significant than the first one, accounts for the main spectral changes. Contribution of this profile is about zero for spectra below pH 7, while above this pH its value increases, as can be seen from the behaviour of the 2nd coefficients V_2 .

By using our method, pKa constants were determined for both fluorescence and absorption data with a good agreement for both oligopeptides. From the oligopeptide Ac-IMKKAYEL-amid absorption

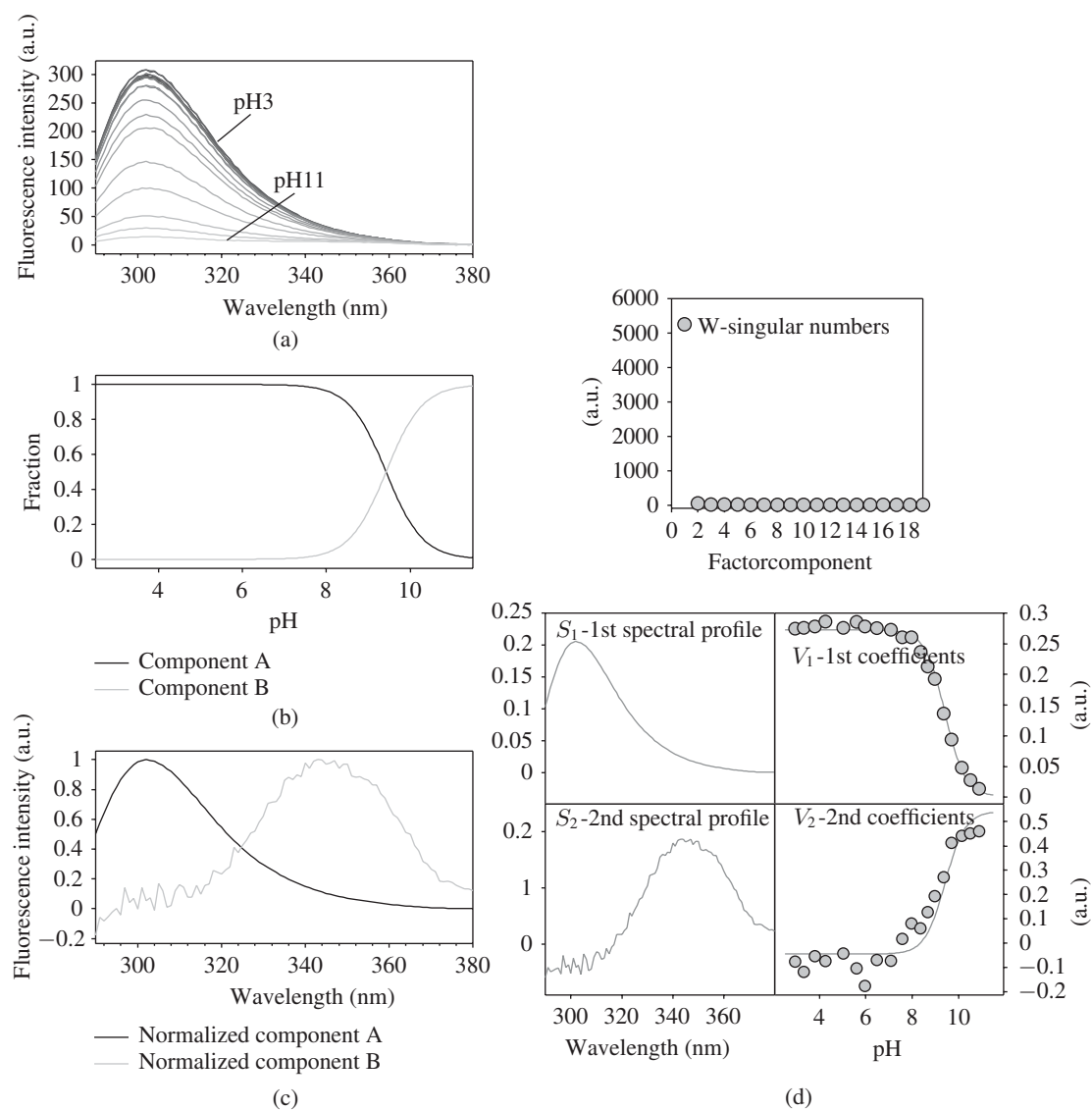


Figure 1: Fluorescence pH dependency of the MADS box segment Ac-IMKKAYEL-amid (a), determined fractions (b), normalized emission spectra of the two components—normalization factor $N_A = 0.003$, $N_B = 0.201$ (c), and factor analysis results (d).

we obtained $pK_a = 9,45 \pm 0,05$, from its fluorescence spectra $pK_a = 9,43 \pm 0,06$. For oligopeptide Ac-KLRRYTTFs-amid absorption, we obtained $pK_a = 9,01 \pm 0,05$, and using fluorescence spectra, we calculated $pK_a = 9,03 \pm 0,06$. This is in good agreement with previous determinations of tyrosine pK_a in various oligopeptides [15, 16].

In correspondence with our assumptions, we observed that the positively charged amino acids (R: arginines; K: lysines) do shift the dissociation constant of the free-state tyrosine to lower values (the dissociation constant of free tyrosine is 10.07 [15, 17]).

Moreover, using this method, we were able to distinguish the two emission components (see Figure 1(c)) and their respective fractions (Figure 1(b)). Component *A* represents the tyrosine emission spectrum (maximum at 303 nm), whereas component *B* represents the emission of tyrosinate (maximum near 345 nm), which is about 60 times weaker.

4. Conclusions

Using the factor analysis on absorption and fluorescence-monitored titration, we were able to determine the pKa constants of two tyrosine-containing oligopeptides with a high precision as well as absorption and fluorescence spectral profiles corresponding to the differently charged forms. Furthermore, we obtained quantitative information about the effect of a specific environment on pKa of tyrosine, which will help us to better distinguish between the different tyrosines in MADS^{SRF}.

The presented methodology is applicable to any oligopeptide bearing at least one pH-dependent photosensitive amino acid or probe and in general can be applied to a vast number of spectroscopic techniques reflecting protonation changes in peptides. Further study on larger oligopeptide segments of SRF will be performed.

Acknowledgments

This work is supported by the Czech Science Foundation (Project 202/09/0193) and Grant Agency of Charles University (Project 402111). B. Řezáčová gratefully acknowledges the French Government support for her stay in Laboratoire Acides Nucléiques et Biophotonique.

References

- [1] M. Meloun, Z. Ferenčíková, and A. Vrána, "The thermodynamic dissociation constants of methotrexate by the nonlinear regression and factor analysis of multiwavelength spectrophotometric pH-titration data," *Central European Journal of Chemistry*, vol. 8, no. 1, pp. 494–507, 2010.
- [2] K. Y. Tam and K. Takács-Novák, "Multiwavelength spectrophotometric determination of acid dissociation constants—part II. First derivative versus target factor analysis," *Pharmaceutical Research*, vol. 16, pp. 374–381, 1999.
- [3] P. Shore and A. D. Sharrocks, "The MADS-box family of transcription factors," *European Journal of Biochemistry*, vol. 229, no. 1, pp. 1–13, 1995.
- [4] M. Hassler and T. J. Richmond, "The B-box dominates SAP-1-SRF interactions in the structure of the ternary complex," *EMBO Journal*, vol. 20, no. 12, pp. 3018–3028, 2001.
- [5] K. Huang, J. M. Louis, L. Donaldson, F. L. Lim, A. D. Sharrocks, and G. M. Clore, "Solution structure of the MEF2A-DNA complex: structural basis for the modulation of DNA bending and specificity by MADS-box transcription factors," *EMBO Journal*, vol. 19, no. 11, pp. 2615–2628, 2000.
- [6] Y. Mo, W. Ho, K. Johnston, and R. Marmorstein, "Crystal structure of a ternary SAP-1/SRF/c-fos SRE DNA complex," *Journal of Molecular Biology*, vol. 314, no. 3, pp. 495–506, 2001.
- [7] L. Pellegrini, S. Tan, and T. J. Richmond, "Structure of serum response factor core bound to DNA," *Nature*, vol. 376, no. 6540, pp. 490–498, 1995.

- [8] E. Santelli and T. J. Richmond, "Crystal structure of MEF2A core bound to DNA at 1.5 Å Resolution," *Journal of Molecular Biology*, vol. 297, no. 2, pp. 437–449, 2000.
- [9] S. Tan and T. J. Richmond, "Crystal structure of the yeast MAT α 2/MCM1/DNA ternary complex," *Nature*, vol. 391, no. 6668, pp. 660–666, 1998.
- [10] W. C. Chan and P. D. White, *Fmoc Solid Phase Peptide Synthesis: A Practical Approach*, Oxford University Press, London, UK, 2000.
- [11] J. R. Lakowicz, *Principles of Fluorescence Spectroscopy*, Springer, Singapore, 3rd edition, 2006.
- [12] E. R. Malinowski, *Factor Analysis in Chemistry*, Wiley, New York, NY, USA, 2nd edition, 1991.
- [13] J. B. A. Ross, W. R. Laws, K. W. Rousslang, and H. R. Wyssbrod, "Biochemical applications," in *Topics in Fluorescence Spectroscopy*, J. R. Lakowicz, Ed., vol. 3, pp. 1–63, Kluwer Academic Publishers, New York, NY, USA, 2002.
- [14] A. G. Szabo, K. R. Lynn, D. T. Krajcarski, and D. M. Rayner, "Tyrosinate fluorescence maxima at 345 nm in proteins lacking tryptophan at pH7," *FEBS Letters*, vol. 94, no. 2, pp. 249–252, 1978.
- [15] M. Sela and E. Katchalski, "Spectrophotometric titration of α -amino acid copolymers containing tyrosine," *Journal of the American Chemical Society*, vol. 78, no. 16, pp. 3986–3989, 1956.
- [16] R. L. Thurlkill, G. R. Grimsley, J. M. Scholtz, and C. N. Pace, "pK values of the ionizable groups of proteins," *Protein Science*, vol. 15, no. 5, pp. 1214–1218, 2006.
- [17] A. L. Lehninger, D. L. Nelson, and M. M. Cox, *Lehninger Principles of Biochemistry*, W. H. Freeman, New York, NY, USA, 4th edition, 2004.

Attachment II.

Protonation Effect of Tyrosine in a Segment of the SRF Transcription Factor: A Combined Optical Spectroscopy, Molecular Dynamics and DFT Calculation Study

Barbora Profantová^{1, 2}, Václav Profant¹, Vlastimil Zíma¹, Vladimír Kopecký Jr.¹, Lucie Bednářová³, Christian Zentz⁴, Vladimír Baumruk¹, Pierre-Yves Turpin², Josef Štěpánek^{1, *}

¹ *Institute of Physics, Faculty of Mathematics and Physics, Charles University in Prague, Ke Karlovu 5, 121 16 Prague 2, Czech Republic*

² *Laboratoire Jean Perrin, FRE 3231, Université Pierre et Marie Curie, place Jussieu 4, 75252, Paris Cedex 5, France*

³ *Institute of Organic Chemistry and Biochemistry, Academy of Sciences of the Czech Republic, Flemingovo nám. 2, 166 10 Prague, Czech Republic*

⁴ *ER12, Université Pierre et Marie Curie, Place Jussieu 4, 75252, Paris Cedex 5, France*

Abstract: The high sensitivity to pH of a short segment (an octamer) of Serum Response Factor (SRF), an important member of the MADS box family of transcription factors, was investigated by Raman scattering, infrared and circular dichroism spectroscopies. Molecular dynamics (MD) and density functional theory (DFT) calculations enabled interpretation of spectral changes in close detail. Although there was a negligible difference between spectra in acidic and neutral environments, the spectrum in basic pH was substantially different. The major changes were attributed to the deprotonation of tyrosine. The secondary structure of the SRF octamer fragment was estimated experimentally as well as predicted theoretically by MD. All techniques proved that it exists in a dynamical equilibrium among several conformations mostly close to β -turn, unordered conformations and extended structure; in contrast to the stable secondary structure it possesses as a part of SRF. Generally, this approach represents a useful tool for study of various short oligopeptides.

Keywords: *MADS box, protein secondary structure, tyrosine, pH transition, Raman spectroscopy, infrared spectroscopy*

Protonation Effect of Tyrosine in a Segment of the SRF Transcription Factor: A Combined Optical Spectroscopy, Molecular Dynamics, and Density Functional Theory Calculation Study

Barbora Profantová,^{†,‡} Václav Profant,[†] Vlastimil Zíma,[†] Vladimír Kopecký, Jr.,[†] Lucie Bednárová,[§] Christian Zentz,[⊥] Vladimír Baumruk,[†] Pierre-Yves Turpin,[‡] and Josef Štěpánek^{*,†}

[†]Institute of Physics, Faculty of Mathematics and Physics, Charles University in Prague, Ke Karlovu 5, 121 16 Prague 2, Czech Republic

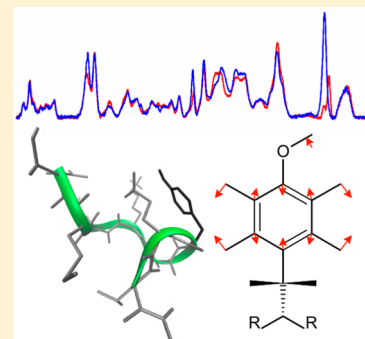
[‡]Laboratoire Jean Perrin, FRE 3231, Université Pierre et Marie Curie, place Jussieu 4, 75252 Paris CEDEX 5, France

[§]Institute of Organic Chemistry and Biochemistry, Academy of Sciences of the Czech Republic, Flemingovo nám. 2, 166 10 Prague 6, Czech Republic

[⊥]ER12, Université Pierre et Marie Curie, Place Jussieu 4, 75252 Paris CEDEX 5, France

Supporting Information

ABSTRACT: The high sensitivity to pH of a short segment (an octamer) of serum response factor (SRF), an important member of the MADS box family of transcription factors, was investigated by Raman scattering, infrared and circular dichroism spectroscopies. Molecular dynamics (MD) and density functional theory (DFT) calculations enabled interpretation of spectral changes in close detail. Although there was a negligible difference between spectra in acidic and neutral environments, the spectrum in basic pH was substantially different. The major changes were attributed to the deprotonation of tyrosine. The secondary structure of the SRF octamer fragment was estimated experimentally as well as predicted theoretically by MD. All techniques proved that it exists in a dynamical equilibrium among several conformations mostly close to β turn, unordered conformations, and extended structure, in contrast to the stable secondary structure it possesses as a part of SRF. Generally, this approach represents a useful tool for the study of various short oligopeptides.



INTRODUCTION

Transcription factors play an essential role in the gene regulation of higher organisms by binding to multiple target gene sequences in a complex manner. In particular, the so-called serum response factor (SRF), by binding to the DNA serum response element (SRE), regulates the transcription of a number of immediate early genes, neuronal and muscle genes, and thus controls cell growth and differentiation, neuronal transmission, and muscle function and development.¹ SRF is one of the first discovered members of a family of transcription factors that share a highly conserved segment of 56 amino acids, called the MADS box.² The MADS box of SRF has been identified as the major determinant for DNA-binding specificity.³ It is encompassed within a sequence of a hundred residues that form a core domain (core-SRF) responsible for the activities of DNA specific recognition and recruitment of accessory factors.^{4,5} The MADS box motif and its selected segments are believed to be able to serve as basic models for the study of local functional properties of the DNA recognition within the protein family.

The SRF MADS box contains three tyrosine residues that can be used as spectroscopic inner probes sensitive to changes in their environment. To distinguish contributions of individual

tyrosine moieties to the whole MADS box spectra, we investigated shorter segments of the MADS box. In a previous UV/fluorescence study, we revealed that pK_a values of MADS box tyrosines are affected by other amino acids located in their vicinity.⁶ These neighboring amino acids, and especially charged residues like arginine or lysine, tend to shift the dissociation constant of the free state of tyrosine.^{7,8}

Here, we focus on the extensive study of vibrational spectra of one of the substantial segments of the MADS box, located between the 168 and 175 positions of SRF (i.e., octamer^{SRF}) having the sequence: Ac-IMKKAYEL-amid. The X-ray structure of the complex formed by two core-SRF subunits bound to the DNA target shows that this oligopeptide constitutes the end of an α 1-helix, the main DNA binding element of the protein, and is situated at the junction with the dimerization domain.^{9,10} In the octamer^{SRF} sequence, Lys170, Lys171, and Glu174 amino acids are highly invariant, whereas Tyr173 is less conserved within the whole MADS box protein family.^{3,11}

Received: October 8, 2013

Revised: November 20, 2013

Published: November 21, 2013

In the available structures of core-SRF/DNA complexes Lys170 and Lys171 may be involved in forming salt bridges with the phosphate backbone of the DNA site, and their simultaneous mutation decreases core-SRF/DNA binding affinity,⁵ whereas Glu174 is involved in the core-SRF dimer interface.^{9,10,12} The variation of the repartition of charges and H-bonding configuration of less conserved Tyr173 are concerned in the specificity of core-SRF/DNA complex.¹³

When the fact that the X-ray structure of the octamer^{SRF} within the SRF is known is considered,⁹ its conformation as an isolated fragment in solution is expected to be dramatically different. In our study, we combine the electronic circular dichroism, Raman, and infrared spectroscopies with up-to-date theoretical techniques of molecular dynamics (MD) and density functional theory (DFT) calculations to verify whether it is possible to correctly simulate the behavior and spectroscopic properties of this relatively large system (154 atoms). The accuracy and sensitivity of calculated results can be elucidated from a comparison of the simulated spectra of the octamer^{SRF} in the secondary structure based on both X-ray of the whole SRF and MD prediction and from the direct comparison with the experimental data.¹⁴ The results can serve as an advanced tool for detailed vibrational analysis, interpretation of experimental spectra and further characterization of the selected inner probe, its sensitivity to variations of environmental conditions, and so forth. This is demonstrated by measurements at various pH and simulations of the octamer^{SRF} in differently charged states, which provide a detailed understanding of changes observed in the experimental spectra.

Generally, this approach, which is based on a close interconnection between experiments and MD simulations along with DFT calculations, represents a very powerful tool for general applications to the study of various short oligopeptides (up to ~180 atoms).

MATERIALS AND METHODS

Materials. The octamer^{SRF} oligopeptide of sequence Ac-IMKKAYEL-amid ($M_w = 1036.30$ Da) was synthesized according to the Fmoc/tBu solid-phase strategy¹⁵ on a 433A peptide synthesizer (Applied Biosystems) using a Fmoc Amide Resin (Applied Biosystems). The mass characterization of the purified peptide was in agreement with the expected value (above 98% by RP-HPLC). For spectroscopic measurements, the following buffers were used: 50 mM cacodylate buffer pH 7.0 (prepared using $(\text{CH}_3)_2\text{AsO}_2\text{Na}\cdot 3\text{H}_2\text{O}$ (Sigma Aldrich) and HCl (Merck)), acetate buffer pH 3.2 (prepared using glacial acetic acid (Penta) and CH_3COONa (Lachema)), and 50 mM sodium bicarbonate buffer pH 11.0 (prepared using NaOH (Fluka) and Na_2CO_3 (Lachema)). To avoid any loss of reliability in some spectral regions caused by the subtraction of buffer Raman and infrared bands, samples were also diluted in water with small amounts of NaOH (Normapur) or HCl (Merck) to reach pH 12 or 3.0, respectively.

Electronic Circular Dichroism. Circular dichroism (CD) spectra were recorded on Jasco J-815 spectropolarimeter (Jasco) purged with N_2 . The spectra were collected from 180 to 260 nm at room temperature in 0.1 cm quartz cells (with following parameters: peptide concentration = 4.7 mM, 2 scans, 0.5 nm steps, 20 nm/min speed, 8 s time constant, 1 nm spectral bandwidth) and from 230 to 380 nm in 1 cm quartz cells (with peptide concentration = 23.4 mM and with identical experimental parameters). After the baseline subtraction, the

final data were expressed as molar ellipticities, θ ($\text{deg cm}^2 \text{dmol}^{-1}$), per residue.

Raman Spectroscopy. Raman spectra were recorded on a Jobin-Yvon T64000 Raman spectrometer in a standard 90° geometry. Samples, having concentration 7.1 mM, were placed in a temperature-stabilized microcell of 20 μL internal volume and excited by the 488 nm/200 mW Ar^+ laser. Data were recorded in the spectral range from 600 to 1900 cm^{-1} ; the effective spectral resolution was $\sim 4 \text{ cm}^{-1}$. Raman spectra were corrected using a singular value decomposition-based method for intensity normalization, background correction, and solvent subtraction.¹⁶

Infrared Spectroscopy. Infrared spectra were recorded on a Bruker Vector 33 Fourier transform infrared (FTIR) spectrometer using a standard MIR global source, a KBr beamsplitter, and an MCT detector. 4000 scans were collected with a 2 cm^{-1} spectral resolution and a Blackman–Harris 3-term apodization function. Aqueous 2.9 mM peptide solutions were measured at room temperature in a CaF_2 cell with an 8 μm path length. The spectral contribution of water was corrected following the standard algorithm.¹⁷ Spectrum of water vapors was subtracted and, finally, the spectra were normalized at amide I band intensity.

THEORY

Molecular Dynamics. An all-atom structure model of the octamer^{SRF} with acetylated N-terminus and amidated C-terminus with overall charge +1 (neutral pH, see Figure 1)

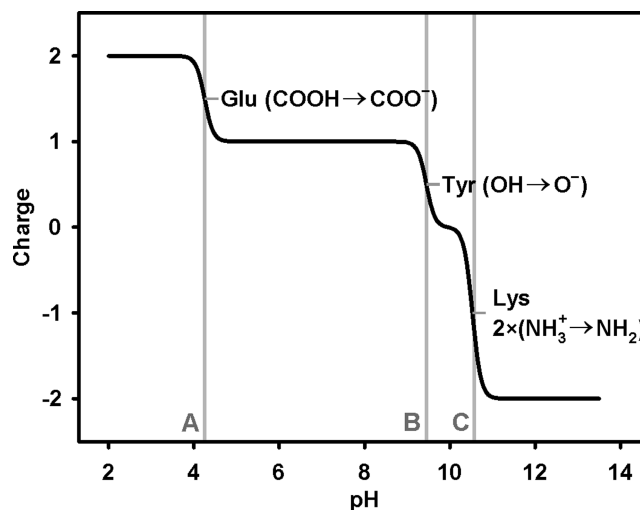


Figure 1. Titration curve of the octamer^{SRF}. pK_a transitions of R-groups: (A) glutamic acid $pK_a = 4.25$; (B) tyrosine $pK_a = 9.45$, (C) lysine $pK_a = 10.53$.

was created using the tLEaP program from the Amber Tools¹⁸ suite and the force field AmberFF99SB.¹⁹ The model was neutralized using a chloride anion and solvated in TIP3 water. The second model (overall charge 0, Figure 1) was created by replacing tyrosine with tyrosinate to simulate the oligopeptide state reached at high basic pH values. The force field for tyrosinate was generated using the R.E.D. server.^{20–23}

The initial equilibration of the systems was performed using NAMD 2.7 and 2.8²⁴ with time step of 2 fs and a cutoff 10 Å, PME grid size $48 \times 48 \times 48$, Langevin damping 1/ps, and all bonds rigid using Settle algorithm.²⁵ The systems were first minimized for 1000 steps and then thermalized to 310 K and

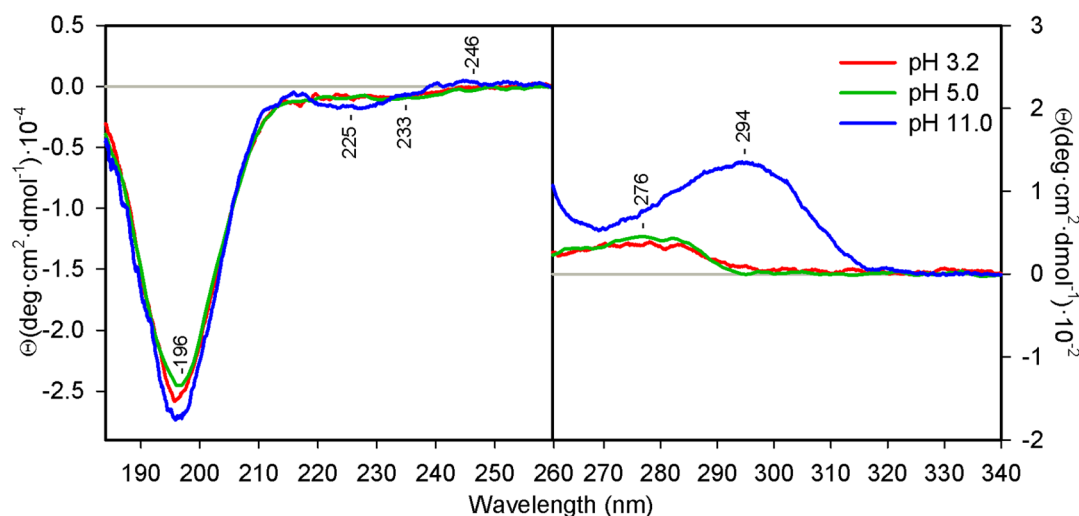


Figure 2. Electronic circular dichroism spectra of the octamer^{SRF} in an acetate buffer pH 3.2 (red), in water pH 5.0 (green) and in a sodium bicarbonate buffer pH 11.0 (blue).

equilibrated at 1 atm for 20 ns. Potential energies and volumes were monitored and reached stable values. For production runs, we used ACEMD²⁶ running on a local workstation equipped with GPU graphics card. The simulations were run in the NVT ensemble with the same parameters as for equilibration, except for a time step of 4 fs enabled by the hydrogen mass repartition scheme.²⁷ The initial 4 ns of each production trajectory were neglected due to possible artifacts from equilibration after change of configuration parameters for NVT ensemble, leaving a 400 ns trajectory with snapshots every 20 ps. Data analysis was performed using the program PTRAJ from the AmberTools¹⁸ suite and visualized using the VMD.²⁸ The secondary structure was analyzed using the DSSP method.²⁹ Cluster analysis was performed using an average-linkage algorithm with limit of the distance at 2.5 Å (every fifth snapshot was used, leaving 100 ps between frames).

QM Spectral Calculations. All input geometries were optimized by energy minimization using Gaussian09.³⁰ In the case of conformers obtained from MD simulations, backbone torsion angles were kept fixed during minimization (Mod-Redundant option). The force field and spectral intensities were calculated at the same theory level within the harmonic approximation by Gaussian, as well. We used standard DFT procedure³¹ employing the B3PW91 functional³² and 6-31G** basis set,³³ that is, the balanced level of calculation between the accuracy and time demands (~300 h of CPU time). Stability of the results toward other methods and functionals (HF, BPW91³⁴) and basis sets (6-31G, 6-31G*) was also checked. The molecular environment was accounted for the COSMO-PCM^{35,36} dielectric model.

Simulated Raman spectral profiles were generated by a convolution of calculated intensities with a Lorentzian function 10 cm⁻¹ wide (full width at half of maximum) and adjusted by a Boltzmann factor³⁷ to 298 K. The computed and experimental intensities were normalized to have similar magnitudes. The assignment of experimental bands to particular vibrational modes was performed by using the computer program Facio,³⁸ which provided animations of nuclear motions along computed normal modes. The final assignment was then based on agreement of experimental/calculated positional and intensity parameters.

For the direct comparison between experimental and calculated spectra (at DFT/B3PW91/6-31G**/COSMO level) an empirical scaling^{39,40} of wavenumber scale based on quadratic fit was applied. The five well assigned bands (evenly distributed across the experimental region) were selected, and their calculated wavenumber values were fitted at the experimental ones determining the coefficients of the quadratic fit as

$$\nu_s = -0.000568\nu_c^2 + 1.09\nu_c - 43.08 \quad (1)$$

where ν_c represents the calculated wavenumber and ν_s corresponds to the scaled wavenumber.

RESULTS AND DISCUSSION

Molecular Structure and Geometry. The sequence of octamer^{SRF} possesses four functional groups of amino acids (Tyr, Glu, and two Lys) that can be protonated/deprotonated depending on the acidity/basicity of environment. On the basis of pK_a's of free Glu 4.25,⁴¹ Lys 10.53,⁴¹ and Tyr 9.45 in the octamer^{SRF} (as determined in our preceding study;⁶ free Tyr has a pK_a of 10.07⁴¹), the titration curve can be depicted (see Figure 1). There are four differently charged states with charge $q = +2$ at acidic pH < 4, $q = +1$ at neutral pH ∈ (4.5–9.2), $q = 0$ at basic pH ∈ (9.7–10.3), and $q = -2$ at highly basic pH > 10.8. However, only three of them ($q = +2, +1, -2$) are experimentally accessible in a pure form because Tyr and Lys have their dissociation constants close to each other. For the determination of the conformation of the free octamer^{SRF} in different charged states a combination of CD, Raman, and FTIR spectroscopies was used.

CD Spectroscopy. In the UV spectral region (190–240 nm), a negative spectral band at 196 nm was observed in the whole pH range (3–11). This spectral band was accompanied by a negative shoulder around 230 nm (for acidic and neutral pH). In the basic environment, this shoulder shifts to 225 nm and its intensity slightly increases (see Figure 2). Bands at 196 nm and about 230 nm can be attributed to π - π^* and n - π^* transitions and assigned to an unordered conformation.^{42,43} As the octamer^{SRF} in its primary structure contains tyrosine residue, one can expect up to four additional π - π^* transitions because of the phenolic chromophore of tyrosine side chain. Although they are partially hidden by a signal of n - π^*

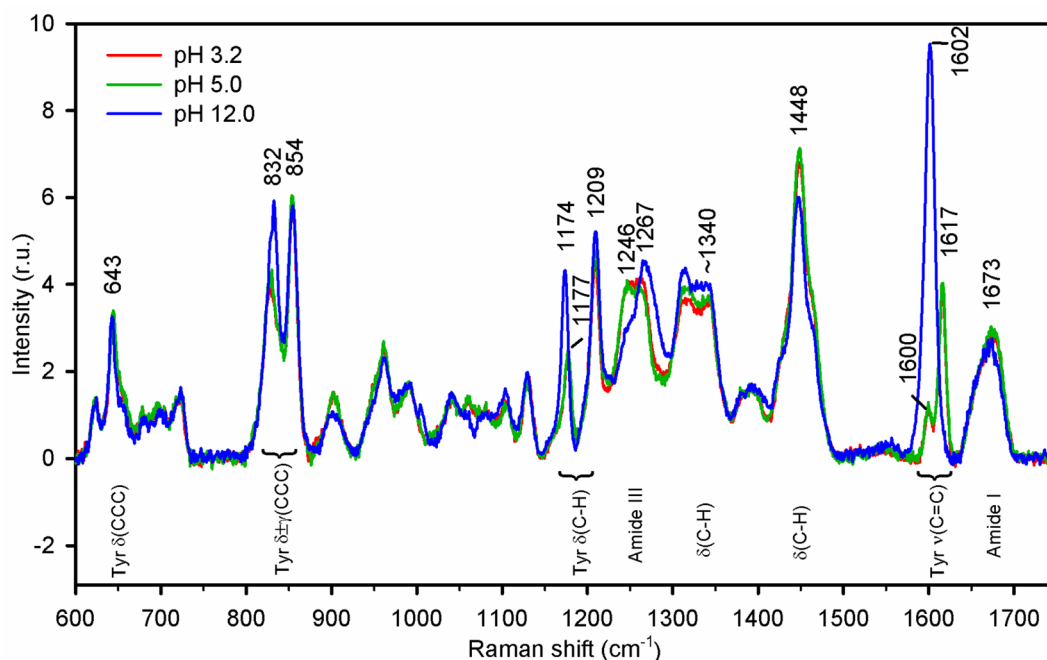


Figure 3. Raman spectra of the octamer^{SRF} measured at acidic pH 3.2 (red), neutral pH 5.0 (green), and basic pH 12.0 (blue). Most distinctive bands are labeled and empirically assigned according to the literature.^{46,47,49–51}

Table 1. Calculated and Experimental Frequencies of Selected Vibrational Modes of the Tyrosine Resp. Tyrosinate within the Octamer^{SRF}

tyrosine (Y) modes ^a	description	Raman shift (cm ⁻¹)		Wilson ^c nomenclature	tyrosinate (Y') modes ^a	description	Raman shift (cm ⁻¹)		Wilson ^c nomenclature
		experiment	DFT ^b				experiment	DFT ^b	
1	$\nu(\text{C}=\text{C})$	1617	1620	ν_{8a}	1	$\nu(\text{C}=\text{C})$	1602	1600	ν_{8a}
2	$\nu(\text{C}=\text{C})$	1600	1599	ν_{8b}	2	$\nu(\text{C}=\text{C})$		1525	ν_{8b}
3	$\nu(\text{C}=\text{C})$		1515	ν_{19a}	3	$\nu(\text{C}=\text{C})$		1512	ν_{19a}
4	$\nu(\text{C}=\text{C})$	1448	1440	ν_{19b}	4	$\nu(\text{C}=\text{C})$	1425	1426	ν_{19b}
5	$\nu(\text{C}=\text{C})$		1358	ν_{14}	5	$\nu(\text{C}=\text{C})$		1368	
6	$\delta(\text{C}-\text{H})$	1341	1340	ν_3	6	$\nu(\text{C}=\text{C})$		1319	ν_{14}
7	$\delta(\text{C}-\text{H})$		1274		7	$\nu(\text{C}=\text{C}), \delta(\text{C}-\text{H})$		1253	ν_{14}, ν_3
8	$\delta(\text{C}-\text{H})$	1209	1212		8	$\delta(\text{C}-\text{H})$	1209	1208	
9	$\delta(\text{C}-\text{H})$		1188	ν_{9a}	9	$\delta(\text{C}-\text{H})$	1174	1160	ν_{9a}
9a	$\delta(\text{C}-\text{H})$	1177	1178	ν_{9a}	10	$\delta(\text{C}-\text{H})$	1104	1094	ν_{15}
10	$\delta(\text{C}-\text{H})$	1129	1122	ν_{15}	11	$\delta(\text{C}-\text{H})$		986	ν_{18a}
11	$\delta(\text{C}-\text{H})$		1016	ν_{18a}	12	$\gamma(\text{C}-\text{H})$		946	ν_{17a}
12	$\gamma(\text{C}-\text{H})$	962	958	ν_{17a}	13	$\gamma(\text{C}-\text{H})$		936	ν_{10b}
13	$\gamma(\text{C}-\text{H})$		942	ν_{10b}	14	$\delta(\text{CCC})$	854, 832 ^d	842	ν_1
14	$\delta(\text{CCC})$	854, 830 ^d	854	ν_1	15	$\gamma(\text{C}-\text{H})$	832	830	ν_{17b}
15	$\gamma(\text{C}-\text{H})$	830	830	ν_{17b}	16	$\gamma(\text{C}-\text{H})$		809	ν_{10a}
16	$\gamma(\text{C}-\text{H})$		820	ν_{10a}	17	$\gamma(\text{CCC})$	723	737	ν_4
17	$\gamma(\text{CCC})$		760	ν_4	18	$\delta(\text{CCC})$	642	635	ν_{6b}
17a	$\gamma(\text{CCC})$	723	717	ν_4	19	$\gamma(\text{CCC})$	854, 832 ^d	430	ν_{16a}
18	$\delta(\text{CCC})$	643	642	ν_{6b}					
19	$\gamma(\text{CCC})$	854, 830 ^d	420	ν_{16a}					

^aSelected vibrational modes of tyrosine within the octamer^{SRF} determined by DFT calculations (scaled). ^bLevel B3PW91/6-31G**/COSMO (water); scaled according to eq 1. ^cBased on refs 48 and 58. ^dFermi doublet, the second harmonic of the mode 19 (ν_{16a}) combined with 14 (ν_1).

transitions of the peptide backbone we can assume that in the octamer^{SRF} $\pi-\pi^*$ B_b transitions significantly contribute to the weak spectral band observed at ~ 225 nm.

The contribution of aromatic side chains can be easily identified in longer wavelengths (240–320 nm). The weak positive spectral band around 276 nm was observed for the peptide at acidic and neutral environment (pH 3.2 and 5.0,

respectively) together with the weak positive band at 275 nm in absorption spectra (Figure S1, Supporting Information). At basic pH 11.0, a red shift to 294 nm was observed for both absorption and CD spectra, though the sign of the CD band does not change. This behavior corresponds to the phenolate form of the tyrosine side chain and is in a good agreement with published data.^{44,45}

In summary, the CD data support features of an unordered structure as a main structural motif of the octamer^{SRF}. However, electronic CD is essentially sensitive to long-range interactions. Therefore, we include a study by vibrational spectroscopies (Raman and FTIR), which are more sensitive to structural details and local arrangements.

Raman Spectroscopy. Experimental Raman spectra (Figure 3) were measured at pH 3.2 (acidic), 5.0 (neutral), and 12.0 (basic), which correspond to the +2, +1, and -2 charged states, respectively (see Figure 1). Negligible change between Raman spectra in acidic and neutral pH was observed. It indicates that deprotonation of Glu does not have any effect on either the secondary structure of the oligomer or on the polarizability of Glu residue. Further increasing of pH to the basic range resulted in significant changes of several Raman bands. These changes could be divided into two groups, the first one corresponding to tyrosine deprotonation and the second one to the secondary structure changes. Nevertheless, it is worth noting that no direct spectroscopic markers of deprotonation of the pair of Lys residues were observed.

The loss of a hydrogen at the Tyr phenol group leads to a shift and intensity change of several peaks. The difference between the neutral and negatively charged form of Tyr is most prominent on the in-plane stretching vibrations $\nu(\text{C}=\text{C})$ of the ring.^{46,47} At neutral pH, the pair of bands at 1617 and 1600 cm^{-1} (ν_{8a} and ν_{8b} , respectively; according to the nomenclature of benzene ring modes by Wilson,⁴⁸ see Table 1 for the detailed band assignment) was observed, whereas at basic pH, only one strong band at 1602 cm^{-1} corresponding to the ν_{8a} was present. Ring deformation modes $\delta(\text{C}-\text{H})$ are much less affected by deprotonation. The peak at 1209 cm^{-1} changes neither the position nor the intensity, whereas the band at 1177 cm^{-1} corresponding to ν_{9a} with a contribution from $\text{C}_6\text{H}_5-\text{C}$ stretching increases its intensity and shifts to 1174 cm^{-1} at basic pH.^{47,49,50} A change in the ratio of the bands at 830 and 854 cm^{-1} assigned to the Fermi resonance^{46,51} between the symmetric ring-breathing deformation $\delta(\text{CCC})$, ν_1 and the overtone of the nonplanar ring vibration $\gamma(\text{CCC})$, ν_{16a} (fundamental frequency 413 cm^{-1}) was also observed. At basic pH, the lower band shifts to 832 cm^{-1} and increases in intensity. This is in agreement with literature⁵¹ showing that the relative intensity increase of this particular band as compared to that of the band at 854 cm^{-1} is directly related to the presence of a negative charge (or even partial negative charge) at the oxygen atom. The 643 cm^{-1} band corresponding to the $\delta(\text{CCC})$ deformation, ν_{6b} appears to be insensitive to the protonation state at all.

Information about the secondary structure can be derived from the position and shape of the amide I and amide III bands in Raman spectra. In acidic and neutral environments, the amide I is located at 1673 cm^{-1} , whereas at basic pH, a small downshift to 1671 cm^{-1} was observed. The difference is more obvious in the amide III region consisting of two components. At acidic and neutral pH, they are of approximately the same intensity, with low and high frequency components at 1246 cm^{-1} and 1262 cm^{-1} , respectively. At basic pH, the relative intensity of the low frequency component decreases while its position remains the same as mentioned above (i.e., 1246 cm^{-1}); the high frequency component is shifted to 1267 cm^{-1} . This indicates that the octamer^{SRF} adopts a slightly different secondary structure in a basic environment than in neutral and acidic ones.

The maximum of the amide I at $\sim 1672 \text{ cm}^{-1}$ points on a possible presence of β sheets, β turns, and β hairpins along with random coil or unordered structures. The two bands at 1246 and $\sim 1265 \text{ cm}^{-1}$ in the amide III region can be assigned to the same structures.^{52,53} This is in a general agreement with an estimation of the secondary structure from the primary peptide sequence by GOR⁵⁴ and Chou and Fasman⁵⁵ algorithms (data not shown). Based on this analysis it may be stated that the octapeptide tends to form a β -hairpin structure, which is in a dynamical equilibrium with an unordered or random coil structure.

At neutral and basic pH, there are also small differences between intensities of the band at 1448 cm^{-1} and the broad band at $\sim 1340 \text{ cm}^{-1}$ corresponding to $\delta(\text{C}-\text{H})$ deformations (CH_2 and CH_3 bending modes). This could be an effect of both the deprotonation of Lys side chains and the overall influence of the highly basic environment.

Infrared Spectroscopy. FTIR spectra of the octamer^{SRF} were measured at pH 3.0 and 11.5 because at these pHs, the peptide is fully protonated or deprotonated, respectively (see Figure 1). The Figure 4 depicts FTIR spectra at given pH. Two

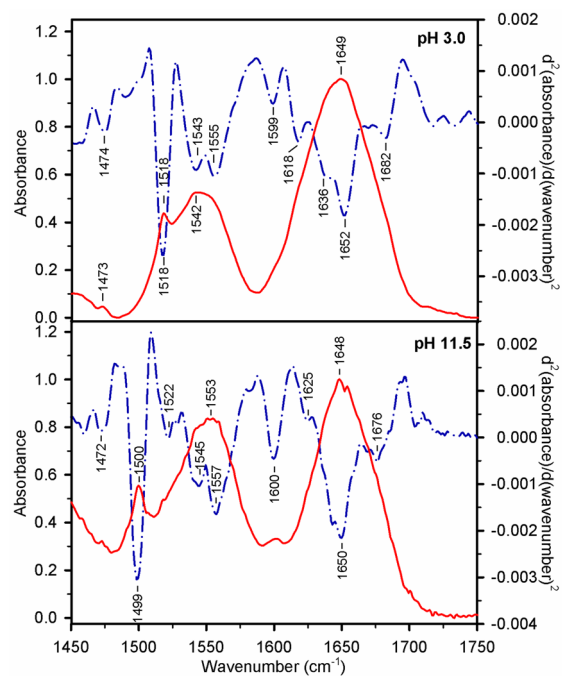


Table 2. Occurrences of Selected Clusters in the MD Trajectory and Description of Their Secondary Structure

neutral pH			basic pH		
cluster	occurrence (%)	structure	cluster	occurrence (%)	structure
N1	25	β turn, unordered	B1	24.9	extended
N2	17.5	extended	B2	20.2	extended
N3	10.4	β turn, extended	B3	18.4	β turn, extended
N4	6.9	α helix, unordered	B4	7.9	β turn, unordered
N5	6.3	β turn, extended	B5	6.5	unordered
N6	5.6	β turn, unordered	Σ B6–16	22.3 ^a	
N7	5.2	α helix, unordered			
N8	5.1	α helix, unordered			
Σ N9–21	18.2 ^a				

^aThe clusters with occurrence below 4%

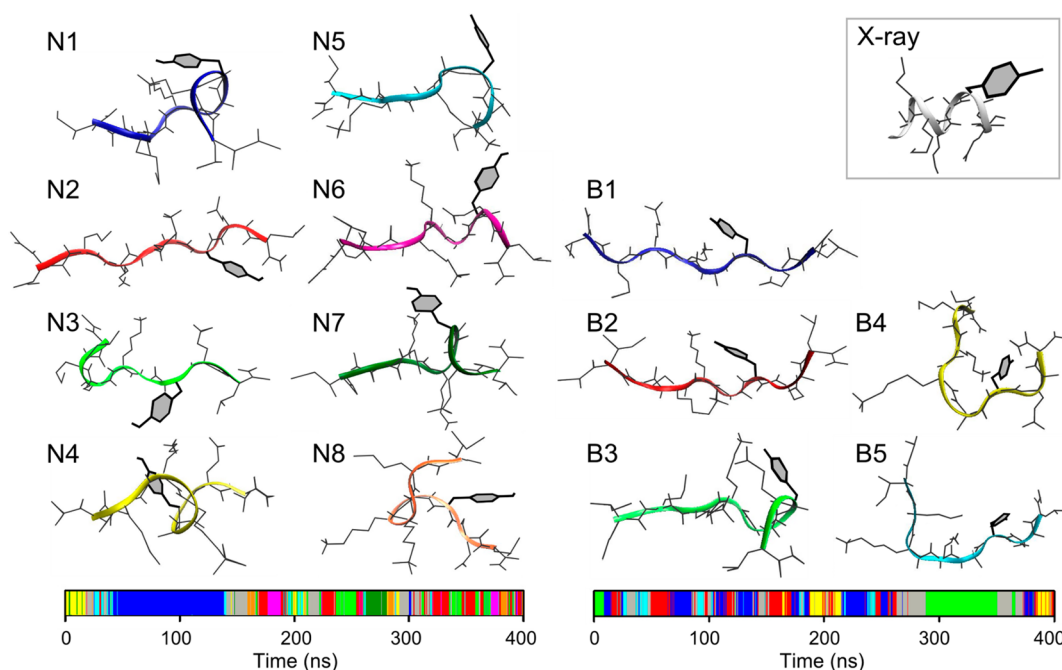


Figure 5. Most probable conformers sorted according to their occurrence as revealed by the cluster analysis both in neutral (N1–8) and basic (B1–5) pH upon the MD trajectory acquired from 400 ns AMBER99SB simulation (lower). Colors of the clusters correspond to their occurrence within the MD trajectory (gray color represents less occurring clusters). The X-ray structure of the octamer^{SRF} was extracted from the structure of the SRF bound to DNA.⁹

hairpin.⁵⁶ Classical Tyr ring vibrations⁵⁷ $\nu(\text{C}=\text{C})$ are clearly visible at 1618 cm^{-1} , ν_{8a} , and 1518 cm^{-1} , ν_{19a} along with a weaker $\nu(\text{C}=\text{C})$, ν_{8b} ring vibration⁵⁷ at 1599 cm^{-1} . Thus, we may conclude that the octamer^{SRF} exists as a mixture of unordered structure with turns together with a dominant structure of β hairpin at pH 3.0.

The most apparent spectral changes at pH 11.5 are connected with Tyr deprotonation. The band corresponding to tyrosinate ring $\nu(\text{C}=\text{C})$, ν_{19a} vibrations⁵⁷ at 1518 cm^{-1} is downshifted by 19 cm^{-1} at 1499 cm^{-1} . This state is more polar than the neutral state, and thus, the intensity of several other bands increases (e.g., $\nu(\text{C}=\text{C})$ ring vibrations at 1600 cm^{-1} , ν_{8a} and 1522 cm^{-1} , ν_{8b}). Moreover, it seems that the β -hairpin structure nearly disappears at pH 11.5 and that disordered structure (at 1650 cm^{-1}) with turns (at 1676 cm^{-1}) prevails.⁵⁶ It indicates that negative charges prevent the formation of any stable compact secondary structure.

Molecular Dynamic Simulations. Based on the experimental results showing that the main spectral difference arises between the octamer structures with total charge $q = +1$ and 0

(see Figure 1), that is, between the octamer containing Tyr in its protonated and deprotonated (tyrosinate) form, the MD simulation was performed only for these two states. In the following text, they are referred to according to the pH region in which they occur (i.e. “neutral” or N for the octamer^{SRF} with tyrosine ($q = +1$) and “basic” or B for the octamer^{SRF} with tyrosinate ($q = 0$)). From the total number of 4000 frames of MD trajectory for both forms, cluster analysis found 21 and 16 individual clusters for neutral and basic form, respectively. The occurrences and secondary structure characteristics for the most frequent clusters (occurrence above 4%) are listed in Table 2. Their geometries are shown in Figure 5 together with diagrams of their incidence during the simulation.

The secondary structure of neutral clusters is dominated by unordered and extended conformations ($\sim 70\%$); regular structure motives are represented by β turns ($\sim 20\%$) and by small contribution of α -helical loops ($<10\%$). Basic clusters prefer unordered and extended arrangement even more ($\sim 85\%$) mainly at the expense of β turns ($\sim 10\%$). The

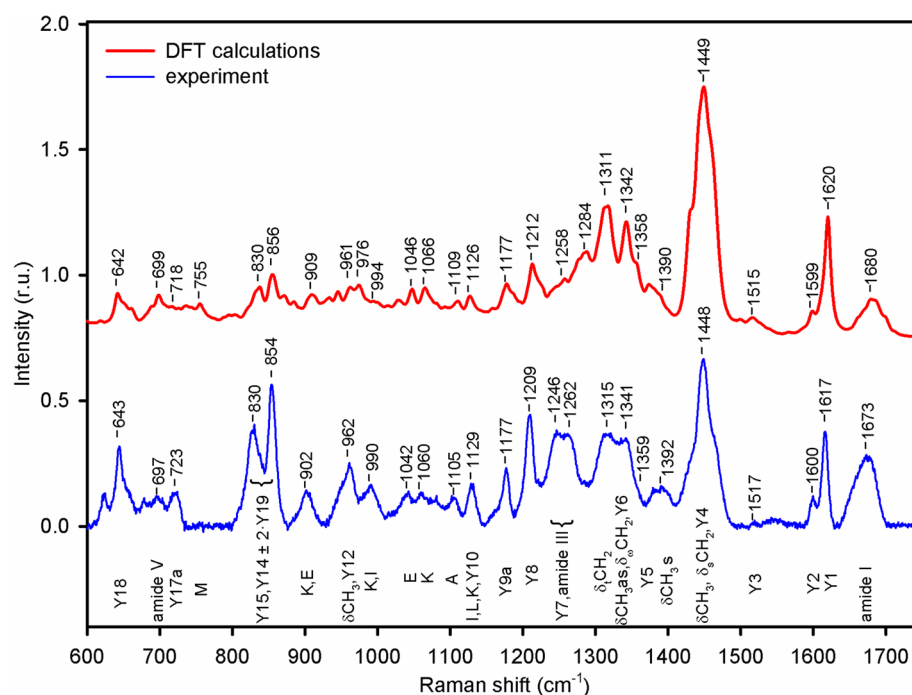


Figure 6. Comparison of experimental and calculated (B3PW91/6-31G**/COSMO(water)) Raman spectra of the octamer^{SRF} at neutral pH. Vibrations of Tyr (Y) and the most significant bands of other amino acids present in the oligopeptide are assigned (and marked by one-letter amino acid code) according to the results of DFT calculations. Calculated frequencies were scaled using the second order polynomial fit to enable a direct assignment of bands (for details, see eq 1 in the Theory section).

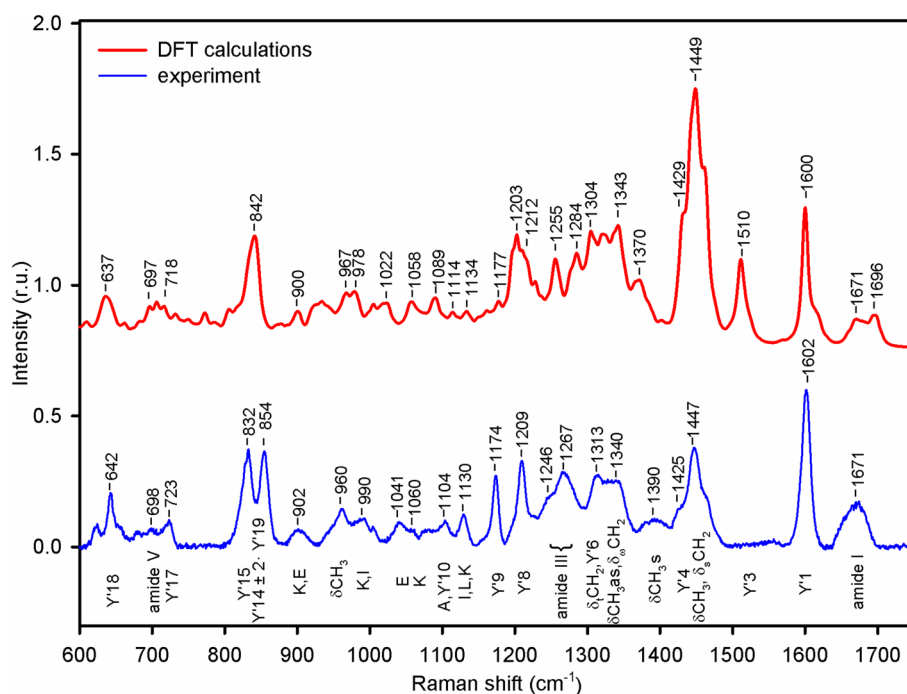


Figure 7. Comparison of experimental and calculated (B3PW91/6-31G**/COSMO(water)) Raman spectra of the octamer^{SRF} at basic pH. Vibrations of tyrosinate (Y) and the most significant bands of other amino acids present in the oligopeptide are assigned according to the results of DFT calculations. Calculated frequencies were scaled using the second order polynomial fit to enable the direct assignment of bands (for details, see eq 1 in the Theory section).

occurrence of α -helical loops is also lower in basic clusters (<5%).

QM simulations. As a first step, the octamer^{SRF} spectra in its differently charged forms (see Figure 1) were simulated to observe a pure effect of deprotonation on Raman spectra. The

α -helical structure of the model molecule was derived from the X-ray structure of core-SRF (Figure 5, upper right corner), which was not altered by an energy minimization and represents a stable local minimum independent of the charge state.^{9,10} Therefore, differences among the charged forms could

be directly assigned to the changes in protonation state of present amino acids. Calculations were performed on the B3PW91/6-31G**/COSMO level using water as an implicit solvent. Simulated spectra are depicted in Figure S2, Supporting Information. It is evident that the major alterations are associated with change of the total charge from +1 to 0 (i.e., with the deprotonation of the Tyr residue), whereas the charge changes on Glu and Lys residues have only a negligible effect, in good agreement with experimental results. Therefore, further simulation could be limited to only two charged states: neutral and basic (similarly to MD simulations).

The geometries resulting from the MD cluster analysis with occurrence >4% (see Table 2) were used for more accurate calculation of octamer^{SRF} Raman spectra. All conformers were energy minimized using the ModRedundant option for keeping the backbone torsion angles fixed. Spectra of individual conformers were simulated using the above-mentioned level of theory. The final spectra of neutral and basic forms were calculated as a weighted average in using the occurrences of given forms mentioned in Table 2 (see Figure S3, Supporting Information). The use of Boltzmann weights led to unreliable results as the calculated energy of conformers does not include any contribution from hydrogen bonding and charge dissipation.

For the purpose of direct comparison between experimental and calculated spectra, a scaling according to the eq 1 was applied. A very good agreement was achieved between the experiment and the simulation, as can be seen in Figure 6 for the neutral form (and in Figure 7 for the basic form), allowing the precise vibrational analysis. Almost all experimental bands (including very weak features) were assigned with emphasis on peptide backbone vibrations and characteristic modes of individual amino acids, especially on Tyr. Experimental spectra were also fitted using a basis consisting of spectra of individual conformers (relative occurrences as free parameters), but no significant improvement comparing experimental and calculated spectra was reached.

Every neutral conformer possessed 456 fundamental vibrations (basic conformers 453), from which ~245 were in our region of interest between 600 and 1800 cm^{-1} . Among them, 19 specific vibrations of tyrosine Y (tyrosinate Y') phenyl (phenolate) ring were identified for every conformer, often coupled with vibrations of other parts of the oligopeptide. Frequencies and Raman intensities of these modes are listed in Supporting Information Tables S1, neutral conformers and basic conformers in Supporting Information Table S2; Supporting Information Tables S3 and S4 contain the scaled frequencies used for direct comparison to experiments. The general description of selected modes for both neutral and basic form is listed in Table 1 along with their experimental and calculated (weighted average) wavenumbers and labeling by Wilson.⁴⁸ The graphical representation of these modes is shown in Figure S4, Supporting Information. Changes in the secondary structure among individual conformers have no significant influence on frequencies of Tyr vibrations that mostly differ by less than $\pm 3 \text{ cm}^{-1}$. Rare larger shifts are usually caused by couplings with other parts of the structure, which also influences the calculated intensities.

In general, the quality of simulated spectrum and its resemblance to the experimental one is better for the neutral form than for the basic one. We assume that this is caused by the higher number of charged groups in the latter case; the implicit solvent model is not able to mimic the effects of charge

distribution adequately. Furthermore, the absence of explicit solvent and hydrogen bonding to the carbonyls of the peptide backbone lead to the limited precision of calculated frequencies and band shapes in the amide I and amide III region.

We found that even smaller basis sets can be used to reach a reasonable agreement with experimental data, provided that they include at least polarization functions on non-hydrogen atoms (6-31G* level and higher). Spectra simulated using the BPW91 functional manifested better agreement in the frequency scale; however, the overall spectral shape was substantially worse as compared to that of the B3PW91 (see Figure S5, Supporting Information).

The Fermi doublet at 832 and 854 cm^{-1} formed by the mode Y_{14} ($\delta(\text{CCC}), \nu_1$) and the second harmonic of the mode Y_{19} ($\gamma(\text{CCC}), \nu_{16a}$) cannot be correctly calculated at a harmonic level of simulation; thus, only the mode Y_{14} can be found in the simulated spectra in this region.

Our calculations also reveal the origin of the major spectral changes between the tyrosine in its protonated and deprotonated forms. The nature of both tyrosine and tyrosinate vibrational modes was found to be very similar, as could be seen from comparison of (i) their visualization in the upper and lower part of Figure S4, Supporting Information as well as (ii) their overall description in Table 1. Generally, absence of hydrogen from the hydroxyl group leads to the downshift of calculated frequencies for about $\sim 20 \text{ cm}^{-1}$, to the change of the symmetry leading to different selection rules, and consequently, to changes in Raman intensities. This can be demonstrated on several bands visible in the measured Raman spectrum. One of the most distinctive features, the mode Y_1 ($\nu(\text{C}=\text{C}), \nu_{8a}$) at 1620 cm^{-1} (exp. 1617 cm^{-1}) in neutral pH, shifts in basic pH to 1600 cm^{-1} (Y'_1 , exp. 1602 cm^{-1}) and increases in intensity. On the other hand, the mode Y_2 ($\nu(\text{C}=\text{C}), \nu_{8b}$) at 1599 cm^{-1} (exp. 1600 cm^{-1}) in neutral pH exhibits nearly zero intensity in basic pH due to the symmetry, and calculations suggest a large shift to 1525 cm^{-1} (Y'_2). The deformation modes $\delta(\text{C}-\text{H})$ between 1170 and 1210 cm^{-1} , Y_{9a} (ν_{9a}) and Y_8 , shift only slightly and remain on the approximately same intensity as well as the mode Y_{18} ($\delta(\text{CCC}), \nu_{6b}$) at 642 cm^{-1} (exp. 643 cm^{-1}).

CONCLUSIONS

The secondary structure of isolated octamer^{SRF} was found to be substantially different as compared to its arrangement as a part of the core-SRF. However, the crystal structure of the core-SRF–DNA complex does not take in account the variety of conformations experienced by both partners in solution.¹³ Analysis of FTIR and Raman experimental spectra revealed the presence of unordered or random coil structure together with β turns and β hairpins. The occurrence of β turns and β hairpins was greater in neutral pH, whereas in basic pH, their content vanished. CD, less local than previous vibrational techniques and sensitive to the arrangement of large segments, indicated the unordered or random coil structure as a main structural motif.

Structures predicted by MD simulations were in an excellent agreement with experimental analysis for both neutral and basic forms of the octamer^{SRF}. The secondary structure of each conformer was dominated by unordered or extended conformation and contained a substantial proportion of β turns. The loss of β -like structure in basic form was well represented. Furthermore, MD simulations suggested a minor presence of α -helical loops in the neutral form, which could not be observed experimentally due to their low occurrence. MD

proved to be a powerful tool for prediction of highly conformationally unstable peptide oligomers.

Several spectral bands were successfully assigned according to the available literature; however, for a precise and accurate assignment of weaker features, QM calculations were necessary. Spectra simulated on the basis of MD predicted conformers were found to be in a fine correspondence with experimental profiles, especially for the neutral pH form, which proves the reliability of MD simulations. Tyrosine and tyrosinate vibrations were additionally characterized and classified in the context of previous research.

The most distinctive features of the Raman, FTIR, and CD spectra were associated with Tyr173. Both vibrational and electronic spectra proved to be sensitive to its deprotonation, whereas charge changes on other amino acids caused no or only negligible differences. Thus, it can be concluded that the variation of charges of the highly conserved amino acid Lys170, Lys171, and Glu174 do not change the organization of octamer^{SRF}, in contrast to the less-conserved Tyr173. On the point of view of the biological relevance of these observations, it is worth noting that all these charged residues are involved in the formation of the complex of core-SRF with DNA. The peculiar properties of Tyr173 revealed in octamer^{SRF} are probably involved in the formation of the complex with the cognate DNA. Only residues located at or nearby a non-conserved position might play a role in the DNA specificity; this differentiates SRF among other MADS proteins. Thus, we can assess that octamer^{SRF} reveals fundamental properties of Tyr173 that are involved in the functional role of the MADS box (i.e., the determination of the DNA binding specificity).³

In conclusion, it was successfully demonstrated that interplay of experimental and theoretical approach represents a useful and powerful tool for detailed study of various short oligopeptides (up to ~180 atoms) with biological relevance. Although separately both experiment and MD simulation accompanied by DFT calculation offer rich information, it is their combination which provides deeper understanding and leads to the more accurate interpretation of acquired results.

■ ASSOCIATED CONTENT

📄 Supporting Information

Complementary data include experimental and computational details and spectra with graphical representations of vibration modes. This information is available free of charge via the Internet at <http://pubs.acs.org/>.

■ AUTHOR INFORMATION

Corresponding Author

*J. Štěpánek. Phone: +420 221 911 345. Fax: +420 224 922 797. E-mail: stepjos@karlov.mff.cuni.cz.

Notes

The authors declare no competing financial interest.

■ ACKNOWLEDGMENTS

The authors express gratitude to Sergei Kruglik (Université Pierre et Marie Curie, France) for kind help with Raman measurements and to Yves-Marie Coïc (Institut Pasteur, France) for synthesis of the octamer^{SRF}. B.P. gratefully acknowledges the French Government support for her stay in Laboratoire Jean Perrin (Université Pierre et Marie Curie, France). This work was supported by the Czech Science

Foundation (No. 202/09/0193) and the Grant Agency of Charles University (No. 402111).

■ REFERENCES

- (1) Miano, J. M.; Long, X. C.; Fujiwara, K. Serum Response Factor: Master Regulator of the Actin Cytoskeleton and Contractile Apparatus. *Am. J. Physiol.: Cell Physiol.* **2007**, *292*, C70–C81.
- (2) Schwarzsommer, Z.; Huijser, P.; Nacken, W.; Saedler, H.; Sommer, H. Genetic Control of Flower Development by Homeotic Genes in *Antirrhinum majus*. *Science* **1990**, *250*, 931–936.
- (3) Shore, P.; Sharrocks, A. D. The MADS-box Family of Transcription Factors. *Eur. J. Biochem.* **1995**, *229*, 1–13.
- (4) Norman, C.; Runswick, M.; Pollock, R.; Treisman, R. Isolation and Properties of cDNA Clones Encoding SRF, a Transcription Factor that Binds to the c-Fos Serum Response Element. *Cell* **1988**, *55*, 989–1003.
- (5) Sharrocks, A. D.; Gille, H.; Shaw, P. E. Identification of Amino Acids Essential for DNA Binding and Dimerization in p67SRF: Implications for a Novel DNA-Binding Motif. *Mol. Cell. Biol.* **1993**, *13*, 123–132.
- (6) Rezacova, B.; Coic, Y. M.; Zentz, C.; Turpin, P. Y.; Stepanek, J. Spectroscopic Determination of pKa Constants of MADS Box Segments. *Spectrosc. Int. J.* **2012**, *27*, 455–461.
- (7) Thurlkill, R. L.; Grimsley, G. R.; Scholtz, J. M.; Pace, C. N. pK Values of the Ionizable Groups of Proteins. *Protein Sci.* **2006**, *15*, 1214–1218.
- (8) Sela, M.; Katchalski, E. Spectrophotometric Titration of α -Amino Acid Copolymers Containing Tyrosine. *J. Am. Chem. Soc.* **1956**, *78*, 3986–3989.
- (9) Pellegrini, L.; Song, T.; Richmond, T. J. Structure of Serum Response Factor Core Bound to DNA. *Nature* **1995**, *376*, 490–498.
- (10) Mo, Y.; Ho, W.; Johnston, K.; Marmorstein, R. Crystal Structure of a Ternary SAP-1/SRF/c-fos SIRE DNA Complex. *J. Mol. Biol.* **2001**, *314*, 495–506.
- (11) Gramzow, L.; Ritz, M. S.; Theissen, G. On the Origin of MADS-Domain Transcription Factors. *Trends Genet.* **2010**, *26*, 149–153.
- (12) Hassler, M.; Richmond, T. J. The B-box Dominates SAP-1-SRF Interactions in the Structure of the Ternary Complex. *EMBO J.* **2001**, *20*, 3018–3028.
- (13) Stepanek, J.; Kopecky, V.; Mezzetti, A.; Turpin, P. Y.; Paulin, D.; Alpert, B.; Zentz, C. Structural and Dynamic Changes of the Serum Response Element and the Core Domain of Serum Response Factor Induced by Their Association. *Biochem. Biophys. Res. Commun.* **2010**, *391*, 203–208.
- (14) Kopecky, V.; Ettrich, R.; Hofbauerova, K.; Baumruk, V. Vibrational Spectroscopy and Computer Modeling of Proteins: Solving Structure of Alpha(1)-Acid Glycoprotein. *Spectrosc. Int. J.* **2004**, *18*, 323–330.
- (15) Chan, W. C.; White, P. D. *Fmoc Solid Phase Peptide Synthesis: A Practical Approach*; Oxford University Press: London, 2000.
- (16) Palacky, J.; Mojzes, P.; Bok, J. SVD-Based Method for Intensity Normalization, Background Correction and Solvent Subtraction in Raman Spectroscopy Exploiting the Properties of Water Stretching Vibrations. *J. Raman Spectrosc.* **2011**, *42*, 1528–1539.
- (17) Dousseau, F.; Therrien, M.; Pezolet, M. On the Spectral Subtraction of Water from the FT-IR Spectra of Aqueous Solutions of Proteins. *Appl. Spectrosc.* **1989**, *43*, 538–542.
- (18) Case, D. A.; Darden, T. A.; Cheatham, T. E.; Simmerling, C. L.; Wang, J.; Duke, R. E.; Luo, R.; Walker, R. C.; Zhang, W.; Merz, K. M., et al. *AMBER 11*; University of California: San Francisco, 2010.
- (19) Hornak, V.; Abel, R.; Okur, A.; Strockbine, B.; Roitberg, A.; Simmerling, C. Comparison of Multiple Amber Force Fields and Development of Improved Protein Backbone Parameters. *Proteins* **2006**, *65*, 712–725.
- (20) Vanqualef, E.; Simon, S.; Marquant, G.; Garcia, E.; Klimerak, G.; Delepine, J. C.; Cieplak, P.; Dupradeau, F. Y. RED Server: a Web Service for Deriving RESP and ESP Charges and Building Force Field Libraries for New Molecules and Molecular Fragments. *Nucleic Acids Res.* **2011**, *39*, W511–W517.

- (21) Bayly, C. I.; Cieplak, P.; Cornell, W. D.; Kollman, P. A. A Well-Behaved Electrostatic Potential Based Method Using Charge Restraints for Deriving Atomic Charges: the RESP Model. *J. Phys. Chem.* **1993**, *97*, 10269–10280.
- (22) Dupradeau, F. Y.; Pigache, A.; Zaffran, T.; Savineau, C.; Lelong, R.; Grivel, N.; Lelong, D.; Rosanski, W.; Cieplak, P. The R.E.D. Tools: Advances in RESP and ESP Charge Derivation and Force Field Library Building. *Phys. Chem. Chem. Phys.* **2010**, *12*, 7821–7839.
- (23) Granovsky, A. A. Firefly version 7.1.G. <http://classic.chem.msu.su/gran/firefly/index.html> (accessed June 19, 2012).
- (24) Phillips, J. C.; Braun, R.; Wang, W.; Gumbart, J.; Tajkhorshid, E.; Villa, E.; Chipot, C.; Skeel, R. D.; Kale, L.; Schulten, K. Scalable Molecular Dynamics with NAMD. *J. Comput. Chem.* **2005**, *26*, 1781–1802.
- (25) Miyamoto, S.; Kollman, P. A. Settle: An Analytical Version of the SHAKE and RATTLE Algorithm for Rigid Water Models. *J. Comput. Chem.* **1992**, *13*, 952–962.
- (26) Harvey, M. J.; Giupponi, G.; De Fabritiis, G. ACEMD: Accelerating Biomolecular Dynamics in the Microsecond Time Scale. *J. Chem. Theory Comput.* **2009**, *5*, 1632–1639.
- (27) Feenstra, K. A.; Hess, B.; Berendsen, H. J. C. Improving Efficiency of Large Time-Scale Molecular Dynamics Simulations of Hydrogen-Rich Systems. *J. Comput. Chem.* **1999**, *20*, 786–798.
- (28) Humphrey, W.; Dalke, A.; Schulten, K. VMD: Visual Molecular Dynamics. *J. Mol. Graphics* **1996**, *14*, 33–38.
- (29) Kabsch, W.; Sander, C. Dictionary of Protein Secondary Structure: Pattern Recognition of Hydrogen-Bonded and Geometrical Features. *Biopolymers* **1983**, *22*, 2577–2637.
- (30) Frisch, M. J.; Trucks, G. W.; Schlegel, H. B.; Scuseria, G. E.; Robb, M. A.; Cheeseman, J. R.; Scalmani, G.; Barone, V.; Mennucci, B.; Petersson, G. A., et al. *Gaussian 09*, Revision B01; Gaussian, Inc.: Wallingford CT, 2009.
- (31) Parr, R. G.; Yang, W. *Density-Functional Theory of Atoms and Molecules*; Oxford University Press: New York, 1994.
- (32) Perdew, J. P.; Burke, K.; Wang, Y. Generalized Gradient Approximation for the Exchange-Correlation Hole of a Many-Electron System. *Phys. Rev. B* **1996**, *54*, 16533–16539.
- (33) Ditchfield, R.; Hehre, W. J.; Pople, J. A. Self-Consistent Molecular-Orbital Methods. IX. An Extended Gaussian-Type Basis for Molecular-Orbital Studies of Organic Molecules. *J. Chem. Phys.* **1971**, *54*, 724–728.
- (34) Perdew, J. P.; Wang, Y. Accurate and Simple Analytic Representation of the Electron-Gas Correlation Energy. *Phys. Rev. B* **1992**, *45*, 13244–13249.
- (35) Klamt, A.; Schuurmann, G. COSMO: a New Approach to Dielectric Screening in Solvents With Explicit Expressions for the Screening Energy and its Gradient. *J. Chem. Soc., Perkin Trans. 2* (1972-1999) **1993**, 799–805.
- (36) Klamt, A. COSMO and COSMO-RS. In *The Encyclopedia of Computational Chemistry*; Schleyer, P. R.; Allinger, N. L.; Clark, T.; Gasteiger, J.; Kollman, P. A.; Schaefer III, H. F.; Schreiner, P. R., Eds.; John Wiley & Sons: Chichester, U. K., 1998; Vol. 1, pp 604–615.
- (37) Polavarapu, P. L. *Vibrational Spectra: Principles and Applications with Emphasis on Optical Activity*; Elsevier: Amsterdam, 1998; Vol. 85.
- (38) Suenaga, M. Facio: New Computational Chemistry Environment for PC Gamess. *J. Comput. Chem. Jpn.* **2005**, *4*, 25–32.
- (39) Scott, A. P.; Radom, L. Harmonic Vibrational Frequencies: An Evaluation of Hartree-Fock, Moller-Plesset, Quadratic Configuration Interaction, Density Functional Theory, and Semiempirical Scale Factors. *J. Phys. Chem.* **1996**, *100*, 16502–16513.
- (40) Merrick, J. P.; Moran, D.; Radom, L. An Evaluation of Harmonic Vibrational Frequency Scale Factors. *J. Phys. Chem. A* **2007**, *111*, 11683–11700.
- (41) Lehninger, A. L.; Nelson, D. L.; Cox, M. M. *Lehninger Principles of Biochemistry*, 4th ed.; W.H. Freeman: New York, 2004.
- (42) Drake, A. F.; Siligardi, G.; Gibbons, W. A. Reassessment of the Electronic Circular-Dichroism Criteria for Random Coil Conformations of Poly(L-Lysine) and the Implications for Protein Folding and Denaturation Studies. *Biophys. Chem.* **1988**, *31*, 143–146.
- (43) Gokce, I.; Woody, R. W.; Anderluh, G.; Lakey, J. H. Single Peptide Bonds Exhibit Poly(pro)II ("Random Coil") Circular Dichroism Spectra. *J. Am. Chem. Soc.* **2005**, *127*, 9700–9701.
- (44) Simmons, N. S.; Glazer, A. N. An Analysis of the Tyrosine Circular Dichroism Bands in Ribonuclease. *J. Am. Chem. Soc.* **1967**, *89*, 5040–2.
- (45) Woody, R. W. In *Comprehensive Chiroptical Spectroscopy*; Beerova, N.; Polaravapu, P. L.; Nakanishi, K.; Woody, R. W., Eds.; John Wiley and Sons: Hoboken, NJ, 2012; Vol. 2, p 475.
- (46) Tuma, R. Raman Spectroscopy of Proteins: from Peptides to Large Assemblies. *J. Raman Spectrosc.* **2005**, *36*, 307–319.
- (47) Ludwig, M.; Asher, S. A. Ultraviolet Resonance Raman Excitation Profiles of Tyrosine: Dependence of Raman Cross Sections on Excited-State Intermediates. *J. Am. Chem. Soc.* **1988**, *110*, 1005–1011.
- (48) Wilson, E. B., Jr. The Normal Modes and Frequencies of Vibration of the Regular Plane Hexagon Model of the Benzene Molecule. *Phys. Rev.* **1934**, *45*, 706–714.
- (49) Johnson, C. R.; Ludwig, M.; Asher, S. A. Ultraviolet Resonance Raman Characterization of Photochemical Transients of Phenol, Tyrosine, and Tryptophan. *J. Am. Chem. Soc.* **1986**, *108*, 905–912.
- (50) Tsuboi, M.; Ezaki, Y.; Aida, M.; Suzuki, M.; Yimit, A.; Ushizawa, K.; Ueda, T. Raman Scattering Tensors of Tyrosine. *Biospectroscopy* **1998**, *4*, 61–71.
- (51) Siamwiza, M. N.; Lord, R. C.; Chen, M. C.; Takamatsu, T.; Harada, I.; Matsuura, H.; Shimanouchi, T. Interpretation of the Doublet at 850 and 830 cm^{-1} in the Raman Spectra of Tyrosyl Residues in Proteins and Certain Model Compounds. *Biochemistry* **1975**, *14*, 4870–4876.
- (52) Tensmeyer, L. G.; Kauffman, E. W. Protein Structure as Revealed by Nonresonance Raman Spectroscopy. In *Spectroscopic methods for determining protein structure in solution*; Havel, H. A., Ed.; VCH Publishers: New York, 1996; pp 69–95.
- (53) Pelton, J. T.; McLean, L. R. Spectroscopic Methods for Analysis of Protein Secondary Structure. *Anal. Biochem.* **2000**, *277*, 167–176.
- (54) Garnier, J.; Gibrat, J. F.; Robson, B. GOR Method for Predicting Protein Secondary Structure from Amino Acid Sequence. *Methods Enzymol.* **1996**, *266*, 540–553.
- (55) Chou, P. Y.; Fasman, G. D. Conformational Parameters for Amino Acids in Helical, β -Sheet, and Random Coil Regions Calculated from Proteins. *Biochemistry* **1974**, *13*, 211–222.
- (56) Barth, A. Infrared Spectroscopy of Proteins. *Biochim. Biophys. Acta, Bioenerg.* **2007**, *1767*, 1073–1101.
- (57) Barth, A. The Infrared Absorption of Amino Acid Side Chains. *Prog. Biophys. Mol. Biol.* **2000**, *74*, 141–173.
- (58) Palafox, M. A. Scaling Factors for the Prediction of Vibrational Spectra. I. Benzene Molecule. *Int. J. Quantum Chem.* **2000**, *77*, 661–684.